Neurophotonic tools for microscopic measurements and manipulation: status report

Ahmed S. Abdelfattah,[a] Sapna Ahuja,[b,c] Taner Akkin,[d] Srinivasa Rao Allu,[b,c] Joshua Brake,[e] David A. Boas,[f] Erin M. Buckley,[g,h] Robert E. Campbell,[i,j] Anderson I. Chen,[f] Xiaojun Cheng,[f] Tomáš Čižmár,[k] Irene Costantini,[l,m] Massimo De Vittorio,[n] Anna Devor,[f,o,*] Patrick R. Doran,[f] Mirna El Khatib,[b,c] Valentina Emiliani,[p] Natalie Fomin-Thunemann,[f] Yeshaiahu Fainman,[q] Tomas Fernandez-Alfonso,[r] Christopher G. L. Ferri,[s,†] Ariel Gilad,[t] Xue Han,[f] Andrew Harris,[u] Elizabeth M. C. Hillman,[v] Ute Hochgeschwender,[w] Matthew G. Holt,[x] Na Ji,[y] Kıvılcım Kılıç,[f] Evelyn M. R. Lake,[z] Lei Li,[aa] Tianqi Li,[d] Philipp Mächler,[f,‡] Evan W. Miller,[ab] Rickson C. Mesquita,[ac] K. M. Naga Srinivas Nadella,[r] U. Valentin Nägerl,[ad] Yusuke Nasu,[i] Axel Nimmerjahn,[ae] Petra Ondráčková,[k] Francesco S. Pavone,[m,af] Citlali Perez Campos,[v] Darcy S. Peterka,[v] Filippo Pisano,[n] Ferruccio Pisanello,[n] Francesca Puppo,[s,††] Bernardo L. Sabatini,[ag] Sanaz Sadegh,[s,§] Sava Sakadzic,[o] Shy Shoham,[ah] Sanaya N. Shroff,[f] R. Angus Silver,[r] Ruth R. Sims,[ai] Spencer L. Smith,[aj] Vivek J. Srinivasan,[ak] Martin Thunemann,[f] Lei Tian,[al] Lin Tian,[am] Thomas Troxler,[b,c] Antoine Valera,[r] Alipasha Vaziri,[an,ao] Sergei A. Vinogradov,[b,c] Flavia Vitale,[ap] Lihong V. Wang,[aa] Hana Uhlířová,[k] Chris Xu,[aq] Changhuei Yang,[ar] Mu-Han Yang,[q] Gary Yellen,[as] Ofer Yizhar,[u] and Yongxin Zhao[at]

[a]Brown University, Department of Neuroscience, Providence, Rhode Island, United States
[b]University of Pennsylvania, Perelman School of Medicine, Department of Biochemistry and Biophysics, Philadelphia, Pennsylvania, United States
[c]University of Pennsylvania, School of Arts and Sciences, Department of Chemistry, Philadelphia, Pennsylvania, United States
[d]University of Minnesota, Department of Biomedical Engineering, Minneapolis, Minnesota, United States
[e]Harvey Mudd College, Department of Engineering, Claremont, California, United States
[f]Boston University, Department of Biomedical Engineering, Boston, Massachusetts, United States
[g]Georgia Institute of Technology and Emory University, Wallace H. Coulter Department of Biomedical Engineering, Atlanta, Georgia, United States
[h]Emory University, Department of Pediatrics, Atlanta, Georgia, United States
[i]University of Tokyo, Department of Chemistry, Tokyo, Japan
[j]University of Alberta, Department of Chemistry, Edmonton, Alberta, Canada
[k]Institute of Scientific Instruments of the Czech Academy of Sciences, Brno, Czech Republic
[l]University of Florence, European Laboratory for Non-Linear Spectroscopy, Department of Biology, Florence, Italy
[m]National Institute of Optics, National Research Council, Rome, Italy
[n]Istituto Italiano di Tecnologia, Center for Biomolecular Nanotechnologies, Arnesano, Italy
[o]Massachusetts General Hospital, Harvard Medical School, Athinoula A. Martinos Center for Biomedical Imaging, Charlestown, Massachusetts, United States
[p]Sorbonne University, INSERM, CNRS, Institut de la Vision, Paris, France
[q]University of California San Diego, Department of Electrical and Computer Engineering, La Jolla, California, United States
[r]University College London, Department of Neuroscience, Physiology and Pharmacology, London, United Kingdom

sUniversity of California San Diego, Departments of Neurosciences, La Jolla, California, United States

tThe Hebrew University of Jerusalem, Institute for Medical Research Israel–Canada, Department of Medical Neurobiology, Faculty of Medicine, Jerusalem, Israel

uWeizmann Institute of Science, Department of Brain Sciences, Rehovot, Israel

vColumbia University, Zuckerman Mind Brain Behavior Institute, New York, United States

wCentral Michigan University, Department of Neuroscience, Mount Pleasant, Michigan, United States

xUniversity of Porto, Instituto de Investigação e Inovação em Saúde (i3S), Porto, Portugal

yUniversity of California Berkeley, Department of Physics, Berkeley, California, United States

zYale School of Medicine, Department of Radiology and Biomedical Imaging, New Haven, Connecticut, United States

aaCalifornia Institute of Technology, Andrew and Peggy Cherng Department of Medical Engineering, Department of Electrical Engineering, Pasadena, California, United States

abUniversity of California Berkeley, Departments of Chemistry and Molecular & Cell Biology and Helen Wills Neuroscience Institute, Berkeley, California, United States

acUniversity of Campinas, Institute of Physics, Campinas, São Paulo, Brazil

adInterdisciplinary Institute for Neuroscience University of Bordeaux & CNRS, Bordeaux, France

aeSalk Institute for Biological Studies, Waitt Advanced Biophotonics Center, La Jolla, California, United States

afUniversity of Florence, European Laboratory for Non-Linear Spectroscopy, Department of Physics, Florence, Italy

agHarvard Medical School, Howard Hughes Medical Institute, Department of Neurobiology, Boston, Massachusetts, United States

ahNew York University Grossman School of Medicine, Tech4Health and Neuroscience Institutes, New York, New York, United States

aiSorbonne University, INSERM, CNRS, Institut de la Vision, Paris, France

ajUniversity of California Santa Barbara, Department of Electrical and Computer Engineering, Santa Barbara, California, United States

akNew York University Langone Health, Departments of Ophthalmology and Radiology, New York, New York, United States

alBoston University, Departments of Electrical Engineering and Biomedical Engineering, Boston, Massachusetts, United States

amUniversity of California Davis, Department of Biochemistry and Molecular Medicine, Davis, California, United States

anRockefeller University, Laboratory of Neurotechnology and Biophysics, New York, New York, United States

aoThe Rockefeller University, The Kavli Neural Systems Institute, New York, New York, United States

apCenter for Neuroengineering and Therapeutics, Departments of Neurology, Bioengineering, Physical Medicine and Rehabilitation, Philadelphia, Pennsylvania, United States

aqCornell University, School of Applied and Engineering Physics, Ithaca, New York, United States

arCalifornia Institute of Technology, Departments of Electrical Engineering, Bioengineering and Medical Engineering, Pasadena, California, United States

asHarvard Medical School, Department of Neurobiology, Boston, Massachusetts, United States

atCarnegie Mellon University, Department of Biological Sciences, Pittsburgh, Pennsylvania, United States

---

*Address all correspondence to Anna Devor, adevor@bu.edu

†Present address C.G.L.F.: Varioscale, Inc., San Marcos, California, United States

‡Present address P.M.: Departments of Physics, UCSD, La Jolla, California, United States

††Present address Fr.P.: Departments of Pediatrics, UCSD, La Jolla, California, United States

§Present address S.S.: Illumina Inc., San Diego, California, United States

Abstract. *Neurophotonics* was launched in 2014 coinciding with the launch of the BRAIN Initiative focused on development of technologies for advancement of neuroscience. For the last seven years, *Neurophotonics*' agenda has been well aligned with this focus on neuro-technologies featuring new optical methods and tools applicable to brain studies. While the BRAIN Initiative 2.0 is pivoting towards applications of these novel tools in the quest to understand the brain, this status report reviews an extensive and diverse toolkit of novel methods to explore brain function that have emerged from the BRAIN Initiative and related large-scale efforts for measurement and manipulation of brain structure and function. Here, we focus on neurophotonic tools mostly applicable to animal studies. A companion report, scheduled to appear later this year, will cover diffuse optical imaging methods applicable to noninvasive human studies. For each domain, we outline the current state-of-the-art of the respective technologies, identify the areas where innovation is needed, and provide an outlook for the future directions. © *The Authors. Published by SPIE under a Creative Commons Attribution 4.0 International License. Distribution or reproduction of this work in whole or in part requires full attribution of the original publication, including its DOI.* [DOI: 10.1117/1.NPh.9.S1.013001]

Table of Contents

1 Introduction

The Neuron Doctrine formulated by Ramón y Cajal at the turn of the 19th century is an embodiment of neuroscience discovery empowered by optics. Cajal used Camillo Golgi's "black reaction" to sparsely impregnate neurons with light-absorbing silver nitrate in histological brain sections. Inspecting these sections with a light microscope, Cajal concluded that information was flowing in one specific direction—from dendrites to axons—within a network of discrete nerve cells connected by synapses. This conceptual advance, enabled through utilization of a light-absorbing probe in combination with widefield microscopy, laid the foundation for modern neuroscience. Fast-forward to the present day, and optical tools for measurement and manipulation of neuronal activity are so ubiquitous and versatile that "neurophotonics" has become a common word in the scientific vocabulary: we talk about neurophotonic technologies and research centers, we have the *Neurophotonics* journal, and recognize neurophotonics as its own field of research.

While optical methods have occupied center stage in neuroscience from the times of Cajal and Golgi, the last decade has seen a rapid advance of neurophotonic technologies, in large part thanks to the BRAIN Initiative[1,2] as well as other large-scale neuroscience projects in the US and around the world.[3] At the dawn of the BRAIN Initiative, the research community was deeply engaged in discussion about what kinds of tools were needed to accelerate neuroscience discovery. Questions were asked about the technological goals to maximize the progress in understanding the brain: Should we measure each spike in every neuron? Should we prioritize one model species over another? Should we pick one specific neuronal circuit and summon all forces to understand it as completely as we can? After intense debates in the media, townhall meetings and deliberations at the National Institutes of Health and beyond, the final answer was: We need it all! We need to understand the brain across scales, from its molecular composition to large-scale architecture, from single-cell gene expression to whole-brain activity patterns, and for each aspect of the brain's organization, we need to use those model species that make the most sense. Thus, we also need a variety of tools with which to tackle these different biological parameters and phenomena. Halfway through the BRAIN Initiative, we can safely say that this inclusive scope is paying off. We now have a large array of diverse experimental and computational tools to study the brain across species, scales, levels of description, in animals and humans. Notably, the lion's share of these technologies falls under the general umbrella of neurophotonics.

Here, we review the current state-of-the-art tools that are, in general, applicable to animal models and usually considered under the umbrella of microscopy. We start with an overview of high-resolution structural imaging tools that have emerged and/or matured within the last decade. Then, we highlight several newly developed optical sensors and modulators of brain activity followed by discussion of a suite of one-photon (1P) and multiphoton fluorescence

microscopy methods aimed at large-scale imaging of brain activity with high temporal resolution. We include a number of technologies for imaging cerebral blood flow and metabolism and feature several imaging approaches that integrate optical tools with other measurement modalities providing complementary information and/or helping to overcome fundamental limitations of purely optical methods. Finally, we highlight the importance of computational tools that complement optical technologies extending their capabilities.

Given the vast and rapidly expanding landscape of neurophotonic tools, the current scope is not exhaustive but rather biased on the collective scientific interest of this group of authors. Most often, these tools entail some level of invasiveness and in general are not applicable to live brain imaging in humans. A companion paper is focused on noninvasive (diffuse) optical imaging technologies targeted for humans.

2 Imaging of Microscopic Brain Structure

A singular advance that underlies the modern high-resolution, high-throughput imaging of labeled brain structures in animal species is the development of a diverse palette of bright, photostable fluorescent proteins.[4] These proteins are genetically encoded, which allows targeting of fluorescent labeling to specific cells, subcellular compartments, and biochemical events (e.g., gene transcription). In parallel, advancement of new biochemical methods of tissue index matching, building upon the original CLARITY protocol,[5] have enabled volumetric acquisition of samples as thick as the whole mouse brain. On the imaging side, light-sheet microscopy[6] has emerged as a method of choice for high-throughput acquisition of cleared brain samples.[7] Beyond the diffraction-limited resolution of light microscopy, a suite of super-resolution technologies has leveraged the principle of manipulating the 'on' and 'off' state of the fluorescent labels.[8,9] Expansion microscopy[10] provides an alternative solution for overcoming the diffraction limit by physically expanding the sample. Expansion microscopy can be used to view small structures, such as synaptic vesicles, with no need for complex super-resolution instrumentation, but, in contrast to the "classical" super-resolution methods, is not compatible with live imaging.

Complementary to fluorescent labeling, label-free imaging relies on intrinsic properties of brain tissue.[11–16] High-resolution label-free structural imaging is of particular relevance for human brain tissue, where expression of fluorescent proteins does not apply for neuroethics reasons. Label-free imaging techniques leverage optical phenomena of interaction of light with live and fixed brain tissue including autofluorescence, reflectance, birefringence (polarization and direction dependence of refractive index) that yields retardance and changes in light polarization and scattering.

2.1 Fluorescent Proteins

Naturally occurring fluorescent proteins (FPs) from various marine organisms, including the archetypical *Aequorea victoria* green FP (avGFP),[17] provide the foundation for all genetically encoded molecular probes for fluorescence imaging of brain structure and function used today. The gene for an FP is introduced into the tissues of a model organism and then transcribed and translated by the normal cellular machinery. Expression in specific neuronal cell types or brain regions can be achieved with appropriate combinations of gene enhancers and promoters, adeno-associated virus (AAV) serotypes and injection site, and recombinase-dependent expression strategies. Having inspired countless genetic manipulation strategies, numerous advances in microscopy, and the development of powerful functional imaging probes, FPs are the substrate upon which a vast ecosystem of neurophotonic technologies now flourish.

Essentially all FPs in use today have been engineered using their wild-type progenitors as a starting point (Fig. 1). Nature and natural evolution have played the biggest role in providing researchers with a diversity of FP-based tools, and undoubtedly there are many secrets yet to be revealed.[18] However, for adapting natural FPs to the unnatural demands of neurophotonic applications, laboratory engineering and directed evolution play essential roles. Such approaches have been overwhelmingly successful at providing a color palette of bright FPs for multi-color, multi-parameter imaging,[19] and monomeric FPs for use as minimally-perturbing fusion protein
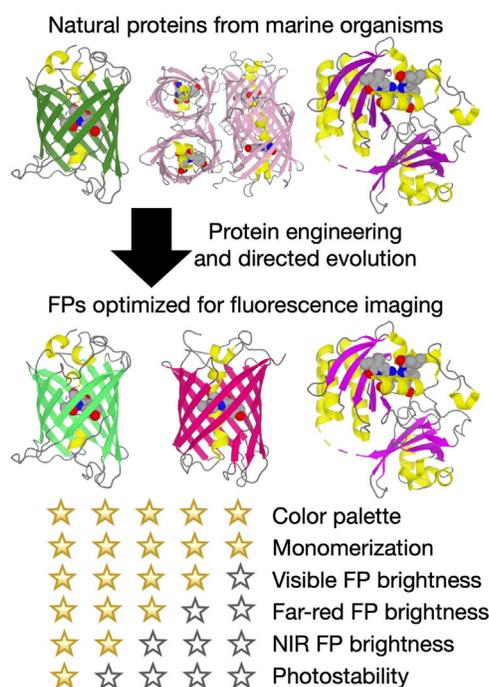
Fig. 1 Fluorescent protein engineering.

labels.[20] However, these efforts have been only partially successful at providing high-performance far-red FPs,[21] brightly fluorescent near-infrared FPs,[22] or substantial improvements in photostability.

Looking to the future, new protein engineering methods, or more intensive application of established methods, will be critical for overcoming these and other limitations. It is impossible to predict exactly which approaches are most likely to provide the next generation of FPs but, based on precedent, progress is certain to be achieved in a piecemeal fashion. For example, complementary approaches of particular promise include innovative library screening schemes[23] and rational computational design.[24] For some applications, alternative approaches such as semi-synthetic fluorogenic proteins,[25,26] and bright luciferase plus luciferin pairs,[27,28] may supplant FPs. In one form or another, FPs, or their functional equivalents, will remain at the forefront of neurophotonic research for the foreseeable future.

2.2 Tissue Clearing for High-Throughput, High-Resolution Imaging of Macrobiomolecules

Classic histological protocols for labeling of fixed tissue sections often include a step of dehydration followed by "clearance." In the process of dehydration, the water is removed and replaced by the alcohol (ethanol). In the process of clearance, a clearing agent (often methyl salicylate) is used to displace the ethanol while also removing fat molecules rendering the tissue optically transparent. In neuroscience, these protocols have been widely used in combination with bright field and epi-fluorescence microscopy for morphological analyses, i.e., for reconstruction of dendritic and axonal arbors across different neuronal cell types.[29] While useful, these methods were limited to relatively thin brain sections to allow the chemicals to penetrate throughout. In addition, uneven shrinkage of serial sections prevented stitching sections into volumes. More recently, transition to organic solvents has been proposed as a way to increase sample thickness enabling volumetric reconstruction.[30] However, the problem of uneven shrinkage remained. In addition, these solvents produced bleaching of endogenous fluorescence, and their toxic and corrosive nature required specialized equipment and handling. As an alternative, aqueous solutions with high refractive index were employed preventing bleaching but not achieving sufficient transparency for thick samples (reviewed in Ref. 31).
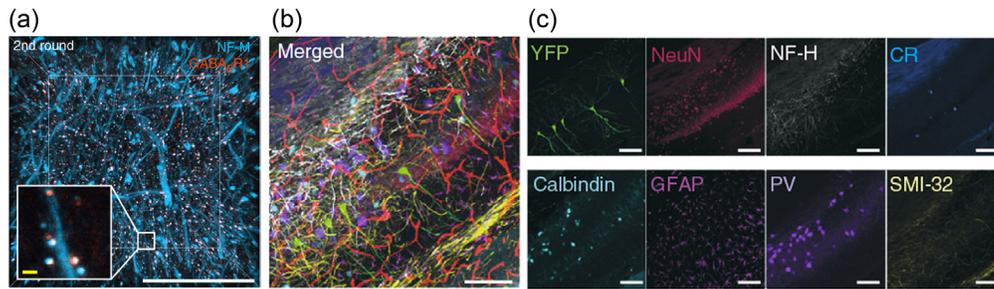
Fig. 2 Visualization of biomolecules in cleared tissue. (a) Imaging of neurofilament medium unit (NF-M) and GABAB receptor subunit-1 antibodies in cleared, expanded tissue. Scale bars, 50 μm. (b)–(c) Overlay of multi-round immunostained images. Scale bar, 100 μm. Panel (a) is adapted from Ref. 32; panels (b) and (c) are adapted from Ref. 33.

In 2013, development of CLARITY,[5] a method of making large volumes of tissue optically transparent and macromolecule-permeable using a hydrogel built from within, revolutionized brain histology. This method has broken ground for the development of a growing family of tissue clearing tools with varying hydrogel composition, including those that can repeatedly expand and shrink brain tissue[32] while preserving target macrobiomolecules.[33] In combination with light-sheet microscopy (Sec. 4.3), these methods allow high-throughput analysis of large-scale FP expression and also support multiplexed immunostaining with many rounds of fluorescent antibody labeling and stripping[34] (Fig. 2).

2.3 Super-Resolution Microscopy

Super-resolution microscopy refers to a new class of fluorescence imaging techniques that have shattered the diffraction barrier of light microscopy, offering spatial resolutions down to the single-digit nanometer range close to the ultimate limit, i.e. the size of the fluorescent molecules. Since their invention some 20 years ago (recognized by the Nobel Prize in 2014), a diversifying family of super-resolution methods has been developed and deployed in neuroscience research, including STED, RESOLFT, PALM, STORM, u-PAINT, and SIM, encompassing laser-scanning and widefield imaging modalities[35] (Fig. 3). While these techniques are quite distinct in design and use (concerning hardware, labeling, image analysis), they are all based on the principle of manipulating the 'on' and 'off' state of the fluorescent labels, whose spatial distribution can be read out in a diffraction-unlimited way.

In STED microscopy,[39] dye molecules are switched off by stimulated emission in a donut-shaped region around the excitation spot that scans the sample, shrinking its size. In PALM,
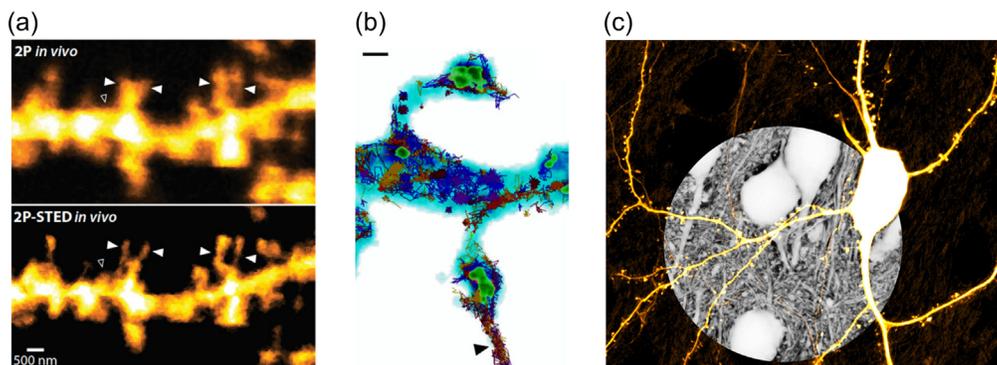
Fig. 3 Super-resolution imaging of fine neuronal structures. (a) Comparison of 2P *versus* 2P-STED image of dendritic spines imaged in the mouse hippocampus *in vivo* (adapted from Ref. 36). (b) Correlative STED and SMLM image of dendritic spine morphology and dynamic spatial arrangement of synaptic proteins (blue, neuronal morphology; green, PSD-95 scaffold protein; colored tracks, GluA1 receptor subunit), scale bar 500 nm (adapted from Ref. 37). (c) Super-resolution shadow imaging (SUSHI) of brain tissue, revealing anatomical context of a YFP-labeled neuron (adapted from Ref. 38).

STORM and u-PAINT, collectively referred to as SMLM (single-molecule localization microscopy), the fluorophores are imaged onto a camera, but not all at the same time. They are turned on so sparsely that each of them can be precisely localized. By acquiring thousands of images of different sets of activated fluorophores, a super-resolved image is constructed.[40]

These ground-breaking methods have enabled unprecedented optical access to subcellular organelles and protein arrangements in living brain cells and tissue preparations, unlocking a wealth of new and exciting biological information. For instance, they have revealed the ring-like organization of the cytoskeleton in axons,[41] the columnar arrangement of pre- and post-synaptic signaling proteins,[42] the structural plasticity of dendritic spines in the hippocampus,[36] as well as basic physical properties of the extracellular space of brain tissue.[43]

In the future, this technology will still develop rapidly in many key respects, allowing for more sophisticated experiments on more complex and biologically relevant samples, while also becoming less cumbersome and expensive. An important task is to make *in vivo* super-resolution imaging more of a reality, which faces special challenges in terms of depth penetration and brain motion. We can expect that recent technological advances, including those in adaptive optics and computational tools, will substantially potentiate the power of super-resolution microscopy and the biological insights that it will unearth.

2.4 *Expansion Microscopy*

The fundamental optical diffraction limit precludes the use of conventional light microscopy for imaging of nanoscopic structures such as the post-synaptic density. Expansion Microscopy (ExM)[44] overcomes this limitation by physically magnifying tissues while reserving or highlighting biomolecules such as proteins, nucleic acids, lipids, etc.[45,46]

The general workflow of ExM involves the following steps: (1) infusion and synthesis of a water-swellable hydrogel throughout the specimen; (2) chemically linking biomolecules of interest to the hydrogel; (3) homogenization of the specimen enzymatically or via heat denaturation, and (4) physical expansion of the specimen in pure water.[47] The workflow is designed to facilitate isotropic expansion.[10,44,48–51] Most ExM methods expand the specimen by up to $\sim4.5\times$ in the linear dimension. Using a conventional light microscope, such expansion provides ~60 nm image resolution for an objective lens with 270 nm diffraction limit ($270/\sim4.5 = \sim60$ nm). If protocols for $10\times$ expansion[52] or more[53] are used, the effective imaging resolution can be further improved to $\sim25 - 30$ nm.

This technology has been used to (1) study synapses in a number of model organisms including mouse brains[44,51] (Fig. 4), larval and adult *Drosophila* brains,[54,55] *C. elegans*,[56] planarian glia,[57] and larval zebrafish, revealing heterogeneity in synapse structure[58] and age-associated changes in active zones;[54] (2) trace neurons in large volume;[32,59] and (3) interrogate neurological diseases, such as Parkinson's disease,[60] schizophrenia,[61] and dementia,[62] discovering disease-related subtle structural changes[61,63] and protein mislocalization.[62]
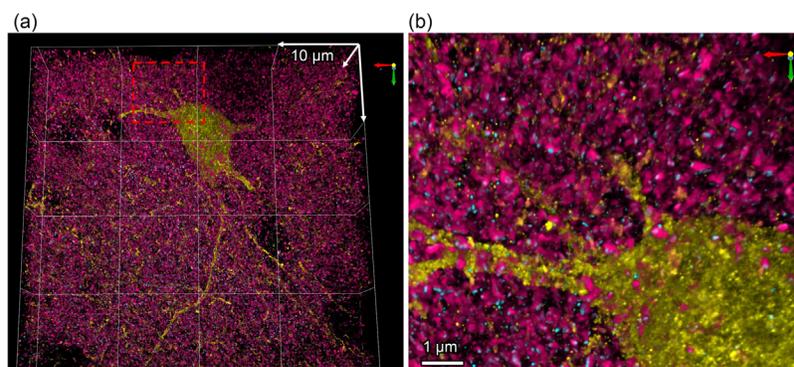
Fig. 4 Expansion microscopy imaging of synaptic proteins. (a) Volumetric image of an inhibitory neuron genetically labelled with EYFP in a $4\times$ expanded mouse brain section stained with antibodies against EYFP (yellow), synaptophysin (magenta) and PSD95 (cyan). (b) Zoom-in view from (a), as indicated by the dashed red box.

In the future, we expect ExM will further advance (1) labeling strategies to overcome the bottleneck in the signal strength that is diluted by expansion itself; (2) new gel chemistry that lead to larger expansion and better resolution; (3) multiplexing strategies to address the limitation of the 4–5 colors due to spectral overlap of fluorophores; (4) development of optical objectives and microscopes and the associated imaging software specifically for imaging expanded brains or other tissues. In the next decade, we envision researchers will be able to routinely acquire large volume and highly multiplexed nanoscale images of expanded neuronal tissue to quantify changes in synaptic components and other nanoscale structure in the brain, potentially providing new insights into the molecular mechanisms of neuronal function and disease.

2.5 Label-Free Structural Imaging Based on Interaction of Light with Tissue

While fluorescent proteins offer selective genetic targeting and multiplexing, these approaches are limited to animal studies where genetic manipulations and editing can be performed. Label-free imaging relies on intrinsic properties of brain tissue and applies to human cerebral tissue, freshly excised or fixed. Indeed, the biological structure autofluorescence produced by red blood cells retained inside the vessels, and the lipofuscin pigments present inside the neuronal bodies, can be detected by fluorescence microscopy techniques.[64] In addition, it is possible to modify the sample with specific preparations in order to increase the autofluorescence signals of particular structures. Among them, a recent protocol called MAGIC (Myelin Autofluorescence imaging by Glycerol Induced Contrast enhancement)[11] enables to perform label-free fluorescence imaging of myelinated fibers in various mammalian brains, including humans, with a glycerol-based tissue treatment (Fig. 5) allowing three-dimensional (3D) connectomics analysis of the brain.

Furthermore, optical methods based on different physical phenomena are extensively used to investigate both *in vivo* and *ex vivo* tissues. Raman scattering and its derivation as Coherent anti-Stokes Raman scattering (CARS)[65] permits to determine the molecular composition of every tissue. Second-harmonic generation (SHG) allows to detect well organized structures like collagen, myosin, or polysaccharides[66,67] while third-harmonic generation (THG) distinguishes the interface between different compartments like skin, neuron's myelin, and adipocyte.[68] Another label free technique that enables the high-resolution analysis of myelinated fibers is 3D-PLI
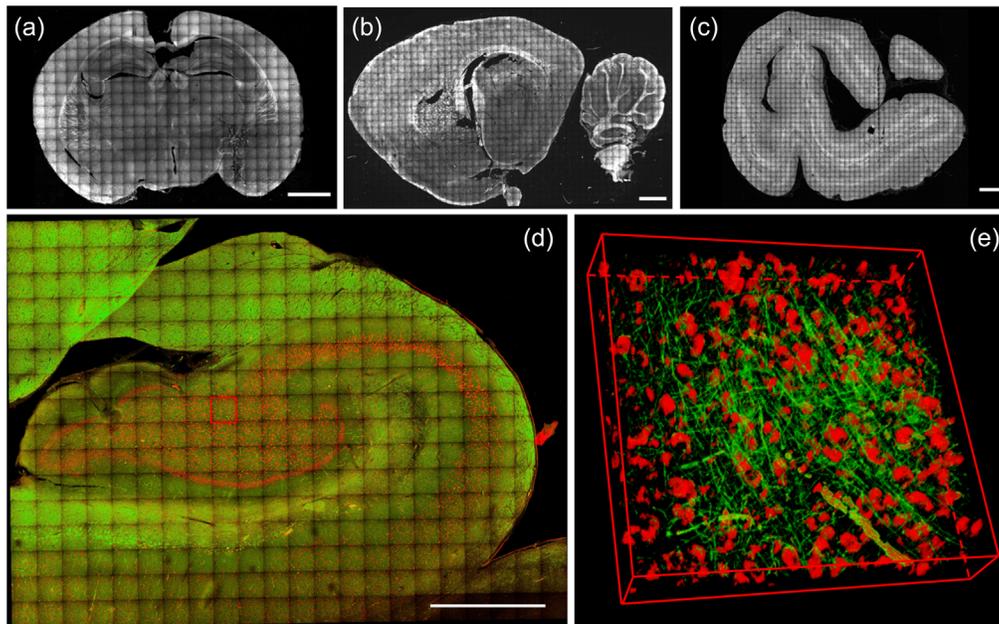
Fig. 5 Reconstruction of brain sections treated with MAGIC: (a) mouse, (b) rat, (c) vervet monkey, (d) and human. Scale bar = 1 mm. (e) 3D rendering ($450 \times 450 \times 60 \ \mu m^3$) of the stack indicated by the red box in d; green and red channels show the myelinated fibers enhanced by MAGIC and the autofluorescence of the cell bodies produced by lipofuscin pigments. Adapted from Costantini et al.[11]

(Polarized Light Imaging),[69] based on the detection of the birefringence of the myelin sheaths surrounding axons. In particular, this technique allows the reconstruction of the 3D organization of the whole brain fiber's architecture in thin slices.[70] Finally, reflectance microscopy[12,14] can be used to measure myelin contents and capillary blood flow in live preparations.

All these methodologies are usually linked together to obtain a multimodal mapping of the different tissue components.[65,71] We believe that in future some of the label-free techniques will be combined with specific tissue preparation and labeling, such as clearing methods,[31] as already done with CARS on mouse brain,[72] coupling the morpho-chemical label free analysis with labeled 3D volumetric imaging on large samples.[73,74] The combination of label-free methods with specific labeling will allow a more comprehensive analysis of tissue composition offering the possibility of molecular phenotyping at the cellular and subcellular level.

2.6 Optical Coherence Tomography

Optical coherence tomography (OCT)[75] is another label-free imaging modality that uses intrinsic contrast to generate cross-sectional or volumetric images of tissues at micrometer resolution. OCT differs from the above-mentioned label-free tools in that it employs low-coherence interferometry to provide depth-resolved images, for which light backscattered and reflected from a sample is mixed with a reference light. Not only the intensity, but also the phase and polarization of the detected light carry physical information. Various OCT-based techniques have been developed for different fields, such as ophthalmology, most notably, but also in cardiology, and dermatology, to visualize tissue structure and function.

OCT applications in the brain have been emerging in recent years.[76] Like the retina, many regions of the brain possess an internal organization which gives rise to natural differences in optical properties. The simplest example of this principle is the fact that white matter has a higher scattering coefficient than gray matter. On a finer scale, cellular composition, myelination, and potentially, axonal/dendritic content can also modulate scattering coefficients of individual layers in the cortical column.[77] Within gray matter itself, high resolution Optical Coherence Microscopy (OCM) imaging has revealed individual myelinated axons[78] and neuronal cell bodies,[77] and potentially cell nuclei.[79] Morphological changes can accompany cell death[80,81] and therefore inform about neuronal viability, while Aβ plaques are distinguished as being highly backscattering.[82] Finally, OCT is unique in enabling optical microscopic imaging more than 1 mm deep *in vivo* in scattering tissue, through minimally invasive preparations (Fig. 6), and can capture deep pathology that is missed by more superficial imaging techniques.[83] Functional and hemodynamic extensions of OCT are discussed in Sec. 6.1.

Interestingly, much of the intrinsic contrast of *in vivo* neuronal tissue is also apparent *ex vivo* in fresh[84] and to some extent, even fixed[85,86] tissues. This has enabled large-scale reconstructions of animal and human brains by serial optical coherence scanning (SOCS) that combines an OCT and a tissue slicer.[15] The SOCS is a new tool for fundamental research into the anatomical and connectional architecture of the brain without using exogenous contrast agents or expression of foreign genes. It relies on conventional or polarization-sensitive OCT of a volume within the field of view, translating the sample laterally to image neighboring volumes, removing a layer of tissue using the slicer to expose deeper regions for imaging, and repeating these steps until the entire block is imaged. Consequently, the SOCS provides large datasets for brain imaging and mapping, and the data size is proportional to the sample volume and inversely proportional to the volumetric spatial resolution. The latter can be enhanced by utilizing OCM. The technology has been used to distinguish the gray matter and white matter,[87] compared with Nissl staining[86] and diffusion MRI,[88,89] and applied on the rat brain,[15] mouse brain,[13,90–92] and human medulla oblongata.[88] Figure 7 shows the power and promise of the *ex vivo* SOCS method, as it shows axon fibers of mouse brainstem and cerebellum and delineates the cerebellar layers without histological processing.

While *ex vivo* OCT provides intrinsic contrast, it is most powerful when complemented by other, more specific histological or labelled imaging techniques. In the future, we can expect the use of SOCS to complement other serial imaging modalities in creating unique and undistorted datasets from rodent, nonhuman primate, and human brains. Development of image processing and analysis tools will allow creation of new brain atlases and better understanding of the
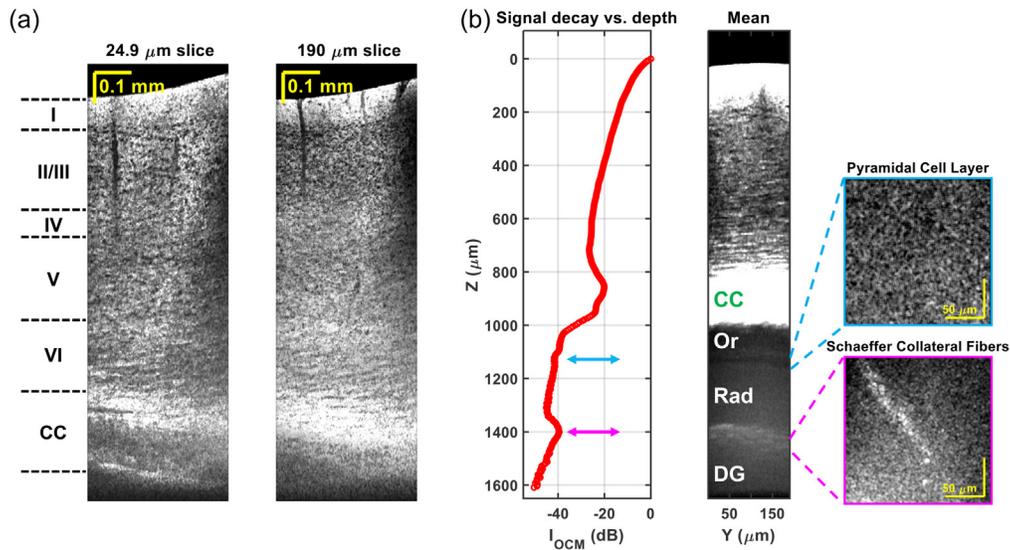
Fig. 6 *In vivo* 1700-nm optical coherence microscopy (OCM) of the mouse brain through a thinned skull preparation. (a) Minimum intensity projection sagittal images, or "slices," with different projection thicknesses in the coronal direction, show cortical cytoarchitecture and the corpus callosum (CC), without physical tissue slicing. (b) OCM signal decay (left panel) and averaged coronal image (middle panel) show sub-cortical layers. CC, corpus callosum; Or, stratum oriens; Rad, stratum radiatum; DG, dentate gyrus. Adapted from Zhu et al.[83]
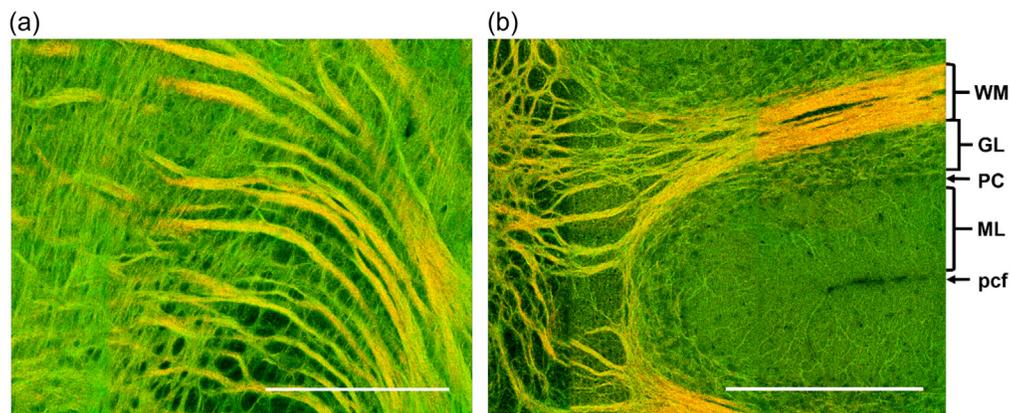
Fig. 7 *Ex vivo* serial optical coherence scanning (SOCS) of the mouse brain. (a)–(b) Composite images with reflectivity (green) and retardance (red) contrasts for selected regions in mouse brainstem (a) and cerebellum (b). WM, white matter; GL, granular layer; ML, molecular layer; pcf, preculminate fissure. PC indicates a layer of Purkinje cell bodies whose dendrites reside in ML. Scale bar: 320 μm (length of a square tile).

connectome. These could facilitate studying atrophies in brain diseases[93] and finding new targets for neuromodulation treatments. The necessity of serial imaging and analysis of big data would require implementation of automated protocols to realize these highly significant goals.

3 Molecular Sensors and Actuators for Imaging and Manipulation of Brain Activity

Recent advances in molecular engineering have led to several families of high-quality optical sensors. We use the terms "sensor," "indicator," and "probe," interchangeably, to broadly describe molecules that provide a measurable signal in response to changes in brain activity. Following the traditional definition of the term in the analytical sciences, we use "biosensor"

to refer to only those sensors in which a protein component is detecting the biological change of interest. Combined with advanced microscopy, calcium ion (Ca^{2+}) imaging using GCaMPs[94] is now routinely employed to enable large-scale, single- or multiphoton imaging for readout of neuronal circuit activity in awake, behaving animals.[95,96] In parallel, voltage sensors have been significantly improved in recent years in terms of intrinsic properties such as membrane localization, brightness, sensitivity and kinetics. These voltage sensors can be divided into three general categories: synthetic sensors,[97] hybrid biosensors that use a combination of synthetic dyes and genetically encoded proteins,[98] and fully genetically encoded biosensors.[99–101] Synthetic voltage sensors have a long history in neuroscience including the latest red-shifted photoinduced electron transfer (PeT) highlighted below.[102] Hybrid voltage biosensors combine molecular specificity of genetically encoded proteins with unsurpassed photophysical properties of synthetic fluorophores. Genetically encoded voltage biosensors are based on either opsins or voltage sensing domains; the most recent of them approach the performance of their synthetic counterparts.[103] The choice of voltage sensor is driven by applications, and no single solution fits all.[104]

Beyond Ca^{2+} and voltage, more recent protein engineering efforts have now extended the concept of single-FP based biosensors to the design of genetically encoded biosensors for neurotransmitters and neuromodulators, including glutamate, GABA, dopamine, norepinephrine, serotonin and acetylcholine, based on either G-protein coupled receptors (GPCR) or bacterial periplasmic binding proteins (PBP).[105] These biosensors enable measurements of neurotransmitter release with high spatiotemporal resolution and molecular specificity across the full course of behavioral paradigms.[106–117]

With growing appreciation for the concepts of the neurovascular unit[118] and tripartite synapse,[119] there has been a concerted effort for development of fluorescent biosensors for cellular metabolism,[120,121] and targeting these and other biosensors to not only neurons but also non-neuronal cells including astrocytes (as well as immune and vascular mural cells).[122]

The sensors mentioned above, whether genetically encoded, hybrid or synthetic, employ fluorescence to report activity. Another notable form of luminescence is phosphorescence that has a longer lifetime and thus occurs on a slower time scale. Phosphorescence has been traditionally employed in sensing O_2, a physiological parameter of key importance in the brain and elsewhere.[123] Development of new 2P-excitable, red-shifted probes has recently enabled deep intravascular and tissue imaging of the partial pressure of O_2 (pO_2).[124,125]

Fluorescence and phosphorescence require that photons are delivered to the chromophore/phosphor molecule to induce emission. In bioluminescence, in contrast, emission of light occurs in the process of a chemical reaction where an enzyme oxidizes a substrate.[126] Bioluminescence has been recently harnessed to generate biosensors though functional reconstitution in the presence of target molecules.[127] It also has been explored for actuation by using emitted light to stimulate light-sensing proteins.[128] Although the concept of bioluminescent actuators is very new, this work already has yielded promising results.[129] Bioluminescent actuation joins optogenetics, a widely used tool for stimulation and inhibition of neuronal activity that has revolutionized neuroscience since its invention in 2005.[130,131]

3.1 Calcium Sensors

Ca^{2+} measurements are central in neuroscience due to the importance of Ca^{2+} in cellular excitability and intracellular signaling pathways.[132] A correlation of Ca^{2+} signals with electrophysiological measurements of membrane potentials across neuronal compartments (soma, proximal dendrites, distal dendrites) has been demonstrated using simultaneous intracellular electrophysiological recordings.[133,134] This is due to abundant expression of numerous types of voltage-gated Ca^{2+} channels.[135–137]

Imaging of neuronal activity using Ca^{2+} sensors was originally enabled by Roger Y. Tsien and colleagues who developed the fura-2 synthetic Ca^{2+} indicator dye and the means to deliver this dye to tissues in the form of an acetoxymethyl (AM) ester.[138,139] Following these initial breakthroughs, examples of Ca^{2+} imaging to record neuronal activity soon started to appear.[140,141] Ever since, the development of improved Ca^{2+} sensors has been a steadily evolving area in neuroscience due to arrival of new indicators with improved signal to noise ratio
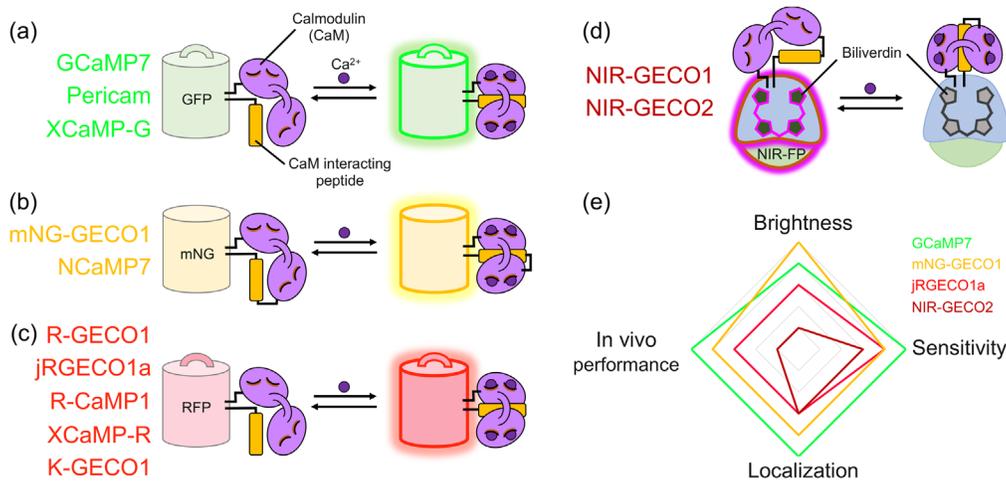
Fig. 8 Overview of available intensiometric single FP-based GECIs. (a) Representative GFP-based GECIs.[159,163,164] (b) Representative mNeonGreen-based GECIs.[165,166] (c) Representative RFP-based GECIs.[164,167–169] (d) Representative near infrared FP-based GECIs.[170,171] (e) Qualitative assessment of various GECIs in terms of brightness, sensitivity, localization and *in vivo* performance.

(SNR) properties, low toxicity, and optimized delivery strategies. Of particular note was the development of an exceptionally good Ca^{2+} indicator Oregon Green BAPTA-1 (OGB-1), and a clever scheme of delivering its AM ester form into thick tissues.[142] Thanks to large 2P absorption cross-section of OGB-1 and other synthetic Ca^{2+} sensors, *in vivo* 2P Ca^{2+} imaging has been widely adopted within the neuroscience community and used for studying of neuronal circuits in healthy cerebral[143–147] and cerebellar cortex,[148] spinal cord,[149] olfactory bulb,[150,151] in glial cells,[152–154] and in diseased brain.[155,156]

Relative to synthetic indicator dyes, genetically encoded Ca^{2+} indicators (GECIs; a.k.a. Ca^{2+} biosensors) offer a number of advantages including genetic targeting to specific cell types, virus-mediated delivery, and the possibility of creating transgenic organisms that stably express the GECI. Just as with the field of synthetic Ca^{2+} indicator dyes, the field of GECIs was enabled by the work of Roger Y. Tsien and colleagues. Specifically, they reported the Förster resonance energy transfer (FRET)-based cameleon Ca^{2+} biosensor in 1997[157] and the single GFP-based camgaroo Ca^{2+} biosensor in 1999.[158] These were soon followed by the improved single FP-based pericam[159] and GCaMP[160] biosensors which were composed of a circularly permuted GFP fused to calmodulin (CaM) and a CaM-interacting peptide.[161] The first GECI that was widely used to image neuronal activity in defined cell populations was GCaMP3,[162] and seventh generation GCaMP variants have been reported.[163] As the toolbox of genetically encoded Ca^{2+} biosensors continues to grow (Fig. 8), it is desirable to engineer biosensors with non-overlapping spectra to simultaneously monitor multiple circuit elements. Towards this goal, there are now a number of red FP-based[167–169] and near-infrared FP-based[170] Ca^{2+} biosensors available, though they do not offer the same outstanding levels of performance achievable with the latest generation of the highly optimized GCaMPs. However, these red-shifted probes offer the advantage of decreased scattering and absorption effects in tissue, thus allowing for deeper and more efficient imaging *in vivo*.

GECIs remain the workhorse of circuits-to-behavior neuroscience studies. The development and application of brighter and colorful Ca^{2+} biosensors along with other molecular tools will push the boundaries of exploration in neuroscience beyond the current limits.

3.2 *Synthetic Voltage Sensors*

Traditionally, neuronal electrical properties have been evaluated using intracellular electro-physiological recordings that are highly accurate but also terminal, invasive, low-throughput and labor intensive, and particularly difficult to perform in the brains of behaving mammals.
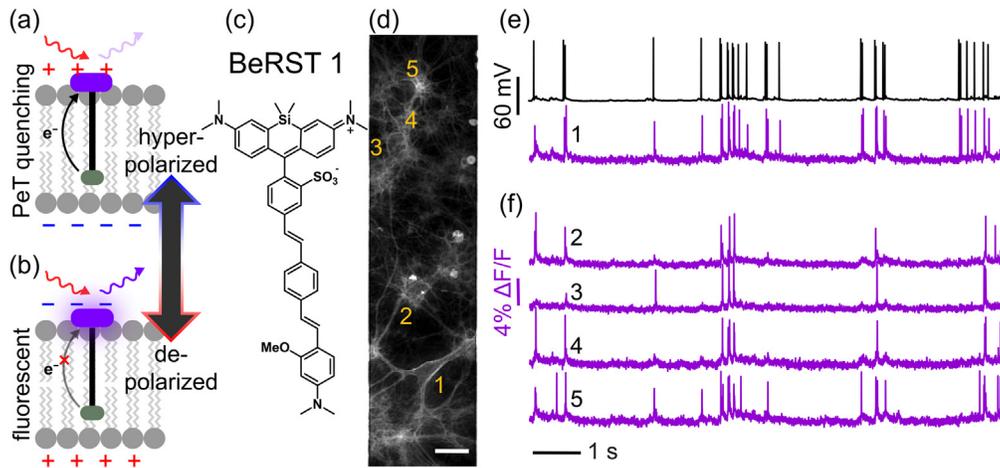
Fig. 9 Voltage imaging with PeT sensors. (a)–(b) Mechanism of voltage sensing in PeT-based voltage-sensitive fluorophores. (c) Structure of a prototypical voltage-sensitive fluorophore, Berkeley Red Sensor of Transmembrane potential, BeRST 1. (d) Fluorescence image of cultured hippocampal neurons loaded with BeRST 1. Scale bar is 20 μm. (e)–(f) Example traces from simultaneous electrophysiological (black) and optical recording (magenta) of spontaneous voltage fluctuations from neuron 1 (e) and spontaneous activity from neurons 2 to 5 (f); the corresponding neurons are labeled in (d). Adapted from Walker et al.[178] and Liu and Miller,[179] © 2020 American Chemical Society.

Synthetic sensors (dyes) provided an early impetus for probing transmembrane neuronal potential with optical imaging as an alternative to electrophysiological recordings. Nearly 50 years ago, experiments in squid axons revealed changes to the optical properties of dyes in response to membrane potential changes.[172] Since that time, efforts to design fluorescent dyes that respond to biological membrane potential broadly fall into two different camps: slow-response dyes that display voltage-dependent partitioning within the membrane, and fast-response dyes whose optical properties are modulated by changing electric fields.[173] Voltage-sensitive dyes are especially useful in model systems that lack ready tools for genetic manipulation and have been used extensively for mapping brain function in mammals and non-human primates.[174]

More recently, voltage-sensitive fluorophores based on voltage-sensitive photoinduced electron transfer (PeT)[175,176] have emerged as another avenue for synthetic voltage sensors[177] (Fig. 9). Changes in membrane potential alter the rate of PeT within the donor-acceptor framework of the dyes. At hyperpolarized potentials, PeT from an electron-rich aniline donor is accelerated by the hyperpolarized potential, preventing emission of a photon from the fluorophore excited state, and quenching fluorescence [Fig. 9(a)]. At depolarized potentials, the inverted membrane potential inhibits PeT and the dye brightens [Fig. 9(b)].[179] The newest PeT-based indicators compare favorably to genetically encoded indicators, in terms of speed, sensitivity, and brightness.[180] Additionally, the positive-going, turn-on response to action potentials, coupled with compatibility with multiphoton excitation,[102,181,182] make PeT-based synthetic voltage indicators an attractive method for imaging rapid membrane potential changes in intact brains. However, an outstanding problem is delivery of fluorescent dyes to specific cells.

In the future, a number of innovations could improve the utility of chemically-synthesized voltage indicators: improved or universal methods of delivery into intact brains; enhanced photo-stability for long-term imaging; larger multiphoton excitation cross-sections for use with 2P and 3P imaging; chemical-only cell targeting, without the requirement for genetic encoding, for example, by targeting native receptors;[183,184] longer wavelength indicators for *in vivo* imaging;[185,186] and, possibly, indicators that harness modalities other than light for noninvasive imaging.

3.3 *Hybrid Voltage Sensors*

Hybrid voltage sensors address the challenge of targeting fluorescent dyes to specific cell types. Multiple hybrid strategies have been explored. One attempt was using a "pro-drug" strategy in
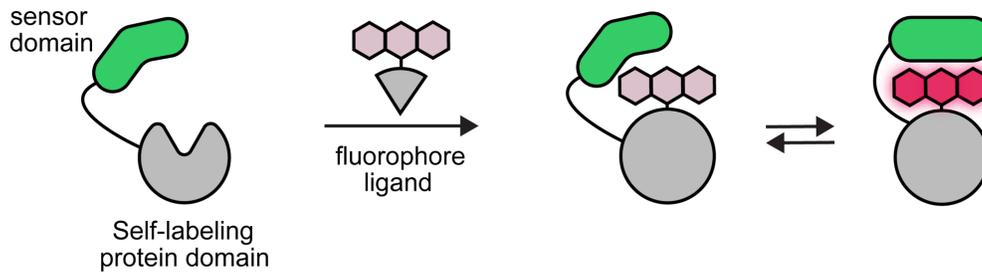
Fig. 10 Schematic of chemigenetic probes. A biosensor domain is attached to a self-labeling domain that irreversibly binds a fluorophore ligand. A change in the biosensor domain alters the bound fluorophore properties allowing functional recording of biochemical signals.

which a genetically encoded enzyme on the cell surface uncages a modified fluorescent voltage indicator.[187,188] Fluorescein-based voltage-sensitive fluorophores can be adapted to this strategy,[189,190] but the method has yet to be applied beyond cultured neurons. Alternatively, voltage-sensitive fluorophores can be tethered to neuronal surfaces with genetically-encoded, self-labeling enzymes to enable fast voltage imaging from defined cells and sub-cellular structures as was demonstrated in cultured hippocampal neurons[191–193] or brain slice.[193] Voltage indicators based on rhodamines can also be targeted in a similar fashion, allowing single-trial detection of action potentials in mouse brain slices.[193]

Recent efforts have introduced another solution to the problem of cell-type-specific targeting through engineering "chemigenetic" probes that couple simple synthetic fluorophores acting as the reporter molecule with a sensor protein domain partner. In chemigenetic probes, a sensor protein domain is appended to a self-labeling protein domain[98,194,195] such as HaloTag[196,197] that irreversibly binds a synthetic fluorophore ligand (Fig. 10). This allows genetic encoding of the protein portion and uses simple and cell-permeable small-molecules, such as Janelia Fluor (JF) dyes,[25,198] as reporter fluorophores.

Chemigenetic probes are engineered so that a change in the sensor protein domain alters the local environment around the dye and changes its fluorescence properties (Fig. 10). This approach yielded bright and photostable voltage and Ca^{2+} probes with highly tunable photophysical and chemical properties.[98,194,195] Chemigenetic voltage probe Voltron[98] increased photon yield from voltage imaging experiments to enable recording from many cells simultaneously. HaloCaMP and HASAP[195] are bright far-red Ca^{2+} and voltage probes that push the useful imaging spectrum to longer wavelengths. These recent developments provide a template for the design of new fluorescent probes for different analytes and biochemical processes.

Further advances in synthesizing tunable far-red dyes, alongside innovative protein engineering for building protein scaffolds able to modulate dye fluorescence, promise to enable functional imaging deeper in tissue. Moreover, improved bioavailability of dyes will allow routine imaging in live animals. Another equally exciting avenue is to develop orthogonal self-labeling proteins like HaloTag that work well *in vivo* with corresponding bioavailable ligands for multicolor imaging.

3.4 *Genetically Encoded Voltage Biosensors*

Recent advances in the development of genetically encoded voltage indicators (GEVIs, a.k.a. voltage biosensors) have led to significant improvement in their optical properties offering recording of transmembrane voltage via fluorescence imaging without the need to deliver extrinsic (synthetic) sensors or fluorophores. In particular, a few recent GEVIs, including SomArchon, QuasAr3, ASAP3 and Ace2N have achieved sufficient sensitivity to capture individual action potentials in behaving mice.[99,100,199–201] Figure 11 shows an example of voltage imaging of multiple cells simultaneously using SomArchon, which allows for the detection of individual action potentials and subthreshold membrane voltage fluctuations in behaving mice.[99] Additionally, since SomArchon operates at the near-infrared wavelength, it can be used in conjunction with blue-light-activated optogenetic actuators for simultaneous voltage imaging and optogenetic control.
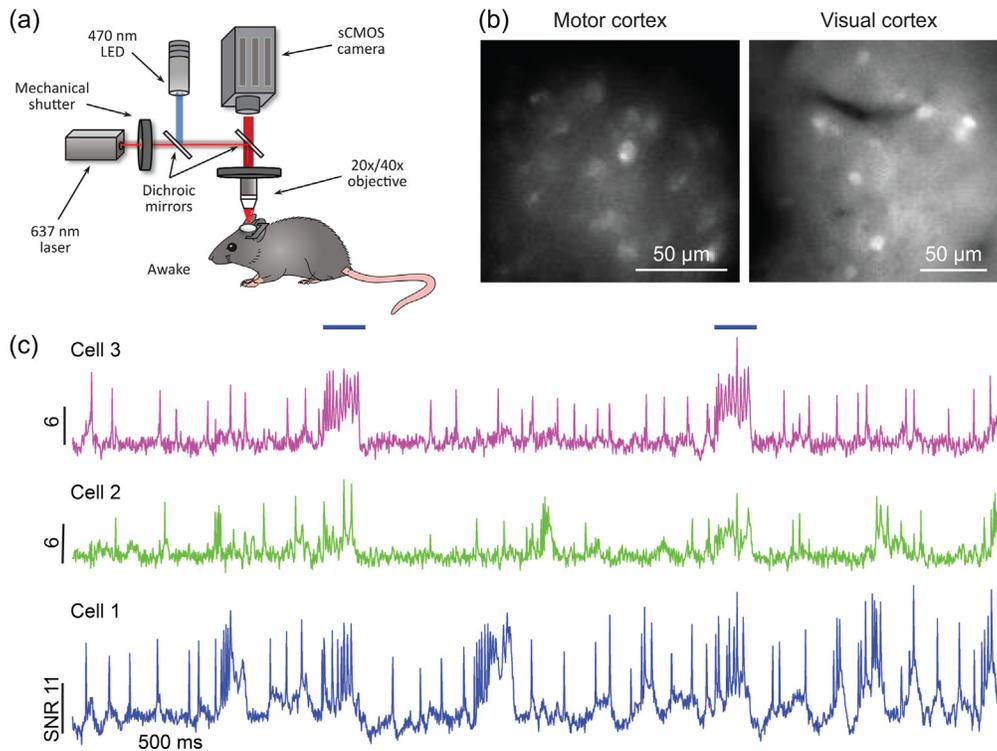
Fig. 11 Single cell voltage imaging in awake mice using a wide-field imaging setup. (a) Experimental setup: awake mice were head-fixed under a wide-field microscope. (b) Representative SomArchon-expressing neurons visualized via EGFP fluorescence in cerebral cortex. (c) Voltage imaging time-courses from three representative neurons in hippocampus; horizontal bars denote optogenetic stimulation. Reproduced with permission from Piatkevich et al.[99]

Several different types of GEVIs exist (for a recent comprehensive review, see Ref. 202). SomArchon and QuasAr3 are opsin-type GEVIs that use the voltage-dependent protonation of opsins as an optical readout. Indicators like Ace2N use an opsin to sense transmembrane potential, and changes in the protonation state of the opsin change the efficiency of energy transfer to a bright fluorescent protein (FP). ASAP3 is an FP fusion with a voltage sensitive protein domain which undergo conformational transitions upon transmembrane voltage fluctuations. These conformational changes are translated to the FP and change the fluorescence intensity of the FP.[203–209] GEVIs have been used to tackle intriguing scientific questions, such as how spiking activity of specific neuron types is modulated during different behavioral processes and relate to subthreshold membrane voltage fluctuations and extracellularly measured local field potential dynamics.

With continued improvement in both voltage sensors' molecular designs and optical instrumentation in the coming years, we expect that voltage imaging will be increasingly accessible to neuroscientists for high-speed kilohertz analysis of many individual neurons during behavior. Such capability will enable time-resolved analysis of transmembrane voltage, both action potentials and subthreshold membrane fluctuations, of distinct cell types and cell compartments in behavior and pathology. Finally, combining voltage imaging with other precision analysis technologies, such as cellular Ca^{2+} imaging and cell-specific proteomic and transcriptomic analysis, neuroscientists will be able to link the voltage dynamics of specific neurons and brain circuits to their cellular and biochemical states and tissue environment.

3.5 *Genetically Encoded Biosensors for Neurotransmitters*

The development and refinement of genetically encoded Ca^{2+} and voltage indicators have paved the way for the development of genetically encoded biosensors for neurotransmitters,

neuromodulators, and neuropeptides. Such biosensors are categorized by two scaffolds: microbial periplasmic binding protein (PBP) and G-protein coupled receptors (GPCR) [Figs. 12(a)–12(b)].

Microbial PBPs form a large protein superfamily that bind numerous classes of small molecules and peptides. Ligand binding in PBPs induces a large Venus flytrap-like conformational change, which is highly conserved [Fig. 12(a)]. These unique features have been used to develop a toolkit of highly sensitive sensors for other neurochemicals, including GABA (iGABASnFr), ATP (iATPSnFR), acetylcholine (iAchSnFR) and nicotine (iNicSnFr).[211–214] However, there are several analytes for which bacterial PBPs do not exist. Recently, a PBP-based biosensor iSeroSnFr for serotonin has been engineered using machine-learning-guided evolution of an existing PBP-based biosensor, iAchSnFr,[211] to redesign its binding pocket to report serotonin release at physiological concentrations.[215]

As an alternative to PBP-based biosensors, biosensors for neuromodulators have been developed by fusing GPCRs with fluorescent proteins, leveraging on ligand specificity, affinity, and binding kinetics that has evolved in the GPCRs. The first generation of GPCR-sensors were FRET-based.[216–219] However, use of these biosensors *in vivo* has been limited due to low dynamic range and sensitivity. GPCRs have seven transmembrane (TM) alpha helices, where the largest conformational change upon activation is thought to occur for TM domains 5 to 7.[220] Thus far, circularly permuted FPs (cpFPs) have been inserted in the intracellular loop 3 (IL3) domain of GPCRs, which bridges TM5 and TM6, to detect this conformational change upon ligand binding [Fig. 12(b)]. Using this versatile strategy, the Light and GRAB sensor family, consisting of dopamine, norepinephrine, and serotonin biosensors, has been developed and applied for *in vivo* recording of neuromodulator dynamics[210,221–226] [Fig. 12(c)]. In addition, red-shifted color variants of dLight1 was engineered for multiplexed neurochemical detection (Patriarchi et al., 2020). GRAB biosensors have also been expanded to acetylcholine, adenosine and more recently endocannabinoid.[224–226]

The intrinsic properties of these neurotransmitter biosensors demand further iterative optimization to be broadly applied to study spatial and temporal patterns of activity in synaptically connected neuronal circuits. Computational modeling would provide theoretic guidance for future optimization. In addition, a high-throughput screening system using fluorescence-activating cell sorting (FACS) combined with image-based screening or the well-known CRISPR/Cas9 system is a pressing need to speed up the process of optimization. Extending the sensitivity, specificity, and color palette of these biosensors will continue to create rich opportunities for studies aimed at understanding the role of specific neurotransmitters in calculations performed by neuronal networks.
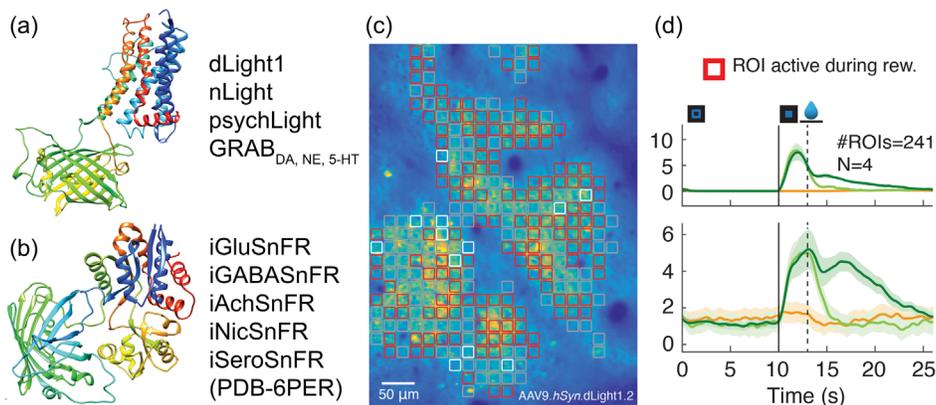
Fig. 12 Genetically encoded sensors for neurotransmitters. (a)–(b) Design scaffolds for sensors based on cognate GPCR (a) or *E. coli* PBP (b). (c) 2P imaging of dopamine dynamics in the mouse cortex using dLight1.2 when mouse performs a visual-motor learning task. Heat map of dLight1.2 expression pattern in layer 2/3 of M1 cortex is overlaid with computationally defined regions of interest colored by the type of responses observed during the task. (d) Average task-induced dLight1.2 transients (bottom) and mouse running velocity (top) aligned to trial onset (0 s). For details see Ref. 210.

3.6 *Molecular Probes for Cell Metabolism*

Brain metabolism is highly dynamic, fluctuating with the local level of neuronal activity and with consequent energy demands. Substantial amounts of ATP are required to support the ion gradients that serve as the batteries for electrical activity, and energy is also needed to support neurotransmitter release and recycling. This energy is provided mainly by the metabolism of glucose, although other fuel molecules can also contribute. Individual brain cells also can differ substantially in their metabolic demands and responses: not only may there be differences between different classes of neurons, but various glial cells—astrocytes (the focus of Sec. 3.7) and oligodendrocytes—may play specific roles in energy metabolism.

Because the metabolic responses are rapid (a few seconds to a few minutes) and can be localized to individual cells and subcellular compartments, imaging of fluorescent biosensors can be the ideal approach to investigating how cellular brain metabolism works. Genetically encoded biosensors have been developed for glucose[227–230] and ATP;[231–233] for the key electron-carrying cofactors $NADH/NAD^+$ (Fig. 13) and $NADPH/NADP$[234–237] and for the metabolic intermediates pyruvate[238] and lactate.[239] These have been imaged both *in vitro* and *in vivo* to elucidate metabolic responses in neurons and astrocytes,[240,241] though some features remain quite controversial.

A particular challenge for using metabolic biosensors is that quantitative readouts are essential for interpretation; unlike the ubiquitous Ca^{2+} biosensors used to monitor neuronal activity, for which the temporal pattern itself is informative, metabolite levels must be compared between different cells and different conditions, even when biosensor expression levels vary. Ratiometric imaging can be used to normalize for expression levels, but ratio imaging requires more spectral bandwidth and reduces the opportunity for multiplexing several biosensors; excitation-ratiometric measurements can be challenging for scanning microscopes; and single-FP ratiometric biosensors also tend to be quite pH sensitive.[120] A valuable alternative is to use fluorescence lifetime imaging: the lifetime readout is independent of biosensor concentration, and rapid lifetime imaging is increasingly practical.[120,241,242] Lifetime-based biosensors are slightly harder to develop,
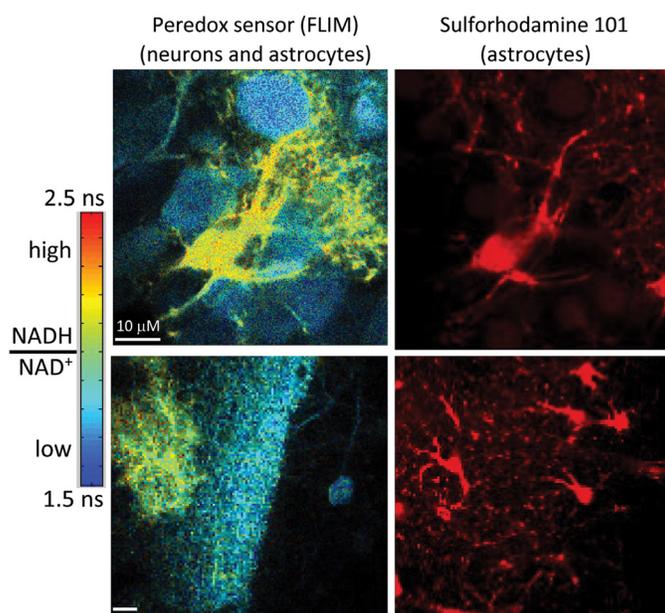
Fig. 13 Metabolic imaging of the Peredox biosensor of $NADH/NAD^+$ redox, expressed in neurons and astrocytes of acute hippocampal slice. Left: pseudocolor images of the biosensor, which reports high $NADH/NAD^+$ ratio as increased fluorescence lifetime. Right: counterstain with sulforhodamine 101 marks astrocytes specifically and shows that they are the cells with elevated $NADH/NAD^+$ levels in the left-hand images, while neurons have lower levels. Not all cells in the slice express the genetically encoded biosensor, which was introduced with a viral vector. See further discussion of astrocytes in Sec. 3.7.

but the ability to multiplex and to get instrument-independent quantitation makes them a valuable target for biosensor development in the coming years.

3.7 *Sensors for Astrocytes*

Astrocytes are one of the major non-neuronal cell types in the mammalian central nervous system (CNS), comprising up to 20% of the human brain.[243] Astrocytes are found throughout the CNS in non-overlapping domains.[244] These cells possess a characteristic morphology, with a central cell body radiating numerous membranous processes, which extend out into the neuropil interacting with neurons, other glia, and blood vessels.[243] Astrocytes are electrically silent, which meant that for many years they were dismissed as being merely parenchymal support cells – or "brain glue." The development of new optical imaging tools and their application to astrocytes has forced a dramatic rethink of this preconception.[122] Indeed, *in situ* imaging experiments, performed largely in acute tissue slices from rodents, have provided compelling evidence that astrocytes are key components and regulators of neuronal circuits.

Use of small organic ion-sensitive dyes and genetically encoded biosensors has demonstrated that astrocytes contribute to local synaptic homeostasis, through active buffering of Na^{+}[245] and K^{+}.[246] Meanwhile, use of metabolic biosensors suggests that astrocytes also act as "power plants," supplying lactate (a key energy substrate) to neurons.[240] Astrocyte-specific expression of genetically encoded neurotransmitter biosensors has shown that these cells are well placed to sense local neuronal activity and neurotransmitter release;[247] crucially, structural imaging of membrane-associated fluorescent proteins,[248] and tagged glutamate transporters,[249] suggests this activity can also trigger dynamic changes in astrocyte processes, which reciprocally modulate synaptic transmission. Such modifications may well be linked to transient increases in cytosolic Ca^{2+}, which are also evoked by local neuronal activity, and which, under certain circumstances, are thought to trigger the release of neuroactive substances (gliotransmitters) from astrocytes that act to modify neuronal activity.[250]

This multifaceted modulation of neurons and synapses by astrocytes suggests these cells provide an additional layer of information processing to that occurring in neurons, one which appears crucial to the modulation of animal behavior.[251] However, the role of astrocytes is complicated by the recent discovery of astrocyte subtypes, which exist both between and within brain regions.[252] These subtypes show differences at the molecular, anatomical and physiological levels, and are likely specialized to match and regulate local neuronal circuits[253] (and see Fig. 14).

Future work will benefit greatly from genetic tools (e.g. new Cre- mouse lines or viral vector systems) that allow precise targeting of these astrocyte subtypes,[255] including in gene knockout models. These will allow the contribution of astrocyte subtypes to local circuit function to be studied in great depth. Such work will also benefit from more specific methods for the acute and chronic manipulation of astrocyte activity,[256–258] as well as an expanded/comprehensive palette of sensors, allowing the mechanistic basis of astrocyte function to be elucidated. Such a toolbox will, of necessity, include sensors for ions, receptor activation (particularly G protein-coupled receptors), metabolic functions and key intracellular signaling pathways (including aspects of structural plasticity and mRNA/protein trafficking).[259,260]

Ideally, such probes will allow high levels of multiplexing (single wavelength probes) and be optimized for *in vivo* use (good signal-to-noise ratio, sensitivity, dynamic range, stability in the cellular environment, resistance to photobleaching, lack of toxicity, etc.), as recent work has demonstrated that astrocyte function is strongly influenced by behavioral state.[261] Probe development will go hand-in-hand with improvements in head-mounted camera technology for use in awake behaving animals (e.g., UCLA miniscope project) and silicon probe design (for the simultaneous measurement of neuronal activity).[262]

In summary, genetic manipulation of regional and subregional astrocyte genes, in combination with (*in vivo*) functional studies of astrocytes and their interactions with local neurons, will bring new insights into diversified astrocyte function and the consequences for control of local neuronal circuits and subsequent animal behavior. Such information may well provide novel insights into CNS diseases. It is likely studies of other CNS cell types, such as oligodendrocytes, microglia and pericytes will benefit from adopting similar strategies.
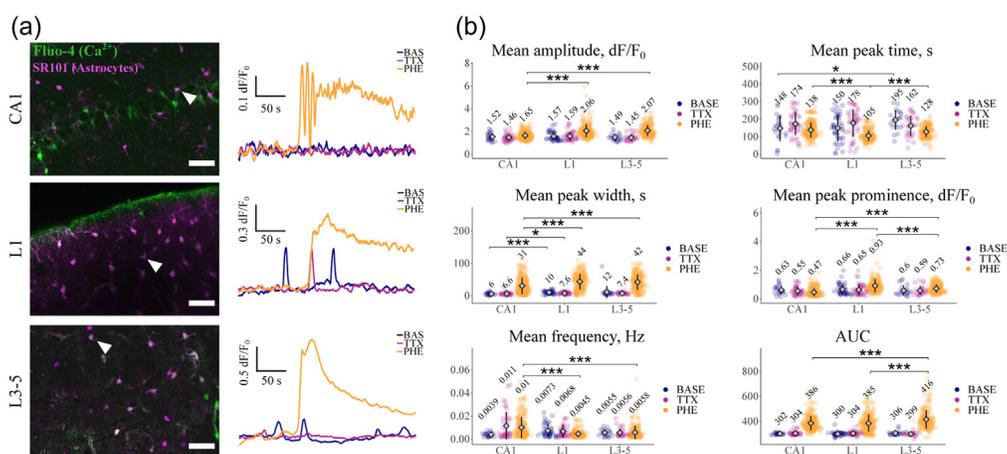
Fig. 14 Astrocyte subpopulations in the mouse CNS show significant differences in Ca^{2+} signaling. Ca^{2+} transients in sulforhodamine101 (SR101)-labeled astrocytes were detected using Fluo-4. Measurements were made in mouse acute tissue slices containing cortical layer 1 (L1), cortical layers 3-5 (L3-5) and the hippocampal CA1 region (CA1). Ca^{2+} transients (expressed as fluorescence changes relative to baseline: dF/F_0) were initially recorded under conditions of baseline activity (BASE) and after sequential application of tetrodotoxin (TTX) (to isolate astrocytes from neuronal activity) and tetrodotoxin plus the α_1-adrenergic receptor agonist phenylephrine (PHE). (a) Representative astrocytes (arrowheads) from three brain areas and the Ca^{2+} transients recorded from these cells under the various experimental conditions. Scale bar, 50 μm. (b) Analysis of various transient parameters, recorded under identical experimental conditions. Numerical values are the calculated means for each condition. AUC: area under curve. Modified from Batiuk et al.[254] *$p \leq 0.05$, **$p \leq 0.01$, ***$p \leq 0.001$.

3.8 *Probes for Oxygen Measurements by Phosphorescence Quenching*

Tissue oxygen levels can be measured by the phosphorescence quenching method[263,264] using molecular probes with controllable quenching parameters and defined bio-distributions. This approach relies on the ability of oxygen (O_2) to quench emission originating from the triplet excited states of probe molecules. Oxygen levels are derived from phosphorescence decay times, which are independent of the optical properties of the medium and local probe concentrations. "Protected" oxygen probes for truly quantitative imaging of oxygen *in vivo* consist of platinum (Pt) or palladium (Pd) porphyrins encapsulated inside hydrophobic dendrimers, coated at the periphery with hydrophilic polyethylene glycol (PEG) residues.[265–267]

Over the past decade, a special subset of phosphorescent probes has been developed specifically for 2P phosphorescence lifetime microscopy (2P PLIM or simply 2PLM) of oxygen.[124] The 2PLM technique has become particularly popular in neuroimaging, enabling imaging of oxygen distributions and concentration gradients in live brain with micron-scale resolution.[268–274] While being excellent linear absorbers, Pt and Pd porphyrins have vanishingly small 2P absorption cross-sections. In the original 2P oxygen probes (e.g., PtP-C343) the ability to absorb light by a 2P mechanism was boosted by supplementing the porphyrins with multiple 2P chromophores comprising 2P antennae.[124,275,276] However, later a more potent probe was developed, known as Oxyphor 2P[125] (Fig. 15), which relies on a single porphyrin whose 2P-active excited electronic states have been tuned by way of synthetic manipulations, rendering a chromophore with strong 2PA and exceptionally bright phosphorescence.[277,278] Presently, Oxyphor 2P is the probe of choice for 2PLM as well as for other applications of phosphorescence-based oximetry (e.g. Ref. 279).

The next challenge in the phosphorescent probes development area is to combine oxygen imaging with sensing of other environmental analytes (e.g. temperature, proton gradients, metal ions, etc.), explore higher orders of non-linearity (e.g. 3PA), and create sensors that can be tagged selectively to particular types of tissues and cells.
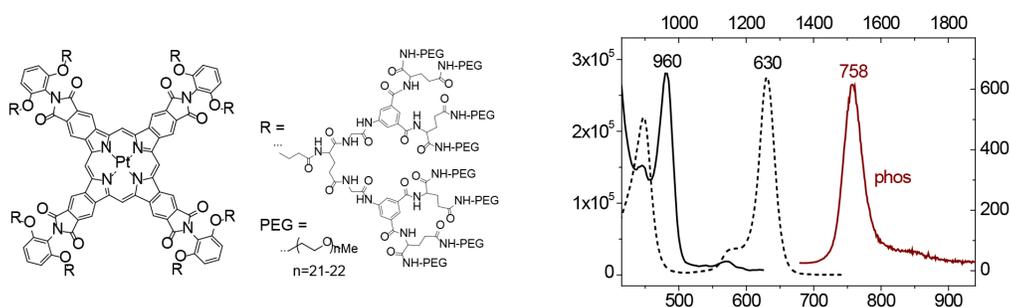
Fig. 15 Structure, optical absorption spectra and basic photophysical properties of probe Oxyphor 2P. In the spectra (right): dotted black line, 1P absorption; solid black lin, 2P absorption; solid dark red line, phosphorescence.

3.9 *Bioluminescent Tools for Imaging, Modulating, and Integrating*

Photons are typically generated from a physical light source, but they can also be produced by a genetically encoded luciferase, an enzyme that oxidizes a substrate, a luciferin, thereby emitting bioluminescence. Bioluminescent imaging enables minimal background and no photobleaching as there is no need for an excitation light source. Bioluminescence can be repurposed beyond imaging and be utilized as a versatile genetically encoded light source for controlling optogenetic actuators.

Core principles behind this platform technology are fusions of a light-emitting luciferase and a light-sensing photoreceptor such as opsins (channelrhodopsin, pumps),[280,281] enzymes (adenylate cyclase, Cre recombinase),[128,282] or transcription factors (CRY2/CIB, GAVPO).[128,283] Expressing light-emitting luciferases and light-sensing proteins in pre- and postsynaptic neurons permit causal interrogation of synaptically connected populations through an "optical synapse" [Fig. 16(a)]. Engineered split luciferases allow for functional reconstitution, allowing light emission to be harnessed to activate light sensing proteins when Ca^{2+}, voltage, neurotransmitters, and neuropeptides are detected or altered [Fig. 16(b)]. By making light itself activity dependent, optogenetic proteins can be modulated by luciferases serving as an integrator of biological processes [Fig. 16(c)].

Light emission from luciferases can be harnessed to control a range of biological processes by coupling bioluminescence with light-sensing proteins. Fusions of luciferase and opsin (luminopsins) have been used *in vivo* for improving motor deficits in a Parkinson's disease mouse model,[284] suppression of seizure activity,[285] enhancing neuronal repair and functional recovery after ischemic stroke[286] and spinal cord injury, modulating spatial and episodic short-term memory,[287] studying the effects of developmental hyperexcitation on behavior and circuit activity in adulthood[129] [Fig. 16(d)], and promoting axon regeneration after peripheral nerve injury.[288]

We can expect that this technology will benefit from discovery of new organisms with novel luciferase-luciferin combinations.[289] Molecular engineering of luciferases towards brighter and faster indicators in conjunction with tuning light sensing proteins will enable imaging, modulation, and integration of neuronal activity in freely moving mice at increasing sensitivities. This will further be enabled by chemical engineering of synthetic luciferins extending the color palette and intensity of emitted light and advances in miniscopes.[290] The trajectory of bioluminescent probes will allow imaging, controlling, and integrating neuronal activity with increasing sophistication.

3.10 *Optogenetic Actuators*

Optogenetic techniques have revolutionized neuroscience this past decade, offering an unprecedented toolkit for manipulating neuronal circuits with light.[130] Driven by the goal of understanding the organization and function of the brain, optogenetics began with the discovery of the light-gated cation-conducting channelrhodopsins ChR1 and ChR2[291,292] and the application of ChR2 for light-based excitation of mammalian neurons.[131,293,294] This groundbreaking advance was followed by efforts of multiple groups to enhance and diversify the optogenetic
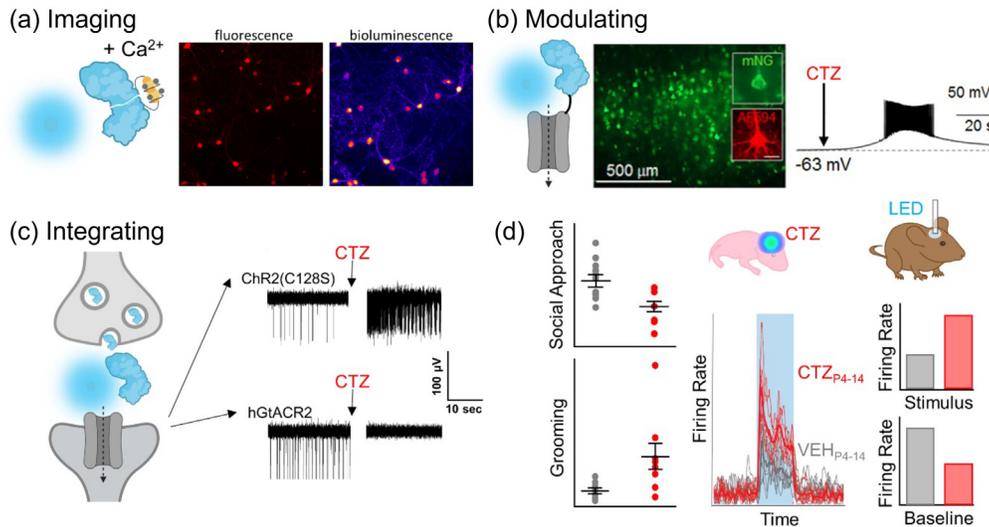
Fig. 16 Bioluminescent tools for imaging, modulating, and integrating. (a)–(c) Luciferases are genetically encoded light emitters that can be employed for imaging neuronal activity when used as a Ca^{2+} dependent split molecule (a), for modulating neuronal activity when tethered to an optogenetic element (b), and for integrating neuronal activity by expressing the light emitter pre- and the light biosensor post-synaptically (c). (d) Example of experiments taking advantage of the bimodal feature of luminopsins: genetically targeted brain circuits were activated chemogenetically (luciferin) during a defined time window of postnatal development; the same neurons were interrogated in adult animals optogenetically (LED).

toolbox.[295,296] These efforts have culminated in the engineering of dozens of novel optogenetic tools for activation and silencing of neuronal activity, for modulation of G-protein signaling pathways and for direct modulation of second-messenger pathways [Fig. 17(a)]. Optogenetic tools have also been developed for light-based control over gene expression, synaptic release, and biochemical signaling pathways. While these have been recently reviewed elsewhere,[297–301] we will focus here on the most commonly applied tools, which are based on microbial and vertebrate rhodopsin proteins. Common to all these novel tools is the utilization of naturally occurring light-sensitive proteins as actuators to drive cellular processes. The critical advance, and the main attraction of optogenetic tools for neuroscience research, is that these tools are all genetically encoded. This allows the use of genetic engineering techniques to direct the expression of optogenetic tools to precisely defined cell populations, through implementation of transgenic techniques and/or viral vector technology [Fig. 17(b)]. Selectivity is achieved via specific promoter or enhancer sequences that are exclusively expressed in the target cell populations. Cells expressing the light-sensitive protein respond to light in a manner defined by the properties of the specific protein used, while their non-expressing neighbors will remain unaltered. Together, the intersection of genetic specificity and the natural insensitivity of most brain tissue elements to light, render optogenetics a powerful technique for functional dissection of brain circuits in living animals. Optogenetics has been used for a wide range of experimental purposes, from functional dissection of neuronal circuit connectivity[302] through investigation of the contribution of defined neuronal populations to highly specific behaviors[303] to the development of light-driven interventions in animal models of neurological disorders[304] and, most recently, treatment of human patients suffering from neurodegenerative disease.[305]

Optogenetic techniques require optical access to cells expressing optogenetic actuators, to allow light-based modulation of the targeted cells. While this is simple to achieve *in vitro* (Boyden et al., 2005), applying optogenetic manipulations *in vivo* requires technology for delivering light to the living brain. The first experiments using ChR2 in behaving rodents used multimode optical fibers coupled through cannulas that were chronically implanted or affixed to the skull.[295,306] This arrangement allowed reversible connection of the optical fiber without the need to physically insert a light guide into brain tissue for each experiment. This simple technical approach has been the basis for numerous studies using 1P excitation [Fig. 17(c)] in a vast

Fig. 17 Optogenetic tools, genetic targeting and optical techniques. (a) Three major classes of rhodopsin-based optogenetic tools: excitatory pumps and channels (left); inhibitory opsins composed of chloride-conducting channelrhodopsins, proton and chloride pumps, and G-protein-coupled rhodopsins coupled to the inhibitory Gi/o pathway (center); enzyme-rhodopsins (right); shown are the histidine kinase group and the phosphodiesterase group. (b) Expression systems: two examples of gene delivery techniques used to express optogenetic tools in target neuron populations: crossing a recombinase driver mouse line with another that expresses a recombinase-dependent optogenetic actuator (left) or stereotactic injection of a viral vector encoding an optogenetic actuator. (c) Light-delivery techniques for optogenetics: (left) wide-field illumination of neurons expressing an optogenetic actuator through a chronically implanted multimode optical fiber or (right) 2P illumination of individual neurons using spiral-scanning of a diffraction limited spot or parallel illumination of extended shapes using wavefront shaping approaches. Images in panel (b) are from the Allen Institute for Brain Science (https://connectivity.brain-map.org/, experiments #741951571 and #288264301).

number of brain regions and neuronal circuits. However, one must consider that such manipulations are far from being able to accurately mimic the natural activity patterns expressed by populations of neurons in the unperturbed brain and might therefore lead to uninterpretable results due to "off-manifold" effects.[307]

In recent years, 2P techniques have been combined with highly refined optogenetic actuators to allow the control of single neurons[308–310] and precisely defined multi-neuron ensembles [Fig. 17(c)], see Sec. 6). Using pulsed near-infrared lasers combined with spiral scanning or parallel illumination approaches,[311,312] these developments have the potential to advance optogenetic techniques to the point that they can be utilized to "write in" information at the same level of spatial and temporal precision that the brain uses to encode information.[313–316] These exciting developments will surely yield important insight into the natural "language" that neurons use to communicate, encode the external world, and execute behavior. These are long-standing questions in neuroscience. The "optogenetic revolution" has brought us to the exciting place where we can begin to address these questions with remarkable detail and precision.

3.10.1 *Optogenetic tools: light-sensitive proteins*

Optogenetic tools are derived from a wide range of organisms, from archaea to fungi, algae, and animals. Genes encoding opsin proteins are widespread in nature, being found in all three domains of life and viruses.[317,318] Metagenomics led to a revolution in the field of opsin research in the early 2000s and now both metagenomic and metatranscriptomic techniques are driving the rapid expansion of our collective understanding of the taxonomic and functional diversity of this family of proteins.[319] While channelrhodopsins were the first to be applied as optogenetic tools,[131] the current optogenetic toolbox contains tools based on light-gated ion pumps, cation

and anion-conducting channels, G-protein coupled receptors and light-activated enzymes. The diversity of optogenetic tools allows for unprecedented flexibility in experimental design, but also demands an understanding of the basic working principles of the complexities and limitations associated with utilizing light-sensitive proteins.

3.10.2 *Light-activated ion pumps and channels*

The most widely used opsins in optogenetics are cation-conducting and anion-conducting channelrhodopsins, termed CCRs and ACRs respectively. In the early days, the cation conducting Channelrhodopsin-2 from the alga *Chlamydomonas reinhardtii* (CrChR2 or just ChR2) and its first mutant (ChR2-H134R, a mutation introduced to enhance the amplitude of functional photocurrents) monopolized optogenetic investigation.[292,320] ChR2 is a CCR, mostly permeable to protons but which also conducts other cations, including sodium but to a much lesser extent.[321] Naturally occurring ACRs, first discovered in 2015, conduct a variety of anion species.[322,323] Expressed exogenously in host cells, CCRs can act as photoactivatable depolarizing actuators while the function of ACRs is dependent on the chloride reversal potential. In many circumstances, the chloride concentration difference is such that ACR activation leads to hyperpolarization and neuronal inhibition. ACRs have been used extensively to silence adult mammalian neurons but they do have some limitations. Photoactivation of ACRs can lead to excitation in some cells (based on chloride reversal potential) and antidromic propagation when they are expressed in the axon.[324–326] In contrast to channelrhodopsins, ion pumping rhodopsins have the advantages of high ion specificity, active transport of ions against the electrochemical gradient, and a wide variety of functions. Inward proton pumps (e.g. NsXeR) can be used to depolarize neurons,[327] while outward proton (e.g. eArch3.0), outward sodium (e.g. eKR2), and inward chloride pumps (e.g. eNpHR3.0) hyperpolarize neurons and lead to inhibition.[328–331] Unfortunately, in contrast to the robust ion flux generated by some channelrhodopsins, pumps are limited by a one-to-one photon-to-ion stoichiometry which can translate into weak photocurrents or photodamage induced by prolonged and intense illumination in efforts to overcompensate for these limitations.[332] Additionally, excessive buildup of ions over time can damage cells, especially protons which can alter the intracellular or extracellular pH. These inconsistencies and limitations have motivated the community to attempt to identify new tools for neuronal inhibition. G-protein coupled receptors (GPCRs, discussed below) which engage G-protein signaling cascades or highly selective potassium channels (owing to the pronounced potassium gradient of neurons) would solve some of the issues with pumps and channels as hyperpolarizing actuators. While significant efforts to engineer a potassium channel from other channelrhodopsins enjoyed only partial success, naturally occurring potassium channels from *Hyphochytrium catenoides* were characterized recently and were termed Kalium Channel Rhodopsins (KCRs).[333] Even though KCRs still need to be tested and validated for *in vivo* experiments, this new discovery has long been awaited by the optogenetics community and these actuators are a welcome addition to the toolbox.

3.10.3 *Opsin engineering and enhancement*

Not long after the first optogenetics experiments were performed in the early 2000s, it became clear that the capabilities and diversity of opsins available to neuroscientists would need to increase substantially to match the scientific potential of the technique and overcome known and yet unforeseen roadblocks. In addition to the ongoing microbial ecological research to discover naturally occurring opsins, the engineering of opsins with desirable properties through targeted mutation and other means (such as fusions) became a fixture of the field. Efforts to engineer opsins with improved properties such as ion selectivity, spectral diversification, kinetics, light sensitivity, and ion conductance have seen success in recent years and have remained active areas of research. Spectral tuning is of particular interest, because red shifted light (i) penetrates more deeply into tissues, (ii) is less energetic than blue shifted light and thus causes less photodamage, and (iii) can be helpful to eliminate cross talk when opsins are paired with other tools such as fluorescent labels and voltage or Ca^{2+} indicators. A limited list of engineered opsins of interest include those developed for (1) altered ion selectivity: ChloCs,[334] (2) spectral properties: ReaChR[335] and Phobos,[336] (3) light sensitivity: ChRmine,[314] and

(4) kinetics: Chronos,[337] f-Chrimson.[338] The selection of optogenetic actuators for specific experimental applications should be guided by their ionic selectivity, kinetics, action spectrum, and photocurrent amplitude.

3.10.4 *G-protein coupled rhodopsins and light-activated enzymes*

Animal rhodopsins are GPCRs which catalyze GDP/GTP exchange through engagement of heterotrimeric G-proteins after light absorption.[317] The utility of GPCRs in optogenetics research has advanced significantly in recent years with the implementation of bistable melanopsins and parapinopsins. Human and mouse melanopsin variants (hOpn4L, mOpn4L) from retinal ganglion cells can be activated and inactivated with blue light and yellow light, respectively, an advantage in optogenetics experiments where temporal control of activity is desired.[339] While both opsins induce $G_{i/o}$ dependent inward rectifying K^+ (GIRK) currents and are highly light sensitive, mOpn4L exhibits superior on and off kinetics as well as less reduction in amplitude from sustained stimulation. However, these Opn4 variants both showed mixed activation of multiple G-protein pathways, leading to complex effects on neuronal physiology.[339] Herlitze and colleagues later described Lamprey Parapinopsin (UVLamP or PPO) which has improved activation and deactivation kinetics compared to mOpn4L and reduced spectral overlap between the active and inactive states resulting in shorter light pulses required for full activation and deactivation.[340] More recently, two new bistable opsins were characterized which couple selectively to the inhibitory $G_{i/o}$ signaling pathways and allow for efficient optogenetic silencing at presynaptic terminals. The targeting-enhanced mosquito homolog of encephalopsin, termed eOPN3, as well as the lamprey parapinopsin (PPO) were both shown to inhibit synaptic vesicle release through $G_{i/o}$ coupling.[341,342] PPO allows switchable synaptic silencing, activated with blue-violet light, and deactivated with green light. eOPN3 exhibits a red-shifted action spectrum, high light sensitivity, and rapid activation. It returns to the inactive state spontaneously within minutes, making it an excellent inhibitory tool on the time scale from minutes to hours. Another notable member of the bistable GPCR-rhodopsin family, the zebrafish opsin Opn7b also couples to the $G_{i/o}$ pathway and is inactivated by light stimulation. Opn7b was applied as an "inverse optogenetic tool." (Ref. 343).

The modulation of secondary messengers for the interrogation of cyclic nucleotide mediated cellular processes and signaling pathways has far reaching implications in neuroscience and biological systems in general and is an area where the spatiotemporal control afforded by optogenetics can provide a valuable advantage over pharmacological techniques.[344] There are three classes of enzyme-rhodopsins that have so far been described in the literature: histidine kinase rhodopsin (HKR), rhodopsin guanylyl cyclase (Rh-GC), and rhodopsin phosphodiesterase (Rh-PDE).[345–347] While the use of enzymerhodopsins for *in vivo* optogenetics research is not yet a staple, there are promising advances in the use of photoactive enzymes from flavoproteins. For example, the system comprising photoactive adenylyl cyclase from *Beggiatoa* (bPAC) and a cAMP-gated K+ channel from *Spriochaeta thermophila* (SthK) has been successfully applied to inhibit diverse neuron types in mice and Zebrafish embryos.[348] More recently, a variant of bPAC was developed which exhibits lower dark activity (biPAC) and was then applied to investigate cAMP signaling in hypothalamic neurons and its impact on sexual behavior in mice.[349]

4 Imaging Brain Activity with One-Photon (1P) Excitation

Due to the rapidly expanding arsenal of fluorescent probes (discussed in Sec. 3), there is a growing need for technologies to enable fast and efficient imaging of these probes in brain tissue. The main advantage of 1P fluorescent methods is the efficiency of excitation quantified as the absorption cross-section: the probability of photon absorption by a fluorophore molecule. In comparison with multiphoton methods (Sec. 5), the probability of 1P absorption for virtually all of these probes is very high. Therefore, 1P excitation does not require pulsed lasers and can be achieved with relatively inexpensive diode-pumped solid-state laser (DPSS) lasers, LEDs, or even a filtered white light source such as a xenon or tungsten–halogen lamp.

With 1P excitation, one way to achieve fast, large-scale imaging is by using wide-field illumination of the entire brain surface and capturing the emitted fluorescent light with a camera.

This "mesoscale" imaging (Sec. 4.1) is fast, because no scanning is involved, but lacks sectioning along the z-axis and has limited spatial resolution in the XY-plane due to light scattering. Therefore, mesoscale imaging is well suited for studies of cortical activity that do not require resolving single cells or cortical layers. Cell-type specificity can be achieved by genetic targeting of fluorescent probes.

1P fluorescence imaging technology has been miniaturized to enable measurements in freely behaving animals.[350] These wearable "miniscopes" (Sec. 4.2) have been widely applied, in part due to a relatively simple, open-source, low-cost design.[351,352]

Laser scanning microscopy improves resolution at the price of imaging speed, because of the need to scan the excitation beam. Among different approaches, light-sheet microscopy[6] has been successfully applied for *in vivo* imaging of brain activity in various organisms from semitransparent zebra fish embryos[353] to mouse cortex[354,355] (Sec. 4.3).

Optical imaging of deeper brain regions usually requires removal of the overlaying tissue or insertion of bulky lenses. As a compromise between the invasiveness of the measurement and the information content, fiber photometry has been used in many studies for detection of the fluorescence signal without spatial resolution. A number of recording channels can be increased using hundreds of splayed microfibers, each following a path of least resistance through tissue.[356] More recently, a proof-of-principle demonstration of deep brain imaging has been achieved by scanning the excitation beam through an implanted multimodal optical fiber to form an image (Sec. 4.4). Stabilization of this minimally invasive technology will enable cellular and subcellular resolution beyond the penetration limit of multiphoton imaging (we discuss multiphoton imaging in Sec. 5).

4.1 *Wide-Field Calcium Imaging*

In vivo wide-field Ca^{2+} imaging in awake mice expressing GECIs (see Sec. 3.1) allows simultaneous imaging of many brain areas as mice perform complex behavioral tasks.[357] Sensory integration, perception, memory and learning are just several examples of the cognitive functions that can be studied using this approach.[358–362] In addition, mesoscale imaging can be used to characterize the organization of spontaneous cortical activity[363–366] and functional mapping of cortical areas[358,367] [Figs. 18(a)–18(b)].

Very much like a conventional epifluorescence microscope, a wide-field or mesoscale fluorescence imaging system consists of two major components: an excitation path delivering light to the brain surface and an emission path that projects an image of the light emitted by the fluorescent indicator onto a camera chip. The light source in most state-of-the art wide-field setups is either a DPSS laser or an LED matching the excitation peak of a fluorescent sensor. A corresponding emission filter in front of the camera blocks excitation light from reaching the camera. The camera is often the most expensive component in the imaging setup. Many imaging setups use sensitive and expensive sCMOS or EMCCD cameras, particularly when the fluorescence signal is weak due to sparse labelling or limited brightness of the sensor. Tandem lens systems, as initially described by Ratzlaff and Grinvald in 1991[368] are often used to collect and project the emitted light onto the camera chip.[369] Excitation light can enter in between the lens pair via a dichroic mirror. Alternatively, the brain surface can be illuminated obliquely via one or multiple lightguides positioned independently from the excitation path.[370]

The advantages of wide-field imaging are its large field of view (the entire dorsal cortical surface in the mouse) and the ability to image through the intact skull offering minimally invasive and stable conditions. In addition, a typical wide-field imaging setup is fairly inexpensive, appealing to many labs worldwide. The disadvantages are that 1P imaging is mainly sensitive to superficial cortical layers, and suffers from light scattering, particularly when imaging through the skull. In addition, the raw fluorescence signal can be contaminated by hemoglobin absorption. While many of commonly used fluorescent sensors for wide-field imaging are green (e.g., GCaMPs), hemoglobin strongly absorbs light in the blue-green spectrum. This leads to hemodynamic artifacts due to the hemodynamic response (an increase in the blood volume and decrease in blood oxygenation) associated with an increase in neuronal activity. Several methods have been developed to correct for this artifact. These methods require illumination with additional wavelengths, thereby adding further components along excitation and emission paths.
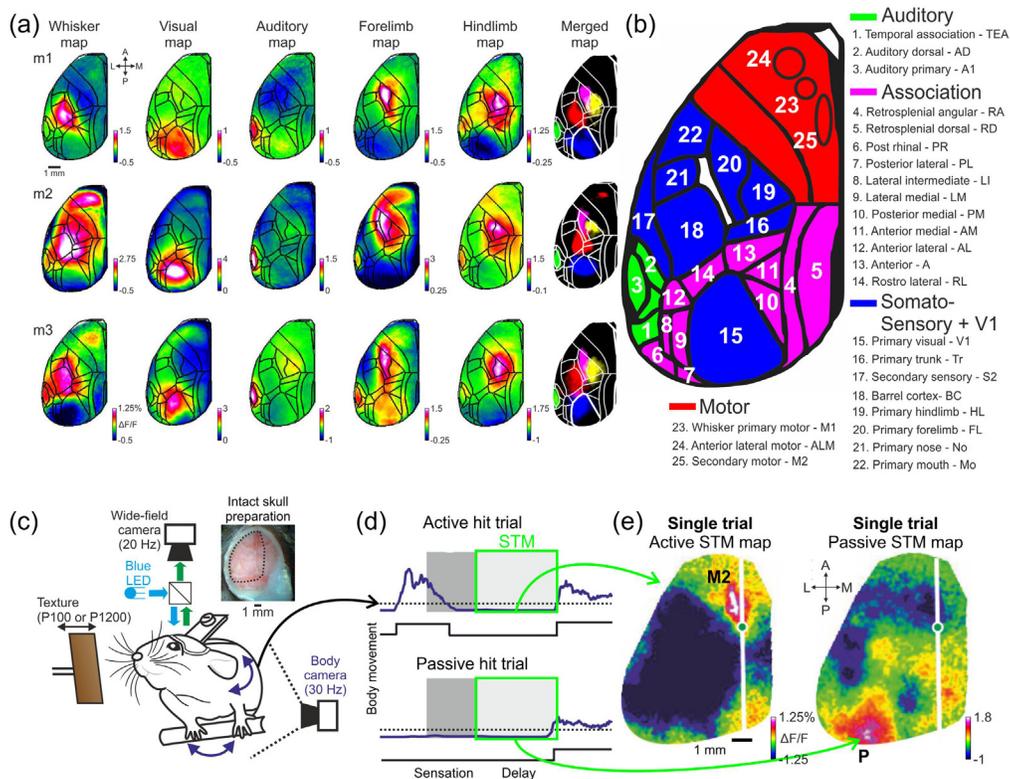
Fig. 18 Mapping of brain areas and task-induced neuronal activity with mesoscale Ca^{2+} imaging. (a) Functional mapping of cortical areas. Example maps from three mice (m1, m2, m3) under anesthesia in response to different sensory stimuli: whisker, visual, auditory, forelimb, and hindlimb. Mean evoked activity map is shown for each stimulus type for each mouse. Color denotes normalized fluorescence ($\Delta F/F$). The maps are registered onto the brain atlas (black lines; © 2004 Allen Institute for Brain Science. Allen Mouse Brain Atlas. Available from: http://mouse.brain-map .org/). Overlays of the 5 maps are shown on the right. (b) Parcellation of the dorsal cortical surface into 25 areas. Cortices are color-coded: auditory (green), association (pink), somatosensory + V1 (blue), and motor (red). (c) Behavioral and wide-field imaging setup in mice performing a whisker-dependent memory guided task. (d) Body movement vector in two example hit trials, one active and one passive. (e) Short term memory (STM) maps (averaged during the quiet delay period) for an active and passive trial showing frontal and posterior patches of activity, respectively. Color denotes normalized fluorescence ($\Delta F/F$).

One method uses estimated changes in concentration of oxy- and deoxyhemoglobin, derived from reflectance measurements at, e.g., 530 and 630 nm.[363] Specifically for GCaMP imaging, one can use Ca^{2+}-independent GCaMP fluorescence upon excitation at ~405 nm.[371] Due to the significant decrease in hemoglobin absorption at red wavelengths, hemodynamic artifacts are less prominent with red-shifted indicators, such as jRGECO1a, leading to relaxed requirement for hemodynamic correction of the collected fluorescence signals.[117]

An example of the insights gained from wide-field imaging is shown in Figs. 18(c)–18(e) adapted from Ref. 359. This study demonstrated that short-term memory was maintained in distinct cortical locations depending on the behavioral strategy of the mouse, either in a frontal area during an active strategy or a posterior area during a passive strategy.

Presently, wide-field imaging is being extended to specific neuronal populations via cell-type-specific targeting of GECIs.[164] Further development of red-shifted GECIs and other types of indicators, such as voltage sensors, may enable deeper and faster imaging. Combining wide-field imaging with fiber photometry and/or electrophysiological recordings will permit simultaneously imaging/recording of neuronal activity from both cortical and subcortical areas. Finally, 1P fluorescence imaging is being implemented in freely moving mice (Sec. 4.2), opening the door to study more natural behaviors.

4.2 *Wearable 1P Microscopes*

Table-top microscopy systems, such as the one shown in Fig. 18 above, require head fixation of the animal under the microscope objective. This condition is incompatible with many behaviors. Wearable imaging systems have been developed to enable measurements in freely moving model organisms, from rodents to zebra finches and primates.[352,372,373] These miniaturized microscopes (or "miniscopes") exist in several implementations regarding imaging capabilities, size, and weight depending on experimental needs. Many of them are currently tethered (i.e., connect to the data acquisition system through flexible wires and, in some cases, fibers), allowing measurements during behavioral assays commonly used in research settings. Most of them rely on fluorescent indicators to provide the specificity and contrast necessary to study the cellular or molecular signaling of interest.

1P miniscopes typically employ integrated LEDs or fiber-coupled DPSS lasers for fluorescence excitation and CMOS (complementary metal oxide semiconductor) image sensors for detection [Fig. 19(a)].[352,372,373] They offer high frame rates (up to ~60 Hz at full resolution) across large fields of view (from ~0.6 mm up to 10 mm diameter). Spatial resolution varies with the field of view from few microns to tens of microns.[375,376] One of the main drawbacks of 1P miniscopes is their potential out-of-focus signal contamination and limited optical depth penetration in densely labeled tissue (≤ 150 μm depending on tissue type). Deeper regions can be imaged using tissue-implanted relay optics, such as gradient index (GRIN) lenses [Figs. 19(b)–19(c)]. The relatively low equipment cost and ease of use of 1P miniscopes have facilitated their widespread adoption.

Wearable imaging systems have enabled biological studies difficult or unfeasible with their larger stationary counterparts (e.g., social interactions, sleep-wake transitions, seizure activity).[374,376] They have provided insight into how genetically defined cell types encode external (e.g., sensory and motor) and internal (e.g., cortical state) information in various brain regions. More recently, miniscopes have also enabled real-time measurement of cellular activity in the spinal cord of behaving mice.[372,377–379]

In the future, we can expect these imaging systems to become even more powerful. Improved electronics and optics (e.g., new CMOS sensors, custom micro-optics, electronic focusing systems) will enhance 1P miniscopes' ability to record at higher resolution, sensitivity, contrast, and speed, in multiple colors and across larger FOVs or tissue volumes.[352,372,378–380] While initial tether-free designs exist [Fig. 19(a)], further improvements in onboard or wireless power and data transmission technology are needed to reduce overall device weight and boost recording duration at desired image resolutions and frame rates.

Complementary to these hardware improvements, new indicators (e.g., transmitter and voltage sensors) and computational tools [Fig. 19(b)] (see also Sec. 9) are likely to enable real-time
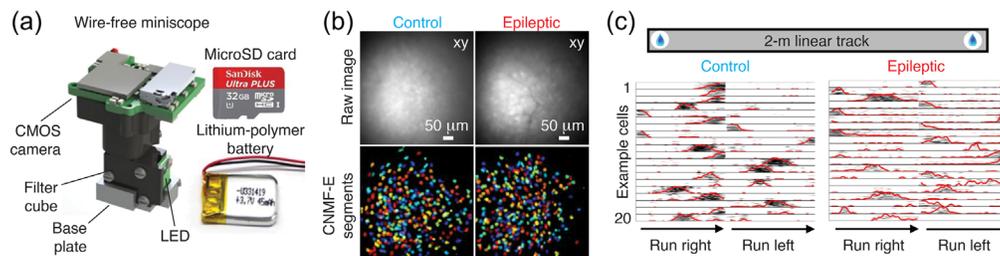
Fig. 19 1P wearable microscopes for cellular-resolution imaging in freely behaving animals. (a) Example 1P miniscope for high-speed, cellular-resolution imaging in freely behaving mice. This implementation is wire-free and weighs 4-5 grams, including a 1.1-gram single-cell lithium-polymer battery. It allows recordings of ≥ 30 min duration at 20 Hz, 320 x 320 pixels resolution, x2 pixel subsampling across a 550 μm $\times$ 550 μm FOV. Data is logged onto a MicroSD card for offline analysis. (b) Example raw images of GCaMP6f Ca^{2+} indicator-expressing (top) and computationally identified cells (bottom) in the dorsal hippocampus of control and epileptic mice. Imaging was performed using a tissue-implanted GRIN lens. (c) Spatially tuned activity pattern across 20 example cells from control and epileptic mice trained to run on a 2-m linear track for water reward. Adapted from Ref. 374 with permission from Nature Publishing Group.

analyses and interrogation of nervous system activity. These innovations will permit longitudinal investigation of various disease, treatment, or behavioral conditions best studied in freely moving animals.

4.3 *Imaging in 3D with Light-Sheet Microscopy*

The standard method of forming 3D images in intact, living specimens such as the brain is to scan a high numerical aperture (NA) point of light to different positions within a volume of interest. For instance, sequential raster scan of individual planes is often used in confocal microscopy to reconstruct a volume. However, this approach becomes increasingly challenging for high-speed imaging, both because scanners begin to exceed physical limits, and integration time per pixel becomes vanishingly small, nearing the fluorescence lifetime of many fluorophores.[381] To overcome these limitations, it is possible to acquire data using parallel illumination of multiple regions at once. In multiphoton microscopy (Sec. 5), this approach has taken many forms, from multi-point scanning[382,383] to extended axial range imaging.[384–386] An embodiment of this approach using 1P excitation is light-sheet microscopy, which illuminates an entire plane within the sample, achieving optical sectioning by generating a focused image of this illuminated plane onto a camera detector. This approach greatly increases integration time per pixel compared to point scanning, while its selective illumination of only the plane being imaged makes light-sheet microscopy especially light-efficient.[381]

Light-sheet microscopy has traditionally been applied to imaging cleared tissues (Sec. 2.2), where generating a thin light sheet and focusing onto this light sheet with a second, orthogonal objective is relatively simple for samples up to the size of a whole mouse brain.[387,388] Another application has been to image small organisms such as Drosophila embryos and zebrafish during early development, and also for functional imaging in the larval zebrafish brain and heart.[389,390] However, the standard use of two orthogonal objective lenses in these light-sheet systems limits both sample size and geometry. 3D imaging speed is also limited by the need to either translate the sample through the light-sheet plane or scan the light sheet in synchrony with repositioning of the detection focal plane. An approach that overcomes these speed and geometry constraints is swept confocally aligned planar excitation (SCAPE) microscopy, a single-objective light-sheet approach, which uses a confocal de-scanning to enable an obliquely incident light sheet at the sample to be scanned from side to side, while the image of the oblique plane is de-scanned, rotated and mapped onto the face of a fast camera [Fig. 20(a)].[354,355] The system's single, stationary objective permits a wide range of intact samples to be imaged in an upright or inverted geometry and does not require restraint or physical translation of the sample. This approach permits 3D microscopy of a wide range of living organisms at speed of up to 300 volumes per second, leveraging the low phototoxicity associated with light-sheet excitation and high light efficiency to capture Ca^{2+} dynamics as well as 3D movement in behaving animals.

SCAPE microscopy has been applied to high-speed imaging of a range of different samples including proprioceptive neurons in crawling Drosophila larvae,[391] whole-brain Ca^{2+} imaging in adult Drosophila,[392] zebrafish larvae [Fig. 20(b)],[381] Ca^{2+} and red blood cell dynamics in the beating hearts of zebrafish larvae,[355,393] and neuronal activity in freely moving C. elegans worms.[355] SCAPE is also effective for imaging the mouse nervous system, capturing activity in apical dendrites in layers 1–3 of the awake mouse cortex at 10 volumes per second [Fig. 20(c)],[7,354,381,394] and profiling Ca^{2+} response properties of 10,000's of olfactory sensory neurons in the intact mouse olfactory epithelium.[395] All the prior examples utilized 1P excitation at 488 and 561 nm illumination. However, SCAPE and related light-sheet approaches are also suitable for 2P excitation which can enable deeper imaging into the living mammalian brain. In the future, 2P SCAPE will provide a competitive alternative to multiplexed 2P strategies outlined in Sec. 5. Efforts are also underway to implement SCAPE via an implanted GRIN lens enabling imaging of deep brain regions.

4.4 *Deep Imaging Through Multimode Optical Fibers*

GRIN lenses, prisms and fiber bundles have been successfully used to image deeper brain regions.[396–401] However, insertion of these optical elements into the brain is invasive. One
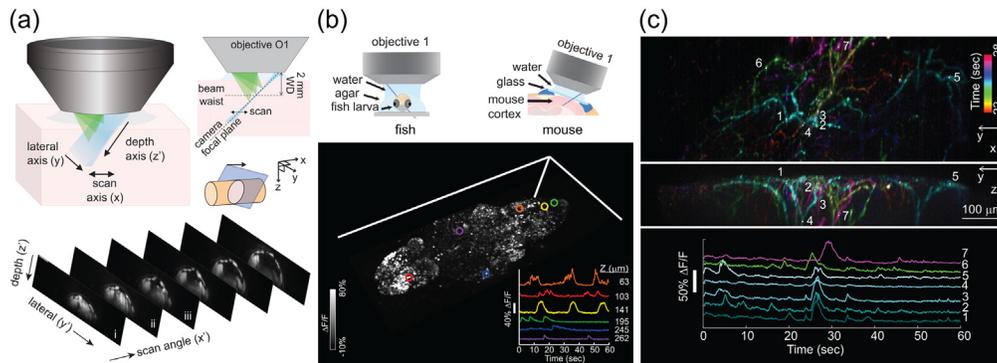
Fig. 20 SCAPE microscopy: elements and application. (a) Top: SCAPE microscopy uses an oblique light sheet to illuminate the sample, and emitted light is collected by the same objective lens. SCAPE sweeps the oblique light sheet back and forth across the sample, de-scanning and rotating returning light to focus onto a stationary camera. Bottom: example images of a drosophila larva, captured as the light sheet scans. (b) Top: experimental imaging configurations to image neuronal activity in zebrafish larvae and awake, behaving mouse. Bottom: visualization of spontaneous neuronal GCaMP activity in the whole brain of a larval zebrafish. Volume rendering shows a maximum intensity projection over time with inset showing time-courses of 6 cells at 6 different depths in the brain. (c) Top and middle: spontaneous activity of apical dendrites of layer 5 neurons in whisker barrel cortex via GCaMP6f imaging in awake behaving mouse. Maximum intensity projection from the top (XY) and side (YZ) with colors denoting time of peak activity. Bottom: time-courses for the seven numbered regions of interest indicated above.

strategy to minimize this problem is imaging though hair-thin multimode fibers (MMFs). Light transport through MMFs is a complex, hardly predictable, yet deterministic process. It can be described by the transmission matrix (TM),[402] a linear operator whose components can be experimentally measured by means of wavefront manipulation and interferometry.[403] For this application, the TM can be conceptually thought of as a lookup table between the light "shape" entering and exiting the fiber.

Once available, the TM prescribes an optical field entering the MMF required to form the desired field distribution at the focal plane [Fig. 21(a)]. When applied to deep-tissue fluorescence imaging, the fiber is being advanced through the overlying tissue until it arrives at a subcortical brain region under investigation [Fig. 20(b)], which is then sequentially exposed to a series of illumination fields. These fields most commonly form diffraction-limited spots sequentially displayed across the focal plane, mimicking a laser scanning microscope. The emitted fluorescence is collected through the same fiber, spectrally separated, and recorded by a photodetector such as a photomultiplier tube (PMT) [Fig. 20(c)].

In context of neuroscience, holographic endoscopy has been used for structural imaging of neurons in cultures,[405] acute brain slices[404,406] and *in vivo*[403–405] [Fig. 20(d)]. Among all other endoscopes, imaging with MMFs features the smallest probe footprint inducing tissue damage while maintaining subcellular resolution [Fig. 20(e), Ref. 404]. Even dendritic spines and axonal boutons can be resolved using MMFs with diameters ~100 μm [Fig. 20(f), Ref. 404]. The first indication that spatially-resolved functional imaging of intracellular Ca^{2+} is possible to implement through the means of holographic endoscopy has been shown recently [Fig. 20(g), Ref. 405].

Using fibers with higher numerical apertures, imaging of custom-designed regions of interests and optimizing the animal models for indicator sparsity required in 1P imaging should ultimately open the door for minimally invasive imaging of neuronal activity anywhere in the brain. Moreover, high speed scanning of custom-designed trajectories along blood vessels containing a fluorescent indicator would allow imaging of blood flow similarly to a 2P technique pioneered by David Kleinfeld and collaborators.[407] Importantly, the same probe could be used not only for imaging but also for spatially resolved optical stimulation of opsins (i.e., optogenetics).

All these imaging modalities funneled through a hair-thin optical probe would push the microscopic visual reach beyond the fundamental limits of optical far-field imaging technologies. The main challenge lies currently in transitioning this technology into awake animals and the realm of chronic experiments.
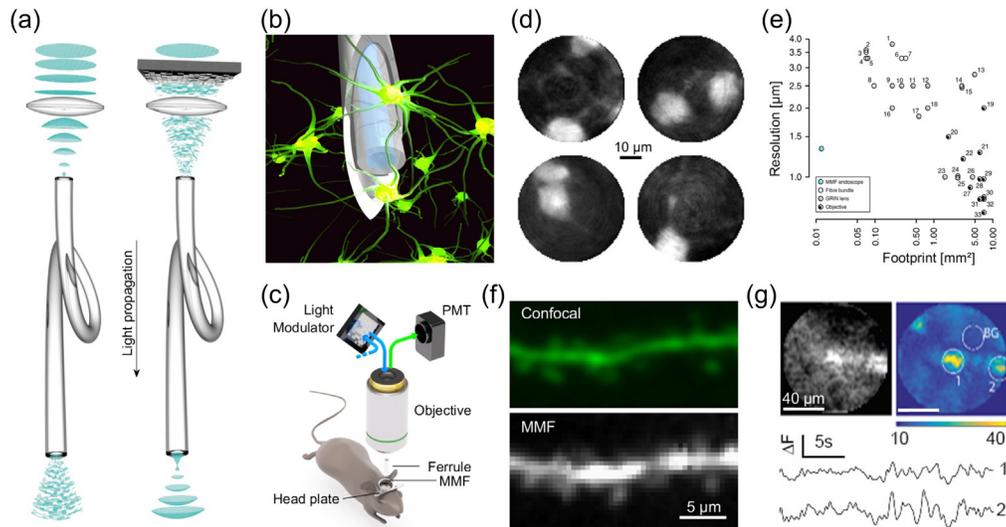
Fig. 21 Deep brain imaging through an optical fiber. (a) Coherent light propagated through a MMF forms a speckle pattern at the output (left). Manipulation of the wavefront entering the MMF yields a desired optical field, e.g., a focal spot (right). (b)–(c) Experimental configuration for *in vivo* imaging. (d) Inhibitory neurons expressing tdTomato imaged *in vivo* (panel adapted from Ref. 403). (e) The trade-off between the fiber size and resolution. (f) Dendritic spines of a hippocampal neuron *ex vivo* resolved using a MMF (bottom). Comparison of the same field of view imaged with a confocal microscope (top). Panels (e) and (f) are adapted from Ref. 404. (g) *In vivo* neurons expressing GCaMP6f (left) and their activity visualized as standard deviation over time (right). Bottom traces show the change of signal in time after background (BG) subtraction from two regions of interest (1 and 2). Panel adapted from Ref. 405 © Optica.

5 Imaging Brain Activity with Multiphoton Excitation

There are a few fundamental challenges when imaging brain activity. One challenge already discussed above (Sec. 4) is to be able to capture fast signaling events (1–100 ms) flowing rapidly between neurons. This challenge scales with the size of neuronal network under investigation. Another challenge is that brain tissue is often highly scattering, which limits the depth penetration of 1P microscopy methods. For example, in the mouse cortex, 1P voltage imaging can be used to measure spikes in cortical neurons with cell bodies located in layers I and II, i.e., less than $\sim$200 μm below the surface.[99,201] Deeper penetration requires multiphoton imaging.

Here, we introduce a suite of multiphoton technologies that have been developed and/or significantly advanced in the last decade to penetrate deep into scattering tissue and cover a large field of view while retaining high resolution and speed. We start by highlighting a multi-region 2P microscopy design that has been developed to improve the imaging field of view (Sec. 5.1).[408–410] These microscopes rely on very large objectives with high NA. The problem of multiregion imaging has also been addressed by optical systems with multiple arms and/ or objectives.[411–413]

Next, we provide a brief overview of several strategies to increase the imaging speed through temporal and spatial multiplexing and "light sculpting," i.e., engineering of the point spread function (PSF, a.k.a. the focal spot) (Sec. 5.2). This is followed by a more detailed discussion of two fast imaging strategies: discrete sampling of specific voxels of interest with acousto-optic lenses[414] (Sec. 5.3) and multipass temporal multiplexing where the excitation laser pulses sequentially excite fluorescence in axially displaced voxels (Sec. 5.4).[415]

In 2P microscopy, excitation of fluorophore molecules by scattered photons results in the background signal leading to deterioration of signal to background ratio (SBR) with depth. This background can be reduced using two photons of different color derived from two laser beams that overlap only in the focal plane (Sec. 5.5). In 3P microscopy[416] (Sec. 5.6), the probability of simultaneous absorption of 3 photons outside of the focal volume is very low, allowing deeper penetration. In addition, 3P excitation requires less energetic, red-shifted photons that scatter less in tissue.

The ability of multiphoton technologies to image the brain tissue deeper, clearer, and faster makes these tools well compatible with the "circuits-to-behavior" neuroscience studies. Ideally, these studies would be conducted in freely behaving animals. To this end, several miniaturized, portable multiphoton designs have been explored (Sec. 5.7).[417,418] The major limitation for these miniaturization efforts is the fundamental tradeoff between the objective diameter, resolution, and field of view. To overcome this limitation, alternative strategies are being explored including microlens arrays[419,420] and nanofabricated metalenses.[421] In the meantime, however, performance of tabletop multiphoton microscopes remains unsurpassed.

5.1 Multi-Region 2-Photon (2P) Imaging

Many conventional 2P imaging systems have fields-of-view (FOVs) that are limited to 1 mm^2 or less, and typically a single image plane is monitored per acquisition. However, neuronal circuitry can be distributed across many cubic millimeters, and capturing dynamics at this spatial scale, with a sub-second time resolution, can lead to novel insights into brain function. Thus, it is useful to pursue large-scale 2P imaging.

Measuring neuronal activity across large FOVs ($\sim$10 mm^2 or more) with subcellular resolution requires relatively large diameter optics, such as microscope objectives that are $>$50 mm wide.[408,422,423] Objectives with moderate-to-high numerical apertures ($>$0.45 NA) and large FOVs (i.e., long focal lengths) provide access to an order of magnitude more pixels. However, the sampling time of the raster scan is unchanged, so scanning the full FOV results in frame rates that are too slow ($>$1 s per frame) to be useful for many applications. To this end, strategically choosing specific subregions within the large FOV and fast jumping between these subregions[408,410,422] can be used to sample across large FOVs while still maintaining sub-second temporal resolution. This technique can be combined with temporal multiplexing[422,424] and spatial multiplexing[409] to achieve fast, simultaneous acquisition of multiple volumes (Fig. 22). An alternative approach to imaging in multiple regions simultaneously is to have multiple, small ROIs under separate, independently positioned objectives.[411,412]

Multiphoton imaging has been scaled up in the axial dimension as well. For example, one can temporally multiplex 2P imaging and 3P imaging (Sec. 5.6) to simultaneously image superficial and deeper neocortical layers.[425] Many innovations in conventional 2P imaging have found
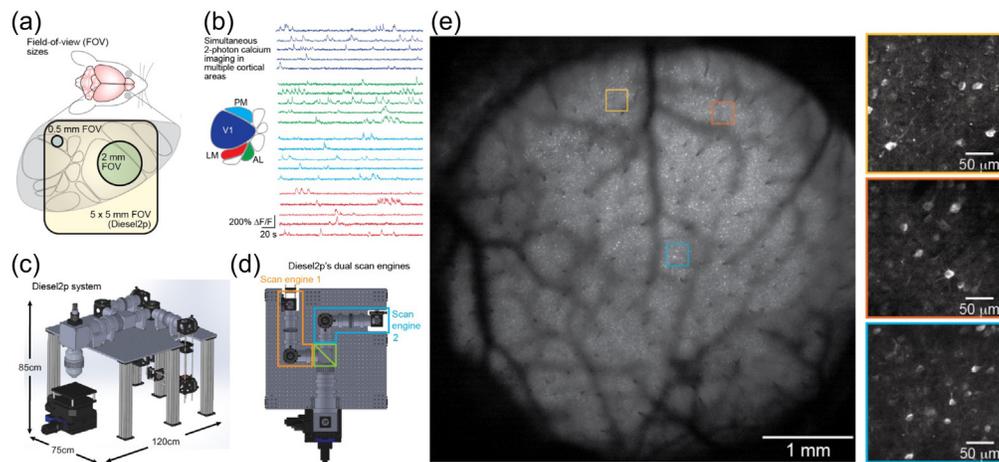
Fig. 22 Large field-of-view, multiregion 2P imaging. (a) FOV available in conventional 2P systems are often confined to $\sim$0.5 mm, which is smaller than many cortical areas. Larger FOVs (2-mm diameter, or the 5 x 5 mm region of the Diesel2p system[410] provide optical access to multiple cortical areas simultaneously. (b) Neuronal activity can be monitored across these FOVs through rapid beam steering and/or multiplexed beams. (c)–(d) The Diesel2p is a system that provides a large FOV (c) and dual scan engines coupled into a single objective (d) for independent multiplexed imaging and/or 2P optogenetic manipulations of neuronal activity. (e) With large FOV, 2P imaging systems, subcellular resolution is available across a large imaging volume, containing on the order of a million neurons. Adapted from Ref. 410.

application in multi-region 2P systems as well, including adaptive optics[410] (Sec. 5.8), axially extended Bessel beam volume scanning[426] (Sec. 5.2), and quad-region scanning.[427]

5.2 *Sampling Strategies for Fast 2P Imaging*

Conventional 2P microscopy is based on raster scanning of a near-infrared laser beam focused into a "point" (diffraction-limited) PSF. However, as previously described, sequential scanning of this PSF throughout large (mm^3) volumes is too slow to image neuronal activity, which occurs on the timescale of milliseconds. Figure 23 summarizes various approaches for fast 2P imaging with large FOVs that have been proposed in recent years. Among them is the multi-region
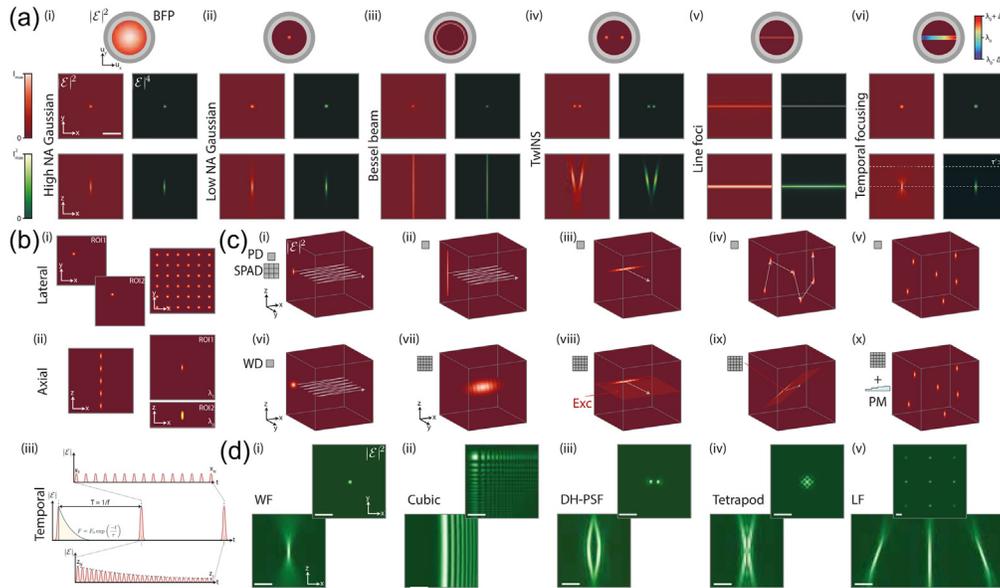
Fig. 23 A summary of state-of-the-art approaches for fast 2P imaging. (a) Commonly used excitation modalities: (i) high NA gaussian beams,[428] (ii) low NA gaussian beams,[429] (iii) Bessel beams,[430] (iv) stereoscopic low NA gaussian beams,[386] (v) line foci for tomographic imaging[182] and (vi) temporally focused, low NA Gaussian beams.[311,431] Top row: simulated intensities of incident beams in the objective back focal plane (BFP) used to generate different excitation PSFs. Middle row: simulated excitation PSFs (red colormap) and the proportional 2P excited fluorescence (green colormap) generated in the focal plane (XY). Bottom row: same as middle but axial (xz) slices. The color bars and principal axes in (i) are applicable to all simulated data apart from (vi) where different colors are used to represent the different wavelengths constituting the ultrafast pulse with central wavelength λ_0 used for temporal focusing. τ refers to the pulse duration which is shortest at the focal plane where 2P excitation is maximized. Abbreviations: |E| refers to the amplitude of the electric field; $|E|^2$, the intensity, and $|E|^4$, the proportional 2P fluorescence; NA, numerical aperture; TwINS, 2P imaging of neurons using stereoscopy. (b) A summary of different implementations of (i) lateral, (ii) axial, and (iii) temporal multiplexing that have been applied to fast 2P imaging. (i) Left: the incident beam is divided into two beamlets each directed to simultaneously image different regions of interest (ROI).[432] Right: the excitation field is divided into multiple laterally separated spots which sample different portions of the same field of view.[433] (ii) Multiple planes throughout a volume can be imaged simultaneously using axially multiplexed beams[432] or by directing beamlets with different wavelengths to different sample depths.[424] (iii) Since the lifetime of common fluorophores is shorter (shown, not to scale) than the separation between subsequent pulses generated by suitable mode-locked lasers, each pulse can be divided into multiple beamlets, which can be laterally (upper) or axially (lower) displaced to perform fast 2P imaging.[415,434,435] (c) Sequential and parallel acquisition modes used for fast 2P imaging. (i)–(v) Methods based on single pixel detection: (i),[428] (ii),[430] (iii),[182] (iv),[436] and (v).[437] (xii)–(x) Common parallel excitation methods combined with camera detection: (vii),[438,439] (viii),[429] and (ix).[440] Abbreviations: PD, point detector; SPAD, single-photon avalanche diode array. (d) (i) Simulated widefield PSF and detection PSFs used for extended depth of field imaging: (ii),[441] (iii),[383] (iv),[442] and (v).[443] Abbreviations: PM, phase mask; WF, widefield; DH, double helix PSF; LF, light field.

microscopy discussed in Sec. 5.1. Another (not mutually exclusive) approach is "sculpting" the PSF in space and time in order to increase the imaging speed (or to image larger volumes whilst maintaining acquisition rates).

Diverse photonic technologies[354,444–452] have increased the rate of sequential scanning, and volumetric imaging rates have also been increased by converting lateral scanning of a patterned substrate in space into axial displacements.[453,454] Some techniques aim to reduce the pixel dwell time of 2P microscopy to its fundamental limit (determined by the excited state fluorophore lifetime) by dividing high-energy ultrafast laser pulses into beamlets that sequentially excite fluorescence in different voxels.[415,424,434,435] The temporal resolution of 2P microscopy has also been improved by optimizing the scan trajectory[450] or by discretely sampling voxels distributed throughout the region of interest.[100,436,455]

An alternative approach for fast 2P imaging is to sculpt the excitation PSF and increase the instantaneous volume of excitation to reduce the total number of sequential measurements. This includes line scanning,[182] and axially elongated excitation PSFs such as Bessel beams which are scanned in the directions orthogonal to their elongation.[426,430,456,457] The acquisition of stereoscopic (tomographic) information is necessary in the case of elongated foci and densely labelled samples.[182,386] Illumination with spatial and temporal focusing of femtosecond pulses has also been used to increase frame rates.[431,438,439] Another subclass of parallel methods spatially multiplex the excitation beam, project multiple foci in 3D, and record fluorescence using 1D[425,432,437,449] or 2D detectors.[383,433,441,458–460]

5.3 Two-Photon Imaging in 3D with an Acousto-Optic Lens

For many applications, such as imaging Ca^{2+} transients in neuronal cell bodies, specific dendrites, axons, or synapses, the ideal sampling strategy would not be a complete coverage of a volume, but rather a set of regions of interest (ROIs) strategically positioned to overlap with locations of interest. This can be achieved by using random-access 3D imaging with an acousto-optic lens (3D-AOL) to steer a 2P laser beam to arbitrary preselected locations in the imaging volume.[461] Moreover, the same technology can be used to correct for brain movement in real time, which can be problematic for imaging of small structures during behavioral tasks.[462] Selective imaging of ROIs with 3D-AOL microscopy enables considerably higher temporal resolution than imaging the entire volume, since the inertia-free focus and scanning is rapid and the ROIs typically occupy a small fraction of the volume.[414,436,463] In addition, this type of acquisition streamlines curation, analysis, storage, and sharing, because only the required data are collected.

3D-AOL laser scanners consist of two orthogonally arranged pairs of AO deflectors, with counter-propagating acoustic waves that fill the TeO_2 crystals, creating dynamic diffraction patterns that can steer and focus a 2P laser beam in 10–25 μs[436,455,464] [Figs. 24(a), 24(b)]. Linear acoustic drives enable random access focusing of a laser beam to any point in the 3D imaging volume (called 3D-RAMP)[436] or random access focusing and continuous line scanning in different x–y planes,[455] while nonlinear drives enable continuous line scans in any arbitrary direction (x, y, z) at tens of kilohertz.[467] Unlike resonant galvanometers, 3D-AOL line scans can be varied in orientation, length, and dwell time ($\sim 10^7$–10^5 s/pixel). A compact design version of the 3D-AOL has a $10 \times 10 \times 25$ cm footprint and can be introduced into the optical path of conventional 2P microscopes providing an imaging volume of $400 \times 400 \times 400$ μm^3.[414] Real-time correction for brain movement is achieved by tracking a fluorescent object in the imaging volume [typically a bead; Fig. 24(c)] with closed-loop FPGA-based image processing and compensating for the movement with a rigid translation of the imaging volume using the 3D-AOL scanner with update rates up to 1 kHz.[462]

3D-AOL microscopy has been used with GECIs to image neuronal population activity in the forebrain of tethered zebrafish while performing swim bouts,[462] and populations of excitatory[463,468,469] and inhibitory neurons[465,470] in mice [Fig. 24(d)]. Its high spatial resolution has enabled imaging of large populations of axons in the cerebellum[471] and selective imaging of dendritic trees and spines with millisecond precision with either 3D-RAMP[436,463] or multiple line scans[466] [Fig. 24(e)]. It is particularly suitable for high-speed multiscale imaging of neurons and neuronal structures that are sparsely distributed within local circuits [Fig. 24(f)].
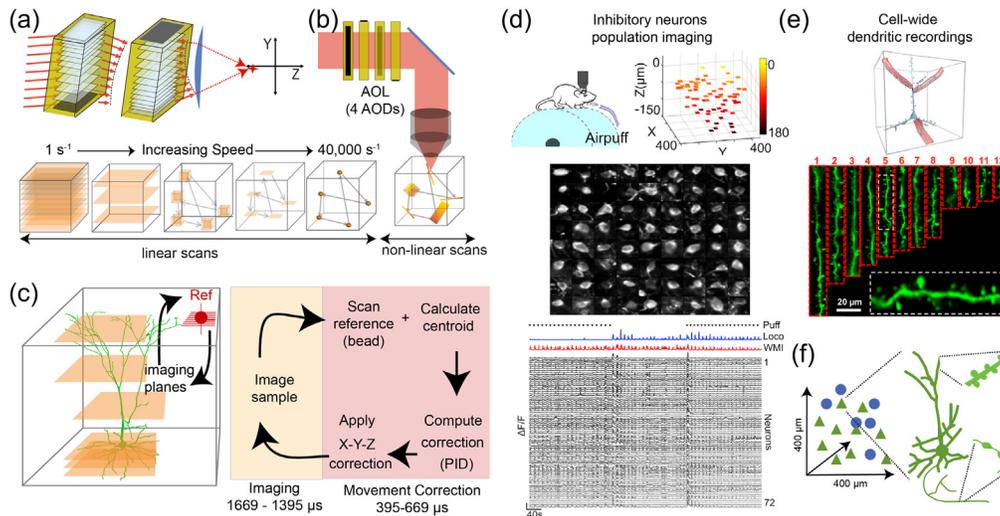
Fig. 24 Principles and applications of 3D-AOL microscopy. (a) Schematic of pair of AO deflectors (AODs) with chirped sound waves that curve the optical wavefront of a laser beam (red lines). Modified from Ref. 463. (b) Two pairs of orthogonally aligned AODs that make up a spherical AOL that can focus and scan a laser beam in 3D. Cubes below illustrates multiple linear (left) and nonlinear (right) drive-based imaging modes. Modified from Ref. 414. (c) Left: illustration of 3D movement correction with XY and Z scans of a bead interleaved with multiplane imaging. Right: sequence of operation to track a reference object in 3D and compensate imaging for brain movement. Modified from Ref. 462. (d) Selective imaging of sparsely distributed inhibitory interneurons in the cerebellum. Top left: awake mouse on a treadmill. Top right: locations of somatic ROIs in 3D-AOL imaging volume of mouse expressing GCaMP6f in Golgi cells. Middle: montage of 72 selectively imaged Golgi cell somata. Bottom: activity traces extracted from the cells during locomotion, whisking (WMI) and mild air puff to the whiskers (Puff). Modified from Ref. 465. (e) Image of pyramidal cell with dendritic branches selectively imaged with multiple line scans (Ribbon scanning). Aligned images of individual dendritic segments with spines clearly visible (middle). Modified from Ref. 466. (f) Schematic illustrating multiscale imaging functionality of 3D-AOL microscopy, which enables simultaneous imaging of neuronal populations, dendrites, spines and axons present in a local circuit.

Current developments include increasing the imaging volume and speeding up movement-stabilized imaging of entire dendritic trees. In the medium-term, this technology could be optimized for movement-stabilized voltage imaging[100] and photo-stimulation applications. On the longer-term, ultra-high-speed adaptive optics capability of this technology[467,472] could be useful for a range of applications, including higher spatiotemporal imaging of neuronal circuits, optical tweezers, and nanofabrication.

5.4 *Dense Volumetric Imaging with Light Beads Microscopy*

Another approach to address a trade-off between resolution, speed of acquisition and the volume size of the recorded neuronal population is Light Beads Microscopy (LBM)[415] that pushes multiphoton imaging to the limits dictated only by the tolerable biological radiation exposure and the nature of fluorescence. In LBM, a set of axially separated and temporally distinct foci record the entire axial imaging range near-simultaneously, enabling volumetric recording at 1.41×10^8 voxels per second only limited by fluorescence lifetime (Fig. 25). Combined with an acquisition strategy that allows recoding of each distinct spatial voxel by only one laser pulse, this results in maximization of generated fluorescence light per unit excitation power.

LBM has been applied to achieve cellular resolution recordings within a volume of $\sim 5.4 \times 6 \times 0.5$ mm spanning both hemispheres of the mouse cortex and containing more than 1 million neurons at ~ 2 Hz as well as other configuration in which volume size is traded for recording speed. These data provided evidence of covariance of neuronal activity within the population of stimulus-tuned neurons separated by several millimeters across the brain at single-trial level
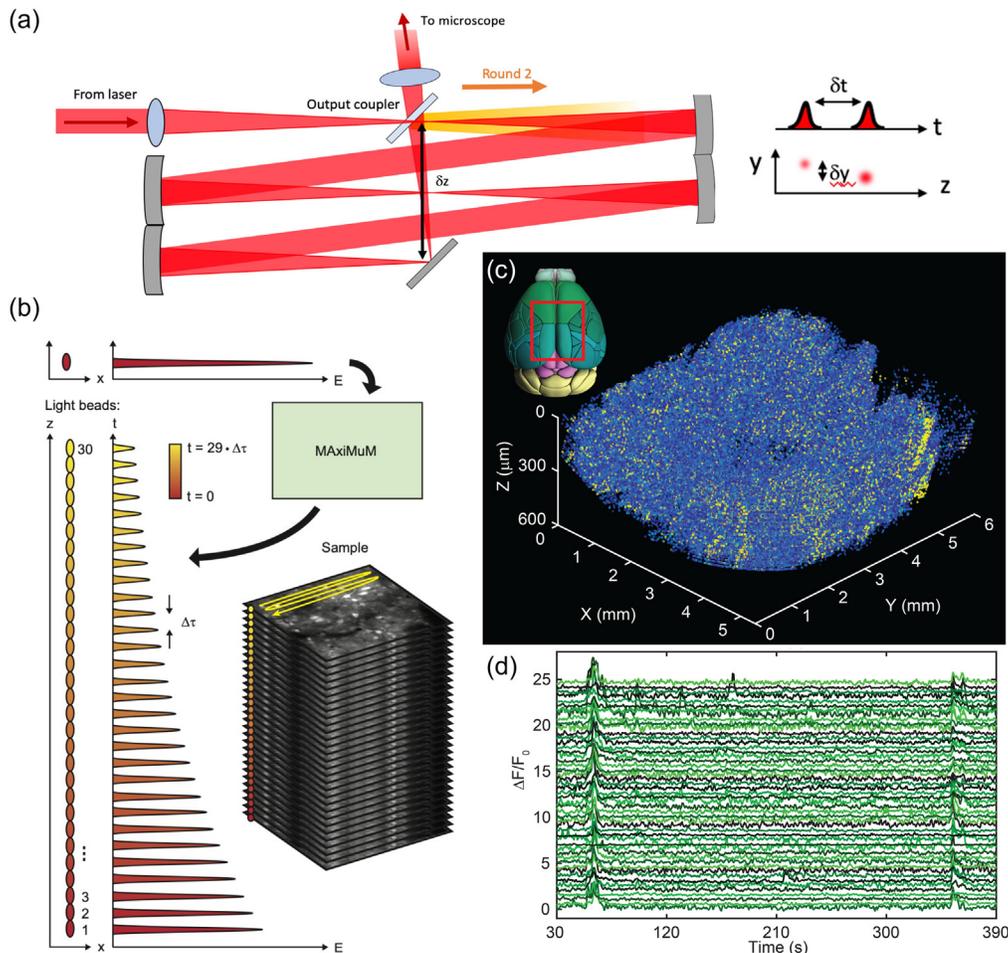
Fig. 25 Light Beads Microscopy: elements and application. (a), (b) The Many-fold Axial Multiplexing Module (MAxiMuM) enables 30-fold temporal multiplexing in the axial direction using a cavity-based design resulting in a set of 30 axially focused beams, "Light Beads" at the sample with $\sigma_{x,y} \sim 1.1 \, \mu$m and $\sigma_z \sim 13 \, \mu$m. A high energy pulse undergoes 30 roundtrips in a slightly imbalanced 8f reimaging cavity and during each round trip a sub-pulse at an appropriate delay is coupled out. Choosing the reflectivity of the output coupler, the exponential falloff of pulse energy can be exactly matched to the required power increase in scattering tissue for all beads. (c) Volumetric recording of 807,748 neurons within $\sim 5.4 \times 6 \times 0.5$ mm^3 at 2.2 Hz within the mouse cortex. 3D rendering of neuron spatial coordinates for a 9-minute recording. (d) Subset of 50 traces from the total of 807,748 extracted neurons, offset: 0.5 ΔF/F$_0$.

representing information on internal states or uncontrolled aspects of external stimuli and behavior.[415]

We expect that in the future, SNR of LBM can be further enhanced using shorter laser pulses and higher bandwidth amplification between the photodetectors and digitizers. Together with development of more efficient, red-shifted indicators these developments are expected to extend the depth of imaging and the size of recorded neuronal population within the limits of tolerable sample exposure to laser light. The ability to record from such large neuronal populations with cellular resolution opens up a range of opportunities for understanding the neurocomputation principles underlying multiregional encoding and processing of sensory and behavioral information across the mammalian brain.

5.5 *Non-Degenerate 2P Microscopy*

In the 2P imaging modalities described above (Secs. 5.1–5.4), a fluorophore was excited by the simultaneous absorption of two photons of the same energy within the near infrared spectrum,
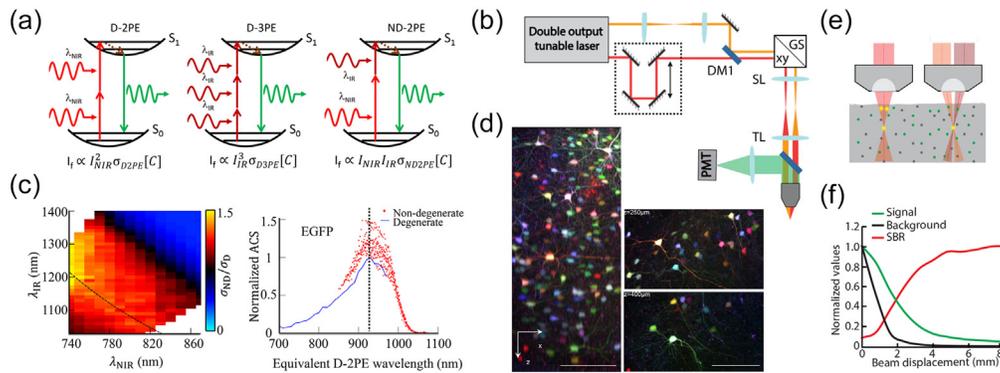
Fig. 26 ND-2PE with collinear and displaced beams. (a) Schematic Jablonski energy diagram for D-2PE, D-3PE, and ND-2PE. I_f, fluorescence signal intensity; I_{NIR} and I_{IR}, intensities of the two laser beams; λ_{NIR} and λ_{IR}, the wavelength of the two laser beams; σ_{D2PE}, σ_{D3PE}, and σ_{ND2PE}, cross-sections for D-2PE, D-3PE, and ND-2PE; $[C]$, fluorophore concentration. (b) Simplified schematic of ND-2PE microscope setup: GS-XY, galvanometer scanner; SL, scan lens; TL, tube lens; DM, dichroic mirror; OL, objective lens; PMT, photomultiplier tube. (c) Left: color-coded normalized non-degenerate absorption cross-section for EGFP as a function of the combination of NIR and IR wavelengths. The cross-section value at each combination of wavelengths was normalized by the peak value of this fluorophore. The isocline corresponding to the ground to excited state transition energy is indicated in dashed black line. Right: normalized cross-section values as a function of the equivalent degenerate wavelength $2/\lambda_D = 1/\lambda_{NIR} + 1/\lambda_{IR}$ are shown in red. Independently measured degenerate cross-section values normalized by its peak within the equivalent range of the total photon energy are shown in black. The black dashed line indicates the position of the peak degenerate absorption used for the normalization procedure (930 nm). These wavelengths correspond to the energy isocline shown in panel (b). (d) Simultaneous excitation of four different fluorescent proteins in Brainbow mouse cortical tissue using ND-2PE with $\lambda_{NIR} = 850$ nm, and $\lambda_{IR} = 1100$ nm. Panel (d) is reproduced with permission from Ref. 473. (e) Left: D-2PE excites the sample both near the surface and within the focal volume. Right: by selecting the two excitation beams for ND-2PE outside of the excitation spectrum of the fluorophores and spatially displacing the beams, the sample is excited only in the focal volume where two beams overlap. (f) Simulation results for the normalized values of signal, background, and SBR versus the beam displacement from the colinear configuration.

derived from the same pulsed laser beam. This is known as "degenerate" 2P (D-2P) excitation. Alternatively, the same energy needed for the transition to the excited state can be delivered via absorption of two photons of different energy (i.e., different color) [Fig. 26(a)]. This is "non-degenerate" 2P excitation (ND-2PE). ND-2PE has a long history in the chemical physics and microscopy.[474–477] Using ND-2PE, we can vary the energies of the individual photons ($\hbar\omega_1$ and $\hbar\omega_2$) while keeping the sum energy $E = \hbar(\omega_1 + \omega_2)$ constant. The first laser beam can be tuned within the standard near-infrared range of excitation wavelengths used in conventional 2P microscopy, placing the second laser beam within the short wavelength infrared wavelengths range for excitation of visible emission fluorophores (green to red). Due to the requirements of two temporally synchronized pulsed beams [Fig. 26(b)], it is preferential to use a single source as a master oscillator. Commercially available turn-key options include dual output femtosecond lasers with one beam fixed at 1040-nm and a second tunable beam.[478] To gain more tuning flexibility, one can also use a femtosecond Ti:Sapphire laser pumping an Optical Parametric Oscillator (OPO).[479–481]

ND-2PE results in an increase in the probability of 2P excitation,[480,482] quantified as the excitation cross-section – an important parameter that, for a given fluorophore concentration and laser power, translates into brighter fluorescence. Because laser illumination may have adverse effects on live biological tissues, large cross-section is always a desirable feature at the focus of fluorophore engineering.[277] Importantly, ND-2PE does not alter the shape of 2P absorption spectrum, so that that the peak absorption remains the same [Fig. 26(c)].

ND-2PE has been used to extend the excitation wavelength range providing a third "virtual" excitation wavelength.[473,483,484] Using synchronized pulses from a femtosecond laser and an

OPO, Mahou et al. demonstrated simultaneous excitation of four different fluorescent proteins in Brainbow mouse cortical tissue[473] [Fig. 26(d)]. ND-2PE has also been explored to increase spatial resolution (Refs. 485, 486 2004 #2024) and penetration depth in scattering media.[487,488] Importantly, ND2P excitation can be used to suppress the background (out-of-focus fluorescence) by choosing their wavelength outside of the D-2PE spectrum of the fluorophores and shaping the beams to overlap only at the focal spot.[478,488–491] For example, one can arrange the beams to enter the back aperture of the objective side-by-side parallel to each other and the optical axis [Fig. 26(e)]. This arrangement reduces their overlap above the focal plane minimizing the background at the price of reducing the effective numerical aperture (NA) for each beam.[478,492] Simulation studies using a beam propagation model have shown that the amount of enhancement in the signal-to-background ratio (SBR) depends on the amount of displacement [Fig. 26(f)]. Both the efficiency of ND-2PE (signal) and out-of-focus fluorescence (background) decrease by increasing the spatial separation of the beams. However, the background decreases at a higher rate leading to the overall increase in SBR.[478]

Further studies are required to optimize the key parameters important for achieving the optimal SBR in ND-2PE: the amount of displacement, the beam size, and the quality of the beam overlap in the focal volume. These improvements would allow increasing the depth penetration of 2P microscopy, particularly in cases of dense fluorescence labeling.

5.6 *Three-Photon (3P) Microscopy*

As we discussed above, 2P microscopy (2PM)[428] in combination with genetically expressed fluorescent probes[493] has been enormously influential in neuroscience. It opened the door for studies of brain structure and function with cellular and subcellular resolution in living animals. The main limitation of this technology is depth penetration: SBR deteriorates when imaging deep into the brains.[494] This problem is commonly known as out-of-focus background fluorescence (mentioned in Sec. 5.5). 3P microscopy (3PM, Fig. 27)[497] overcomes this "fundamental" limitation.

The deep tissue penetration capability of 3PM derives from the longer excitation wavelengths to reduce tissue scattering[497–499] and the higher-order nonlinear excitation to steepen the drop in the probability to excite fluorescence away from the focus.[415,497,500,501] In contrast to 2PM, 3PM is not limited by out-of-focus fluorescence, so far even in densely labeled samples.

Long wavelength 3PM is being applied to deep tissue imaging beyond the depth limit of 2PM, such as 3PM of GCaMP-labeled neurons in the mouse hippocampus[497] and 3PM of quantum-dot-labeled mouse brain vasculature at > 2.1 mm depth.[496] 3PM is capable of imaging through a highly turbid layer such as through the intact skull of adult mouse[495] and adult zebrafish.[502] 2PM and 3PM can be combined for simultaneous imaging of both the cortical layers and the subcortical regions.[424] By leveraging blue-shifted 3P excitation, simultaneous imaging of multiple fluorophores can be achieved. For example, commonly used blue, green, yellow and red fluorescent proteins can be 3P excited using a single excitation beam at 1340 nm,[503] enabling four color, deep tissue imaging.

While long wavelength 3PM has significantly increased the penetration depth of high spatial resolution fluorescence imaging, there are a number of limitations that must be overcome for 3PM to achieve its full potential. 3P excitation is inherently weaker than 2P excitation.[504,505] In fact, the 3P signal strength sets the practical limit of the imaging depth of 3PM today.[506] Therefore, improving the 3P signal is essential to increasing the 3P imaging depth. Large 3P cross-sections,[503] adaptive optics,[507,508] and imaging the regions of interest only[509] can improve the 3P signal. Furthermore, the laser source for 3PM is not yet optimized for deep tissue penetration, and the complexity and cost of the excitation source is a major barrier for the applications of 3PM. An excitation source with cost and user experience similar to a Ti:Sapphire laser for 2PM is necessary to make deep tissue 3PM a routine instrument for brain research. Finally, foundational knowledge of many parameters for 3PM is not yet available. For example, the spectral properties of 3P cross-sections have not been studied for nearly all dyes and fluorescent proteins at wavelengths >1100 nm. Although the scattering and absorption characteristics of the mouse brain between 1300 nm and 1700 nm have been measured recently,[495,510] systematic studies of tissues are needed for other brains (e.g., fly, fish, non-human primate, etc.) to define
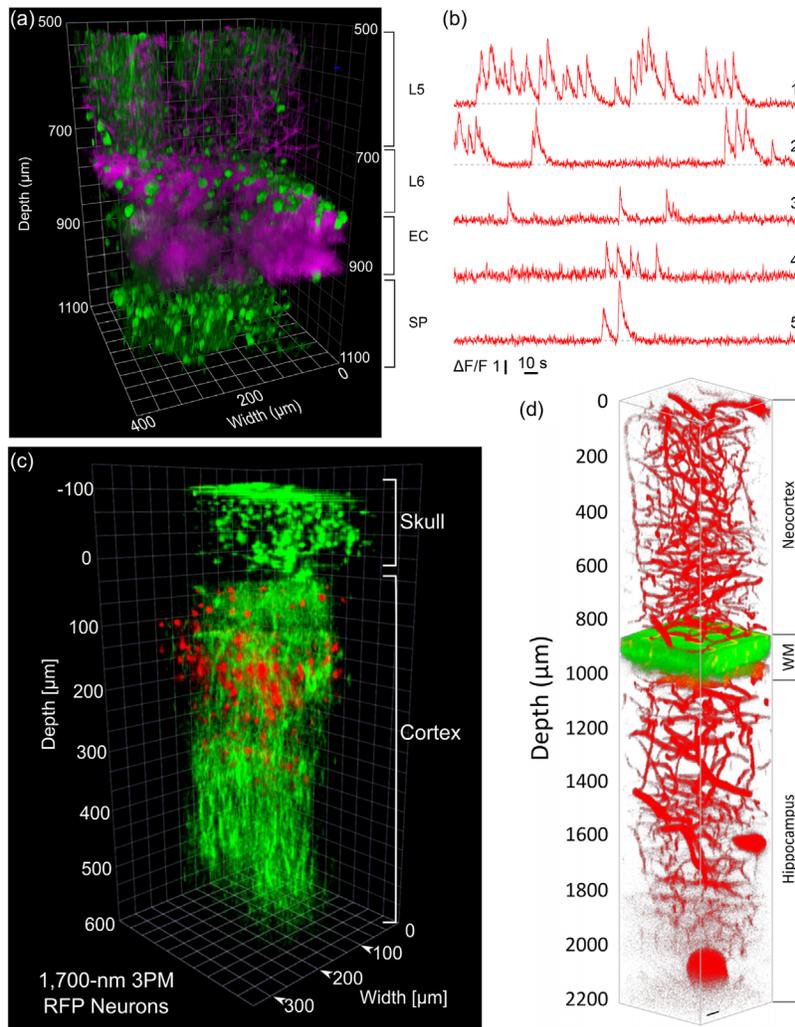
Fig. 27 Deep imaging with 3PM. (a) 3PM of GCaMP6s-labeled neurons in the mouse cortex and the hippocampus. Green, fluorescence; magenta, third-harmonic generation (THG). (b) Activity recording in the Stratum Pyramidale layer of the hippocampus at ~1 mm depth. Only a small portion of the 48-minute recording session is shown. Reproduced with permission from Ref. 416. Springer Nature. (c) Imaging through the intact mouse skull. Red, RFP-labeled neurons in a Brainbow mouse, male, 12 weeks. Green, THG. The zero depth is set just beneath the skull. Reproduced with permission from Ref. 495. Springer Nature. (d) *In vivo* 3PM of mouse brain vasculature labeled with quantum dots (Qtracker 655) to ~2.2 mm depth. Reproduced with permission from Ref. 496, © 2019 American Chemical Society.

the application space for 3PM and lower the barrier of adoption of the 3PM technique beyond the mouse brains.

5.7 *Wearable Multiphoton Microscopes*

Both 2P and 3P microscopes have been miniaturized to enable imaging in freely behaving animals. Compared to 1P miniscopes (Sec. 4.2), their 2P counterparts offer higher resolution, both laterally and axially, and larger depth penetration (up to ~300 μm) [Figs. 28(a)–28(c)].[372,373,418] Depending on the scanning modality, frame rates of up to ~40 Hz (but typically ≤15 Hz) can be achieved. 3P miniscopes offer even larger imaging depths (up to ~1.1 mm in the cortex) but require low-repetition-rate amplified laser systems and special fibers in less widespread use [Figs. 28(d)–28(f)].[417] Due to their reliance on short-pulse lasers and photomultiplier tubes
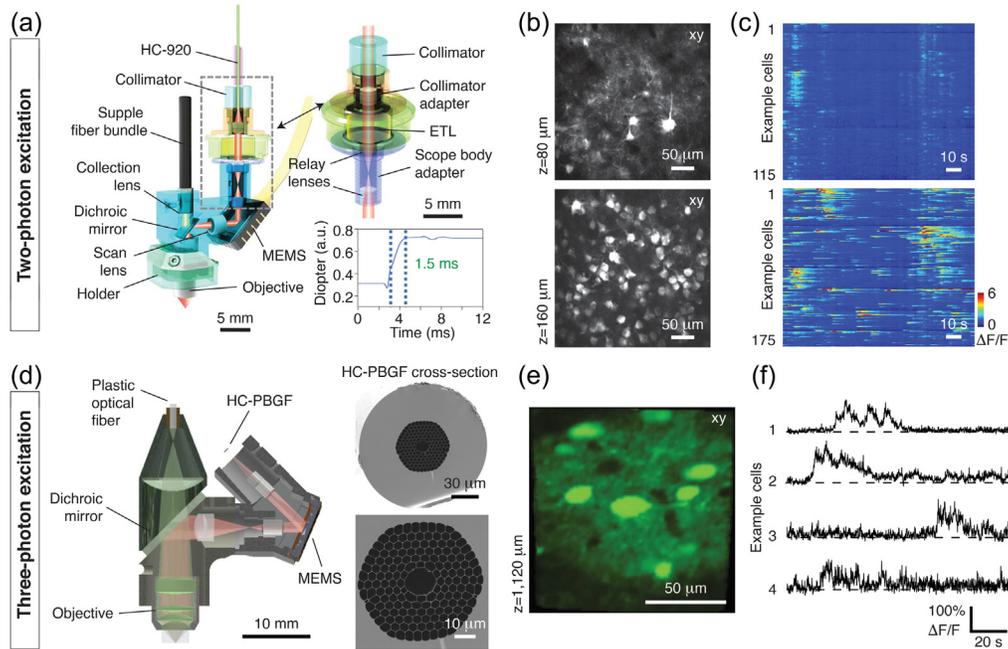
Fig. 28 2P and 3P wearable microscopes for cellular-resolution imaging in freely behaving animals. (a) Example 2P miniscope for high-resolution imaging at depth. This implementation weighs 4.2 grams and includes an electrically tunable lens (ETL) (top right) for rapid focus adjustment across a 180 μm focal range (bottom right). Using a microelectromechanical system (MEMS) scanner, the miniscope allows 10 Hz recordings at 512 x 512 pixels resolution across a 420 μm FOV. (b) Example images of GCaMP6s-expressing neurons acquired at the indicated focal depths (z) in the mouse prefrontal cortex. (c) Ca^{2+} transients from dendritic (top) and cell body regions of interest (ROIs) (bottom) within the focal planes shown in (b). (d) 3P miniscope for deep, high-resolution imaging. This microscope weighs 5 grams and includes a 1.2-m hollow-core photonic bandgap crystal fiber (HC-PBGF) (right) for low-dispersion delivery of the ~1,320 nm excitation light-pulses. A plastic optical fiber collects the emitted fluorescence for remote detection by photomultiplier tubes (PMTs). (e) Image of GCaMP6s-labeled rat cortical neurons at the indicated focal depth (z) in the posterior parietal cortex. (f) Ca^{2+} spiking from four example neurons recorded at 1,120 μm cortical depth. (a)–(f) Adapted with permission from Nature Publishing Group: (a)–(c) from Ref. 418 and (d)–(f) from Ref. 417.

(PMTs) for fluorescence excitation and detection, respectively, multiphoton miniscopes are fiber-coupled. The use of hollow-core (HC) photonic crystal fibers has allowed efficient fluorescence excitation at defined wavelengths [Figs. 28(a), 28(d)]. However, multiphoton miniscopes' attainable field of view tends to be smaller (up to 420 μm but typically ≤300 μm) than their 1P counterparts [Figs. 19(b), 28(b), 28(e)].[372,373] Additionally, their relatively low frame rate and depth-of-field can complicate stable recordings during animal behavior-induced or tissue-intrinsic movements.

In the future, improved laser scanning and optical components may enhance multiphoton miniscopes' FOV, frame rate, and axial beam control [Fig. 28(a)]. Other features may include the ability to perform all-optical or combined imaging and electrophysiological interrogations in unrestrained animals.[352,372]

5.8 Adaptive Optics in Multiphoton Microscopy

Adaptive optics (AO) is a method used in brain imaging to reduce the blurring effect of wavefront distortions and recover diffraction-limited performance deep within the brain tissue. AO was first developed for ground-based telescopes to measure and correct the distortion introduced by the turbulent atmosphere on wavefronts of distant astronomical objects.[511,512] It was later
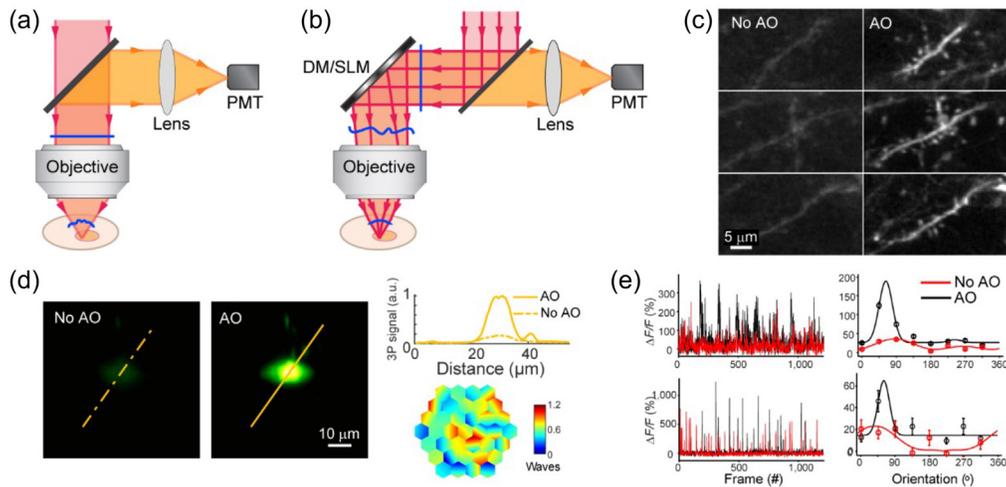
Fig. 29 Adaptive optics enables high-resolution multiphoton microscopy at depth. (a) Wavefront distortion of the excitation light can be (b) corrected with a deformable mirror (DM) or liquid crystal spatial light modulator (SLM) to form a diffraction-limited excitation focus. Blue: wavefront. Red: excitation light. Orange: fluorescence. (c) 2P fluorescence images of dendrites and dendritic spines (606 – 608 μm depth) in the mouse cortex. (d) 3P fluorescence images of a neuron (414 μm depth) in the mouse spinal cord. (e) AO increases Ca^{2+} transient strength $\Delta F/F$ and enables detection of orientation selectivity.

adopted by ophthalmologists to correct the aberrations of the eye for high-resolution imaging of retinal structures.[513,514] With the increasing popularity of multiphoton fluorescence microscopy for *in vivo* brain imaging, AO methods have been developed to measure and correct the distortion that brain tissue imparts on the wavefront of the excitation light [Fig. 29(a)] for high-resolution imaging at depth.[515]

An AO system corrects the distortion or optical aberrations of the image-forming light (i.e., the excitation laser in multiphoton microscopy) by controlling its wavefront with a phase device such as a deformable mirror or liquid-crystal spatial light modulator, so that a diffraction-limited focus can be formed within the sample [Fig. 29(b)]. Effective correction requires accurate measurement of sample-induced aberrations. Methods similar to those applied in astronomy and ophthalmology, where the distortion is directly measured by a wavefront sensor (typically made of a lenslet array and a camera), have been demonstrated for sample preparations with minimal scattering.[516,517] For samples with substantial scattering, indirect wavefront sensing methods have been developed. Some measure wavefront distortion by manipulating the excitation wavefront and detecting its effect on fluorescent signal/image,[518–520] while others measure the electric PSF of the excitation focus directly.[521]

Both direct[522,523] and indirect AO methods[521,524–526] have been applied to 2P fluorescence microscopy for high-resolution structural and functional imaging of the brain down to layer 5b of the mouse cortex[523] and through thinned skull [Fig. 29(c)].[527] Combined with 3P fluorescence microscopy, AO has enabled non-invasive high-resolution imaging of structures such as subcortical synapses and spinal cord neurons [Fig. 29(d)].[506,508] The recovery of diffraction-limited resolution enabled accurate measurement of Ca^{2+} activity from thalamic boutons in layer 4 of the mouse primary cortex [Fig. 29(e)], which led to the discovery of extensive orientation-selective thalamic inputs.[528]

The proof-of-principle experiments described above have firmly established the importance and effectiveness of AO for high-resolution brain imaging at depth. Now it is time for the field to go beyond purely technological demonstrations so that AO can contribute to biological discoveries in the brain. The biggest obstacle is how to integrate AO modules into existing and new microscopes, and to ensure its ease of use and robust performance even in the hands of users with no optical expertise. Further engineering and collaboration with microscope companies will be necessary to realize this goal.

6 Two-Photon Optogenetics

The advent of optogenetic actuators (Sec. 3.10), has ushered a new era in causal neuronal circuit interrogation. Yet, in most "traditional" applications of optogenetic perturbation an entire population of neurons is excited or suppressed together, and furthermore the experimenter often does not observe the neuronal response to the perturbation. However, in essentially every neuronal circuit, the activity of different neurons within a population is heterogeneous. Further, neuronal excitability varies in both space and time, strongly affecting responses to optical stimulation. Thus, providing more nuanced insights into key problems in systems neuroscience like the connection between neuronal code and behavior, requires the advancement of neurophotonic methods with increased precision and built-in optical readout. The resulting set of techniques are often termed "circuit optogenetics"[529] or "all-optical" circuit interrogation.[311,530,531]

6.1 *2P Optogenetic Photostimulation*

From a technical standpoint, stimulating distributed sets of pre-defined neurons in the brain with single-cell resolution has become possible through the advent of holographic 2P optogenetic photostimulation (e.g., Refs. 532–536), which has transformed the study of the behavioral relevance of specific circuits and activity patterns.[313–315,537,538] 2P optogenetic photostimulation utilizes the principle of non-linear 2P absorption to excite light-sensitive opsins within a confined axial plane deep into tissue.[308,532,539] Holographic optical neuronal interfaces (HONIs, in analogy to their holographic optical trap (HOT) predecessors) use phase-modulating spatial light modulators (SLMs) to diffractively shape a distributed excitation pattern in two or three dimensions.[449,540–543] Tightly focused diffraction-limited focal spots maximize 2P excitation efficiency within the focal volume but are not very efficient in modulating behavior of the targeted neuron, because only a small patch of the cell membrane is affected. Therefore, practical implementation of 2P optogenetics commonly relies on one of the two general strategies: rapidly scanning a diffraction-limited spot to cover a large fraction of the cell's membrane[310,314,315,532,536] or defocusing (i.e., spatially expanding) the focal spot to cover the entire cell body[533,535,537,539,544–546] [Figs. 30(a)–30(b)]. The first approach generally trades robustness of optogenetic actuation with temporal precision, and typically lacks the high temporal resolution necessary for generation of precise spike timing to reproduce spatiotemporally patterned activity. The second approach requires more complex hardware. In addition, temporally focused 2P excitation[311,438,544] is used to decouple the lateral and axial dimensions of the excitation spots by shaping the light pulse's spatiotemporal profile.

All-optical HONIs technology is a highly active area of neurophotonics and multiple recent studies have advanced key performance attributes of the optogenetic probes and the spatiotemporal characteristics of the generated light patterns. Several new families of red-shifted optogenetic probes were developed and/or characterized primarily for this application including Chrimson,[337] ReachR,[549] ChRome[535] and ChRmine,[314] soma-targeting strategies were developed for increased efficacy and precision,[533,535,550,551] and transgenic animals that express these probes under genetic control have been developed[546,552] (see also Sec. 3.10). While these opsins have the desirable property of being effectively excited at the ~1040 nm wavelengths of many common pulsed lasers, their extended excitation shoulder at shorter wavelengths means that they suffer from unwanted "cross-talk" excitation from the 2P imaging laser (which becomes worse for more sensitive probes). One possible alternative strategy being developed is to combine a blue-shifted opsin like CoChR with a red-shifted indicator like jRCamp.[534,551] While earlier studies in this area excited neurons with moderate temporal precision (typically >50 ms), sensitive probes and effective excitation from amplified laser sources with low repetition rate now enable millisecond-precise stimulation,[314,533,535,538,546] turning SLM switching times into the limiting factor. Increasing this performance parameter is possible by employing rate-optimized SLMs[314] (where the liquid crystal elements are also heated), by sequentially stacking several SLMs,[314] or by sequentially illuminating different sectors of the SLM[553,554] —a technique first developed for rapid pulse shaping.[555] While holographic patterning of diffraction-limited focal spots in 3D is quite straightforward, development of temporally focused holographic stimulation required creative optical solutions.[311,531,542,556–558]
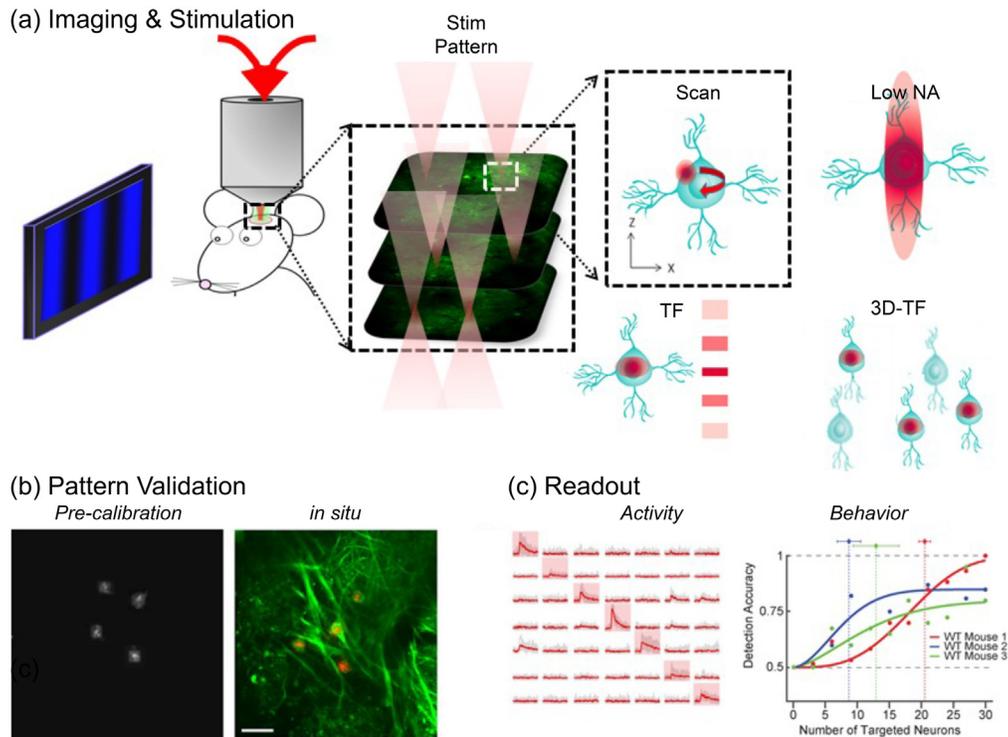
Fig. 30 Precision optogenetic modulation of neuronal circuits and behavior. (a) All-optical precision circuit interrogation is enabled by combining 2P imaging and cell-targeted holographic stimulation of a distributed pattern of multiple neurons, typically using a dedicated low-repetition rate (amplified) femtosecond laser. The illumination is extended across each neuron's membrane by either rapid scanning, reducing the effective numerical aperture (at the cost of optical sectioning) or by parallel illumination of temporally focused extended shapes in two or three dimensions. (b) An array of methods are being developed to calibrate the projected light patterns, adjust as needed, and "smooth" their intensity profile (by minimizing holographic speckle[547]), and in some cases, validate and correct their precise targeting *in situ* inside the tissue.[548] (c) Beyond target validation, all-optical precision neurophotonic interfaces enable direct readout of the effects of circuit perturbations with simultaneous imaging of neuronal activity (left panel from Ref. 536). This paradigm can be used to infer circuit connectivity and dynamics. One can also infer neuronal activity indirectly through animal behavioral reports of its (perturbed) perceptual experience (right panel, from Ref. 538), which informs us about the behavioral relevance of specific neurons and coding features.

6.2 *Combining Precision Optogenetics with Psychophysical Measurements*

These advances, together with a complementary toolbox of experimental and analysis techniques, have set the stage for neurophotonic probing of the precise relationship between subtle circuit manipulations and the observed behavior [Fig. 30(c)]. Population-wide circuit perturbation often leads to dramatic and easily detectable behavioral effects. In contrast, early attempts to apply precision optogenetics in awake behaving animals have failed to evoke measurable behavioral effects.[532] To date, several (non-exclusive) strategies to address this challenge have emerged. The first one is to intensify the manipulation, e.g., by increasing its duration.[313–315] The second strategy is to train the animal to detect or discriminate among purely synthetic percepts. In the process of such training, animals become increasingly sensitive to subtle perturbations, reducing their perceptual thresholds by several orders of magnitude. This approach underlies recent studies on the coding logic of olfactory,[538,559,560] and visual[561] perception. Efforts in this area are often inspired by classical studies that have used subtle electrical stimulation to bias sensory psychophysical curves.[562]

Due to the above-mentioned neurophotonic advances, complex challenges in determining the behavioral relevance of specific features of neuronal circuit activity can now uniquely be

addressed with all-optical circuit interrogation solutions and with unprecedented detail. For example, this toolbox now allows experiments like "leave one out" and cross-excitation of two equivalent populations, providing unprecedented data for computational studies. Likewise, precise manipulation of stimulus timing and inter-neuron synchrony can also be precisely studied. Moreover, changing the parameters of optogenetic actuation by light, including frequency and duration, not only affects the stimulation efficacy, but also provides an important control for possible experimental confounds.[538]

7 Microscopic Imaging of Blood Flow and Oxygenation

Brain cells, including astrocytes and microglia, partner with neurons to maintain healthy brain activity and metabolism (see Secs. 3.6, 3.7). Another important player in this partnership is blood vessels.[563] During neuronal activity, vasoactive molecules and ions released by neurons and glia control the diameter of local microvasculature producing changes in blood flow.[564,565] In parallel, active brain cells consume O_2 causing an increase in O_2 extraction from blood vessels to cerebral tissue. Therefore, measurements of blood flow and oxygenation indirectly reflect neuronal activity.[566] In addition to serving as a surrogate for neuronal activity, these measurements are important in their own right, because perfusion of tissue by blood and the partial pressure of O_2 (pO_2)—in blood vessels and tissue (the interstitial space)—arefundamental physiological parameters in health and disease.

Cerebral blood flow (CBF) can be measured volumetrically with microscopic resolution using OCT that utilizes red blood cell (RBC) motion-induced Doppler shifts (Sec. 7.1). Other optical CBF measurements include laser speckle contrast imaging (LSCI)[567–569] and 2P imaging of RBC velocity.[407] LSCI provides a rapid widefield qualitative characterization of the motion of light scattering particles.[570] 2P measurements of RBC velocity require fluorescent labeling of the blood plasma or RBC.[407,571]

Approaches to microscopic measurements of O_2 in the brain utilize different principles and differ in their degree of invasiveness and sensitivity.[572,573] Depth-resolved real time measurements of intravascular and interstitial pO_2 with micron-scale resolution have been enabled by 2P imaging of phosphorescent nanoprobes (Sec. 3.8). This technique termed '2P phosphorescence lifetime microscopy' or 2PLM (Sec. 7.2) also enables estimation of cerebral metabolic rate of O_2 by quantifying pO_2 gradients around penetrating cortical arterioles.[574,575]

Measurements sensitive to cerebral blood flow, volume and oxygenation are commonly referred to as "hemodynamic." One of the most popular hemodynamic imaging modalities is functional Magnetic Resonance Imaging (fMRI), a macroscopic noninvasive technology commonly used in humans that leverages paramagnetic properties of deoxyhemoglobin to generate signal. Optical hemodynamic imaging technologies create contrast due to differences in the absorption spectrum of oxy- and deoxyhemoglobin.[576] Among them is functional near-infrared imaging (fNIRS),[577] an optical counterpart of fMRI, which we cover in the companion paper dedicated to human optical imaging technologies. In animals, optical intrinsic signal imaging (OISI) has been extensively used for mapping of cortical activity.[578]

Photoacoustics (PA) offers another solution to hemodynamic imaging (Sec. 7.3). This is a hybrid technology that relies on absorption of photon energy to produce other physical phenomena: heat (a change in temperature) and sound (a pressure wave), which is detected by ultrasonic transducers.[579] Photoacoustic microscopy (PAM), which required optical focusing, offers quantification of oxygenation in individual RBCs. Photoacoustic tomography (PAT) provides deeper imaging at the price of lower resolution.[580]

7.1 *Imaging Brain Function with Optical Coherence Tomography*

Cerebral blood flow (CBF) supports brain function by delivering oxygen and other nutrients, while removing waste. Neuronal activity modulates CBF through a process known as "neurovascular coupling." Therefore, measurements of CBF and related hemodynamic parameters can reflect brain function. Earlier (Sec. 2.6), we discussed optical coherence tomography (OCT), which uses optical interferometry to detect echoes of light backscattered from different depths

in tissue,[75] in the context of imaging tissue structure. Over the years, researchers have developed a rich toolbox of functional extensions based on fluctuations of light scattered from red blood cells (RBCs), providing a measurement of brain function. These methods include Doppler,[581] angiography,[582] decorrelation,[583] and capillary transients (RBC passage).[584]

Compared to 2P microscopy, in general, OCT offers slightly greater penetration depths if performed at the same excitation wavelength, enables imaging through less invasive preparations, and does not require extrinsic contrast agents. Amongst optical methods, OCT has the unique advantage of acquiring with depth priority. This enables measuring simultaneously across cortical depths, revealing subtle differences between cortical laminae[585,586] that might otherwise be obscured by physiological noise. This capability has led to OCT angiography studies that pinpoint layer IV as the cortical layer with the largest RBC response to functional activation[585,587] (Fig. 31). Second, OCT acquires three-dimensional volumes in seconds or even fractions of a second, enabling comprehensive assessments of microvascular network dynamics. This capability has led to studies showing flow homogenization during functional activation[588,589] as well as the retrograde propagation of dilation.[590] Third, OCT uses time and confocal gating to reject multiply scattered light and isolate backscattered light from sub-picoliter brain volumes. Such precise control of the light path enables quantitative measurements of capillary speed,[588] oxygenation,[591] hemoglobin concentration,[592] and metabolic rate of oxygen consumption.[592] These baseline measurements are "absolute" in the sense that they can be compared between locations or subjects, and followed over time, unlike conventional laser speckle and optical intrinsic signal imaging. Such baseline measurements provide critical context to interpret neuronal activity-associated changes in hemodynamics or metabolism.

Emerging trends include 1700 nm OCT for imaging of deep cortical and subcortical regions,[83] new contrast mechanisms,[593] and algorithms[594] that may highlight different aspects of brain function at the level of neuroglial tissue. Proper validation against other gold standards, such as multiphoton microscopy,[595] will be critical to provide a sound physiological underpinning for these and other emerging OCT techniques.
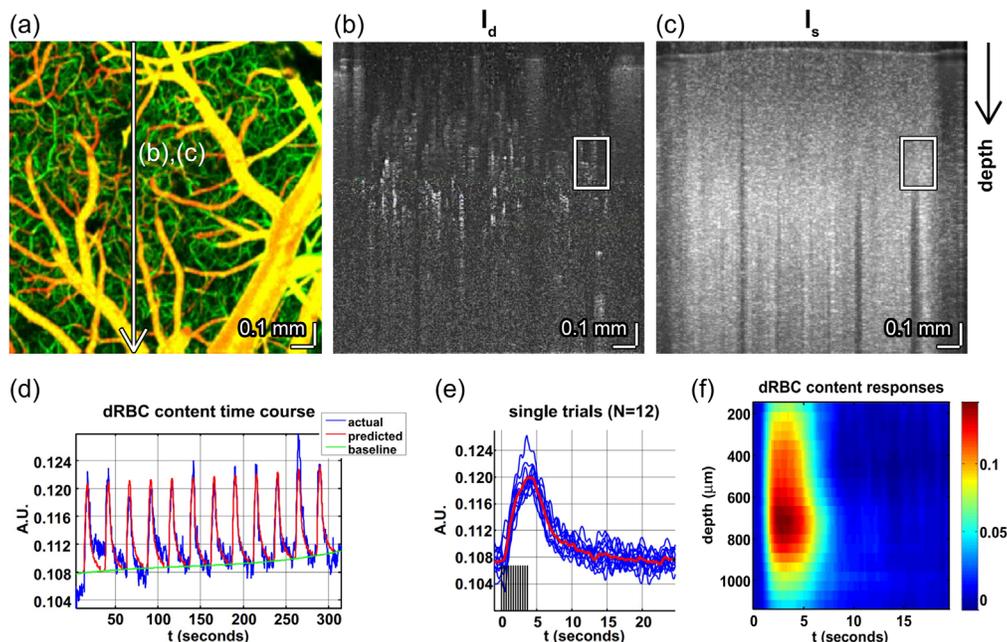
Fig. 31 Angiography and blood flow measurements with OCT. (a) Depth-resolved OCT angiography of the rat somatosensory cortex.[587] Location of OCT cross-sections shown on volumetric angiogram [maximal intensity projection (MIP); superficial vessels in orange-yellow, deep vessels in green]. (b), (c) Cross-sectional angiogram (dynamic intensity, (b)) and static intensity (c) images. (d), (e) Localized changes in dynamic red blood cell (dRBC) content extracted from boxes in (b) and (c), respectively. (f) Depth-resolved measurements show the strongest dRBC responses in middle cortical layers.

7.2 Two-Photon O_2 Imaging

High-resolution, real-time quantification of the partial pressure of O_2 (pO_2) *in vivo* has long been a much-desired objective.[596–599] Development of 2P-enhanced oxygen probes (Sec. 3.8)[124,125,275,600–603] and 2PLM of pO_2 in the brain[268,269] have provided important insights into the brain oxygen metabolism. Among them are confirmation of the "initial dip" in pO_2 upon neuronal activation,[269,270] evidence for artero-venous diffusional shunts in the brain[269] and experimental demonstration of diffusional gradients in O_2 around individual RBCs—the so-called Erythrocyte-Associated Transients (EATs).[269,604]

This technology also enabled estimation of the cerebral metabolic rate of O_2 ($CMRO_2$), a notoriously challenging task,[605] based on pO_2 gradients immediately surrounding diving arterioles (Fig. 32).[574,575] This method relies on 2 assumptions. The first assumption is that peri-arterial tissue gets all its O_2 from the arteriole. This is justified by the absence of capillaries within the periarteriolar space,[606] the presence of a pO_2 gradient in tissue around diving arterioles,[270,575] and a pO_2 decrease within arterioles from the vessel center to the vessel wall indicating the O_2 leaves through the arteriolar wall. This organization can be approximated by Krogh's model of O_2 diffusion from a cylinder[607] where the diving arteriole serves as a single O_2 source for the periarterial tissue. With this model, one can estimate $CMRO_2$ from maps of periarterial tissue pO_2. Recently, this method was used to evaluate baseline $CMRO_2$ across layer in the mouse cortex.

We are only starting to understand microscopic O_2 metabolism, and many questions remain. In current practice, pO_2 measurements are acquired in a "point scan" mode, where the laser beam jumps from point to point. Interleaving of point scan 2PLM with traditional line scan fluorescence measurements would allow near-simultaneous probing of pO_2 and other parameters, such as neurotransmitter release and vasodilation, needed to address important questions about regulation of O_2 delivery to cerebral tissue. Combined with imaging of glucose metabolites (see Sec. 3.6), pO_2 measurements will expand our understanding of the relative contribution of oxidative and non-oxidative metabolic pathways in the brain across different conditions.

7.3 Photoacoustic Imaging

Photoacoustic (PA) tomography (PAT) is a rapidly developing modality that combines optical excitation with ultrasonic detection and can be used over a range of spatial scales at high speed. PAT can utilize endogenous (label-free) contrasts and exogenous probes to provide anatomical, functional, histologic, metabolic, and molecular imaging.[579,608,609]

In PAT, non-ionizing laser pulses ($\sim ps - ns$) are directed to the tissue for excitation. Some of the delivered optical energy is absorbed by the tissue and converted into heat. The heat then induces a pressure rise through thermoelastic expansion. The pressure rise launches an ultrasonic wave, which is referred to as a PA wave. The PA wave is detected by ultrasonic transducers to form an image by a computer. PAT has two primary incarnations: reconstruction-based photoacoustic computed tomography (PACT) and focused-scanning-based photoacoustic microscopy (PAM).[579]
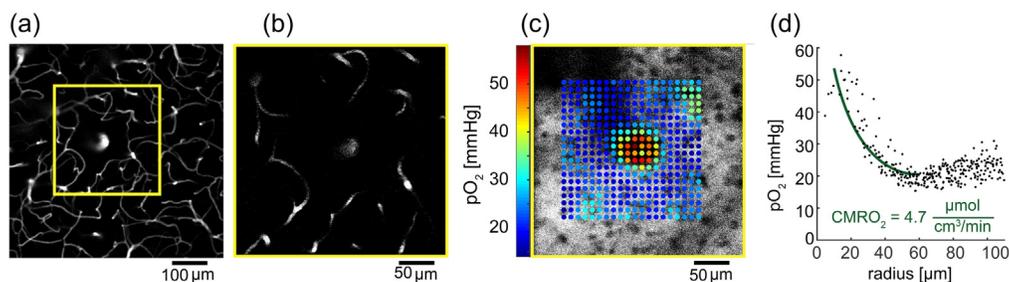
Fig. 32 2P imaging of tissue pO_2. (a) MIP of a 2P vascular image stack of the top 200 μm of cerebral cortex. Contrast is due to intravascular fluorescent dye. (b) Zoomed-in measurement plane. (c) Color-coded pO_2 measurement points overlaid onto the survey phosphorescence image. (c) pO_2 as a function of distance from the center diving arteriole.
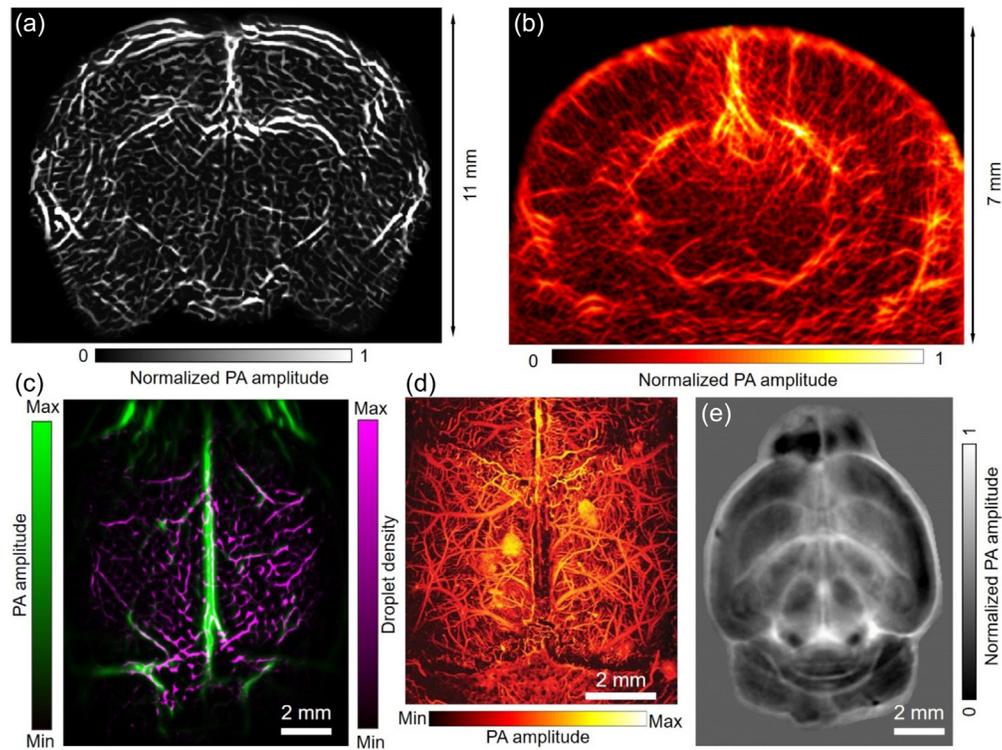
Fig. 33 PAT of the brain. (a) *In vivo* PACT image of a whole rat brain in the coronal plane.[610] (b) *In vivo* high-resolution PACT image of a mouse brain in the coronal plane.[611] (c) *In vivo* superresolution PACT image of a mouse brain, where green shows the conventional PACT signals, and magenta shows the enhanced signals from localized droplets.[612] (d) *In vivo* PAM image of a mouse brain.[613] (e) Cross-sectional PACT image of a mouse brain at 2.8 mm depth.[614]

PAT has found broad applications in neuroscience (Fig. 33). PAM has been used to map cortical vasculature in the mouse brain and quantify oxygen saturation and total concentration of hemoglobin at the single capillary level, based on an endogenous PA contrast—hemoglobin absorption.[613] Label-free PACT has imaged detailed mouse brain structures,[614] provided a measurement of the whole rat brain resting-state functional connectivity,[610] and visualized the epileptic wave propagation across the whole mouse brain during a seizure.[611] More recently, PACT has imaged brain activity in adult humans.[615] Exogenous PA probes are also being developed to monitor glucose metabolism and detect rapid voltage and Ca^{2+} responses to external stimulations in live animals.[616,617]

In the future, we expect that PAT will visualize action potential pulses in the deep brain in rodents with the development of novel voltage/Ca^{2+} indicators operating in the red or near-infrared spectral range. We also expect PAT to be translated to adult human brain imaging, while its current primary barrier is the skull. The adult human skull severely attenuates the excitation light and the emitted PA waves and strongly distorts the PA waveforms, deteriorating image quality. A potential solution is to combine PAT with x-ray computed tomography (CT) or MRI, which can provide accurate skull information to correct for the wavefront distortion. In addition, machine learning methods may play a revolutionary role in this problem due to their high tolerance to skull modeling errors and high computational speed.

8 Hybrid and Multimodal Approaches

In contrast to optical imaging technologies based on detection of photons, hybrid technologies rely on absorption of photon energy to produce other physical phenomena. Above, we discussed photoacoustics (Sec. 7.3) where absorption of photon and heating launches an ultrasonic wave.[579] Ultrasound (US) is also being explored to steer the light in tissue[618] and in US-assisted

optical imaging (Sec. 8.1).[619–622] Recently, the photoacoustic process has been used for spatially confined neuronal stimulation.[623]

Another approach is to combine those technologies that do not interact serving as parallel and complementary information channels extending the spatiotemporal scale, resolution and specificity of each modality alone. For example, implanted "neurophotonic" probes have been developed bearing LEDs and electrodes along the penetrating shanks; LEDs deliver the light required for optogenetics actuation of light-gated ion channels and ion pumps, and electrodes record neuronal activity.[624–626] An alternative solution for depth-resolved optogenetic actuation is tapered optical fibers that allow the light to exit at different locations along the tapered fiber end depending on the angle of incidence of the laser beam entering the fiber. Recording electrodes printed along the fiber enable simultaneous electrophysiological recordings (Sec. 8.2). Another multimodal approach is combining optical imaging with electrophysiological recordings using optically transparent electrode arrays[627–629] (Sec. 8.3). Integration of photodetectors along the shanks of penetrating neurophotonic probes is also being explored.[626] Our final example is simultaneous optical imaging (and optogenetic stimulation) with fMRI[630–634] (Sec. 8.4) that can help physiological underpinning of noninvasive imaging signals and human translation.

8.1 Ultrasound-Enabled Deep Fluorescence Imaging

Light scattering in brain tissue is a barrier to studying the living brain beyond superficial depths. Conventional optical focusing methods rely on ballistic photons, which exponentially decrease with depth. Loss of photons to scattering limits the signal that can be achieved at the focal spot. In addition, scattered photons contribute to out-of-focus excitation. Taken together, these two effects decrease the signal to background ratio (SBR) with depth. Ultrasound (US) scatters less than light in tissue and can be used to image beyond superficial depths, but in general has lower specificity compared to what can be achieved with targeted fluorescent probes.

US has been used to assist optical imaging and photostimulation and has also been explored as a guidestar mechanism for optical wavefront shaping (Fig. 34). Optical wavefront shaping works by tailoring the input optical wavefront to counteract scattering as it travels through the tissue. The scattering properties of tissue (ignoring the contributions by blood cells) is static on the timescale of several seconds at depths up to a few millimeters.[635] Within this time window, knowledge of the relevant parts of the transmission matrix allows the incident wavefront to be pre-distorted to form a desired pattern inside the tissue. In Sec. 5.8, we discussed the use of fluorescent guidestars in multiphoton microscopy. Non-optical guidestars can greatly extend the penetration depth of optical techniques.

The fundamental property that allows the scattering behavior of tissue to be characterized and compensated for is the deterministic nature of elastic scattering.[636] In practice, this property is exploited by latching onto a signal from inside the sample provided by a guidestar to find the needed part of the transmission matrix and correctly modulate the incident light. The predominant methods to find this correct input pattern rely on either feedback optimization or direct conjugation of the signal from a guidestar. In addition to ultrasonic[637] and fluorescent guidestars,[638] other modalities have been explored including kinetic,[639,640] magnetic particle,[641] and photoacoustic[642] guidestars. The performance of these systems is typically benchmarked by the number of independent elements of the transmission matrix that can be controlled and the latency between wavefront recording and playback. The spatial resolution in each case is limited by the nature of the guidestar.

Using wavefront shaping, the penetration depth is no longer limited by scattering (i.e., the transport mean free path) but by the absorption limit. This limit can be several centimeters deep within tissue at wavelengths where absorption is low in the near-infrared regime, and wavefront shaping systems have been demonstrated to successfully focus at depths of up to 2.5 cm in chicken breast and 10 cm in tissue-mimicking phantoms.[643]

However, there are still significant challenges imposed by the temporal dynamics of light scattering in the tissue. *In vivo*, blood flow (i.e., moving red blood cells, RBCs) is a major contributing factor to scattering dynamics. Due to RBC flow, the measured transmission matrix elements can become outdated within several milliseconds even at a depth of 1 millimeter and, due to the nonlinear relationship between scattering path length and penetration depth, this
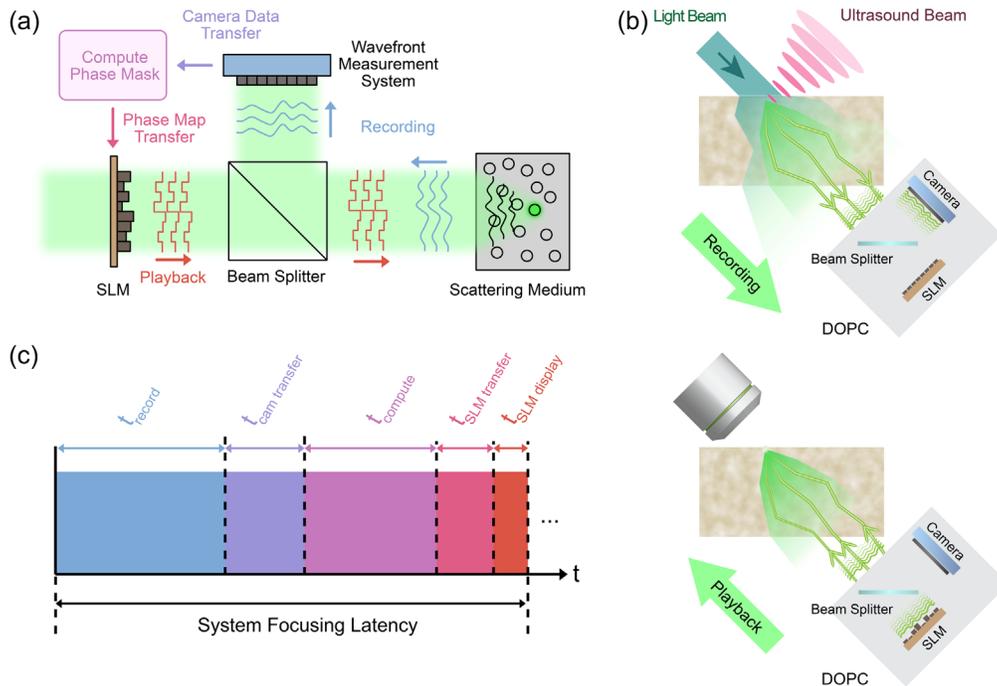
Fig. 34 Wavefront shaping system design. (a) The wavefront shaping system consists of 5 major steps: Recording, camera data transfer, phase mask computation, phase map transfer, and phase map display and playback. First, the scattered light from a guidestar inside the tissue is captured and collected by the wavefront measurement system. Depending on the type of guidestar, the measurement system may use interferometry to detect the signal from the guidestar (e.g., with an ultrasonic guidestar) or simply measure the bulk signal after filtering (e.g., fluorescence from a particle or cell). The captured data from the camera in the measurement system is then transferred to a computing device such as a PC or FPGA where it is processed to find the desired phase map to send light back to the guidestar. Then, this phase mask is transferred to the SLM and displayed to form the shaped playback wave. (b) An example of a wavefront shaping system used to focus light in brain tissue using time-reversed US-encoded light focusing. The US-tagged light is recorded by the camera and then used to calculate the correct wavefront solution to playback a light focus at the previous location of the ultrasonic focus. (c) The sum of the time required to perform each step of the wavefront sensing and shaping process forms the system latency. Typically, the wavefront measurement time is the most significant portion of the process, but when large pixel number cameras and SLMs are used, the time for data transfer becomes significant as well. Parallel processing on embedded systems such as FPGAs can be used to enhance processing time. Furthermore, SLM technologies such as DMDs can be used to reduce the display time to several tens of microseconds as compared to the much slower, millisecond-order liquid-crystal based SLMs.

decorrelation time decreases below one millisecond at a depth of only 2 millimeters.[644] This requires low latency wavefront sensing and shaping systems to maintain the correct wavefront solution. To date, state-of-the-art systems have achieved latencies on the order of a few milliseconds with control of 10^5 optical modes by leveraging fast waveform modulators such as digital micromirror devices.[645] While lower latencies can be achieved with faster modulators such as acousto-optic[646] or microelectromechanical light valves,[647] these techniques typically only offer control over several hundred optical modes.

Recently, a proof-of-principle for another US-enabled fluorescence imaging method has been demonstrated that is not limited by fast speckle decorrelation.[619] Rather, the fluctuating speckle intensity at a point of interest is co-encoded in the emitted fluorescence and US-modulated light. Using the US-modulated transmissions as a decoding key, the fluorescence from the target point at the US focus can be extracted from the overall fluorescence emission. A number of technical challenges associated with this approach still need to be addressed including decreasing the

measurement time and enlarging the field of view. In the meanwhile, wavefront shaping remains the most promising approach for overcoming light scattering.

In the future, we expect wavefront shaping technologies to develop along two main axes:

(1) For some applications where the penetration depth is relatively shallow, such as imaging of deep cortical layers, wavefront distortions are more strongly associated with gross tissue heterogeneity and less impacted by blood flow. These distortions can be addressed with adaptive optics solutions such as the ones described for multiphoton microscopy in Sec. 5.8.

(2) To be able to correct for dynamic light scattering induced by moving RBCs, further technological development is needed to improve system latency by leveraging fast wavefront shaping devices like digital micromirror devices (DMD) and parallelization to solve the data transfer and processing bottlenecks. Currently, wavefront shaping techniques have largely been demonstrated in carefully controlled experiments. To move toward broader adoption, it is necessary to develop strategies tackling the temporal dynamics, especially to reach the ultimate depth limits, and to address practical implementation concerns such as how to interface the wavefront shaping systems with the types of configurations commonly used in neuroscience experiments (e.g., freely moving rodents). To achieve these goals, we envision a wavefront shaping device which will integrate the wavefront sensing and shaping elements such as the one demonstrated in Ref. 648, will be critical to address the wavefront measurement bottleneck by parallelizing the measurement and guaranteeing alignment between the measured and shaped wavefronts.

8.2 *Tapered Optical Fibers as Implantable Multimodal Neuronal Interfaces*

Tapered optical fibers have recently emerged as a new platform for implantable devices to optically interact with deep structures of the mouse brain. These fibers can both deliver or collect light over either large brain volumes or spatially confined subregions all around the conical shape, while generating little to no damage to the brain tissue, comparable to that caused by sharp electrodes used for electrophysiological recordings.[649–651]

Tapered optical fibers have the unique ability of enabling depth-resolved optogenetics and fiber photometry by exploiting the modal properties of the narrowing waveguide: high and low order modes can exchange energy with the brain tissue at different depths along the implant, resulting in a fully integrated and implantable mode-division multiplexer/demultiplexer (MODEM) for brain microcircuitry [Fig. 35(a)]. For example, if the tapered fiber is implanted in cerebral cortex, one can control which cortical layer is being illuminated by changing the input angle of light entering the fiber [see different colors in Fig. 35(a)]. Due to modal mixing of propagating light in the waveguide, the resolution of this technique is in the order of a few hundreds of micrometers. For obtaining finer spatial resolution of light delivery and/or collection, micro and nanofabrication can be employed to coat the fiber with a reflective metal thin layer followed by etching small windows along the tapered end [Fig. 35(b)].[652–654]

Together with the low invasiveness, this technology has contributed to the dissection of basal ganglia neuronal circuitry in the mouse brain: motor-action-related topographical organization of the striatum was probed by depth-selective optogenetic stimulation,[655] while differentiated
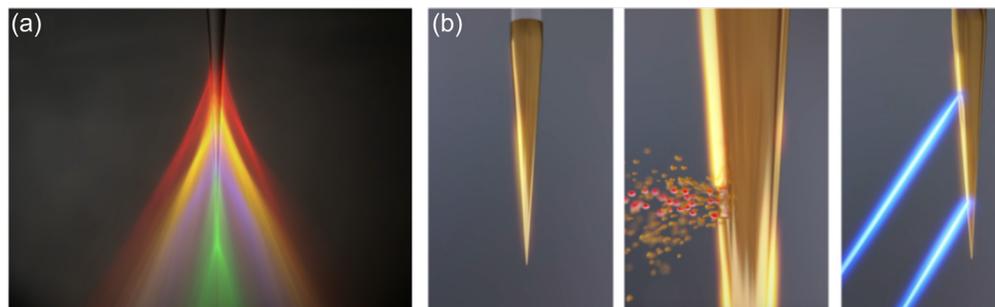
Fig. 35 Tapered optical fibers as neuronal interfaces. (a) Example of how modes of different order outcouple at different sections of a TF. Image is in false colors. (b) High resolution patterning allows structuring the non-planar edge of metal-coated tapered optical fibers.

dopamine transients in dorsal and ventral striatum in reward processing were observed by applying depth-resolved fiber photometry.[651] From the perspective of advanced detection of photons generated in deep brain regions, tapered fibers are compatible with time-correlated single photon counting technologies recently employed to probe the biochemical state of neurons,[656] and can help in bringing this technology to deeper (subcortical) brain structures.[657]

In addition to the ability of carrying excitation or fluorescence light, tapered fibers can host extracellular recording electrodes, resulting an interesting paradigm for probing small brain volume with spatially confined light delivery and electrophysiological recordings.[658] The main challenge in this respect is the non-planar surface of the narrowing waveguide, which does not allow using standard micro- and nano-fabrication techniques.

The photonic properties of tapered fibers also offer the opportunity to control nanoscale light-matter interactions on the fiber surface[659] providing a suitable platform to translate *in vivo* the many options for enhanced biomolecular interfacing using plasmonic resonances that have been proposed *in vitro*.[660] These include Surface Enhanced Raman Scattering (SERS), refractive index sensing, metal-enhanced fluorescence, and highly localized, ultrafast heat delivery in combination with the modulation of the radiative field through sub-wavelength apertures for light delivery and collection in highly scattering tissue.

Next generation technology will therefore have to focus on the development of methods to integrate complex optical and optoelectronic elements on the edge of the fiber taper, aiming at the realization of multifunctional neuronal interfaces targeting both small and wide brain volumes.

8.3 *Transparent Electrode Arrays for Multimodal Brain Mapping*

Optical methods for monitoring and stimulating neuronal activity enable investigating large-scale neuronal networks up to subcellular resolution, and across multiple signaling dimensions. Combining optical tools with electrophysiological recordings allows comprehensive investigations of brain circuits *in vivo*, multi scale, as it leverages the finely tuned spatial resolution of optical imaging with the high temporal resolution and fidelity of electrophysiology. Multimodal studies, however, are not possible with conventional opaque metal microelectrodes, as they block optical access and suffer from photovoltaic artifacts that can contaminate the recordings.[661,662]

Recent progress in materials and fabrication processes for neuroelectronic interfaces has led to the development of transparent microelectrode arrays for simultaneous, artifact-free imaging and recording in the same brain location. These devices typically consist in planar arrays of transparent microscale electrodes (spatial scales ranging from 50 μm to 250 μm) patterned onto <20 μm thin, flexible polymeric films (e.g., parylene, polyimide, PET). The majority of the transparent devices proposed thus far are micro-electrocorticography (microECoG) arrays [Fig. 36(a)],[661–663] although there are a few examples of laminar electrodes for intracortical recordings.[627,666]

The enabling technology behind transparent electrodes are novel nanomaterials that combine high optical transparency for imaging with the electrical conductivity required to record neuronal signals. Graphene—a 2D monoatomic layer of carbon atoms—in particular has emerged as the material of choice for many of these technologies, due to its remarkable combination of transparency, electrical conductivity, biocompatibility, low noise, and resistance to corrosion.[667–669]

From the initial works demonstrating co-localized Ca^{2+} imaging with electrophysiology[627] and optogenetics[661] through graphene microECoG arrays, transparent electrodes have been used for simultaneous LFP recordings, 2P Ca^{2+} imaging in layers II/III of the mouse cortex, optogenetics, and hemodynamic imaging [Fig. 36(b)],[662] for delivering cortical stimulation and concurrently mapping the evoked cortical activation patterns [Fig. 36(c)],[664] and for studying the onset and spreading dynamics of epileptiform discharges *via* simultaneous electrophysiology and wide-field Ca^{2+} imaging [Fig. 36(d)].[663] Graphene electrodes have also been integrated with optic fibers to realize battery-powered devices for closed-loop optogenetics [Fig. 36(e)].[665]

Despite the exciting results, the main drawbacks of transparent graphene microelectrodes are the high interface impedance—which limits the ability to record single extracellular spiking activity—and the complexity of processing and fabrication. In the attempt to overcome
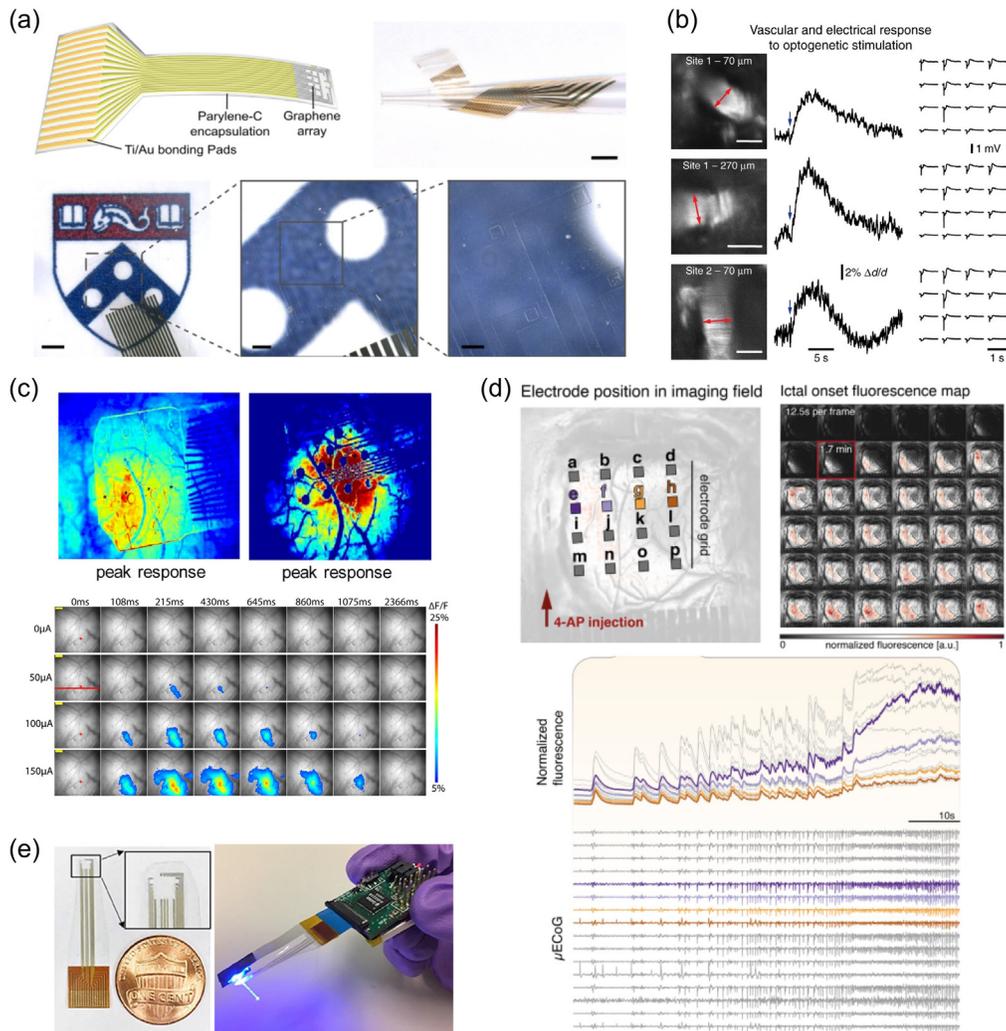
Fig. 36 Multimodal measurements and interrogation of brain activity using transparent electrode arrays and neurophotonic technologies. (a) (Top) Design of a flexible, transparent 16-channel microECoG array for multimodal mapping the dynamics of epileptiform discharges in mouse models.[663] The array is a grid of 50 μm × 50 μm square electrodes with 500 μm spacing (total recording area: 1.55 mm × 1.55 mm, total array footprint 2.75 mm × 2.75 mm. Scale bar: 2 mm). (Bottom) Photographs illustrating the optical transparency of the array in the recording area. Scale bars, left to right: 1 mm, 250 μm, and 100 μm. Reproduced from Ref. 663. (b) Simultaneous optogenetics, recording and hemodynamic imaging in Thy-Cr2 mice through graphene arrays.[662] (Left) Line-scan imaging of arteriolar dilation induced by optogenetic stimulation under two different electrode sites (marker: FITC-dextran, red arrows show line-scan location). Scale bars: 50 μm. (Middle) Average vascular diameter change and (right) light-evoked LFPs recorded at the graphene electrode sites. Reproduced from Ref. 662. (c) Maps of cortical responses to co-localized electrical stimulation delivered through graphene electrodes in GCamp6f mice.[664] (Top) Ca^{2+} fluorescence intensity in response to cortical electrical stimulation under (left) a graphene and (right) a platinum array of the same size. (Bottom) Spatiotemporal maps of cortical activation following electrical stimulation at varying intensities delivered from a transparent graphene electrode (marked with the red star). Adapted from Ref. 664. (d) Multimodal analysis of ictal state transitions in acute mouse preparations induced by 4-aminopyridine (4-AP).[663] (Top left) Schematics of the relative graphene contact positions and 4-AP application site. (Top right) Propagation of the ictal wavefront at seizure onset mapped with wide-field Ca^{2+} epifluorescence imaging. (Bottom) Ca^{2+} fluorescence intensity beneath each electrode and simultaneous microECoG recordings from the graphene array during seizure onset. Adapted from Ref. 663. (e) Closed-loop graphene device for artifact-free optogenetics. (Left) Photographs of the transparent graphene array and (right) the fully assembled battery-powered, closed-loop device integrating the graphene array with an optic fiber for optogenetic stimulation. Adapted from Ref. 665.

these limitations, a number of alternative materials have been explored for transparent micro-electrodes, including carbon nanotubes (CNTs),[670] platinum nanoparticle coatings,[671] conductive polymers (e.g., PEDOT-PSS[628]), and gold nanomeshes.[629,666]

In addition to addressing the impedance, temporal resolution and scalability issues, future work is needed to evaluate the longevity and biocompatibility of graphene-based and other transparent electrode technologies for chronic *in vivo* implants. Furthermore, innovative approaches combining surgical preparations with custom device configurations are required to conduct multi-modal investigations into deeper subcortical regions, which are inaccessible to planar microECoG arrays. Finally, there is a lack of established frameworks for analyzing high-dimensional datasets operating on different spatial and temporal scales, such as those emerging from multimodal optical and electrophysiological mapping of neuronal activity.

8.4 *Optical Imaging and Functional Magnetic Resonance Imaging (fMRI)*

Blood-oxygen-level-dependent (BOLD) fMRI is a widely implemented, clinically and preclinically accessible, noninvasive neuroimaging tool with whole-brain coverage. Despite these strengths, BOLD-fMRI data have relatively low spatiotemporal resolution (sub-millimeter to millimeter, $\sim$1 Hz), and are insensitive to the cellular origins of activity. This can limit the utility and interpretability of BOLD-fMRI measurements.[672] As a complementary neuroimaging tool-set, optical imaging methods have high reporter specificity and spatiotemporal resolution (micron to sub-millimeter, tens to hundreds of Hz), but are limited to optically accessible tissue and to applications in animal models due to the introduction of fluorophores which requires invasive manipulation of the nervous system. Together, optical imaging and BOLD-fMRI provide a link between reporter specific measurements of activity and the most widely used method for assessing human brain function as well as a means of crossing disparate spatiotemporal scales.

BOLD-fMRI and optical imaging can be performed concomitantly (Fig. 37), or serially, to interrogate the physiological reporter specific underpinnings of the BOLD-fMRI signal, explore brain-wide circuit- and network-level activity patterns, and neuro-glio-vascular coupling in health and disease. To collect BOLD-fMRI and optical imaging data from the same subject, significant experimental challenges must be overcome to accommodate the confined space and high magnetic field of the MR-scanner without compromising the optical signal. This can be particularly difficult if the multi-modal data are acquired simultaneously which is necessary when studying certain aspects of brain function such as spontaneous activity (without external stimuli).[673,674]

To date, there are a handful of implementations of BOLD-fMRI with simultaneous single/double-fiber photometry to yield 'point' measurements, or one-dimensional time-courses of optical data and two reports of simultaneous wide-field imaging using fiber-optic bundles to obtain two-dimensional optical images of cortical activity.[630,631,634,675–681] Experimentally, each in-scanner optical imaging implementation includes a means of delivering excitation light to, and relaying optical signal from within the bore, reducing MR-susceptibility artifacts caused by surgeries that yield optical access to the brain, minimizing motion, and eliminating or keeping metal components at a safe distance from the MR-scanner. The signal-processing and analyses of these data follow a variety of strategies that depend on the implementation and scientific question.

In the near future, we expect improved in-scanner optical imaging compatibility with state-of-the-art MRI technology (e.g., imaging with an MR-cryo-coil), experimental versatility (e.g., use of novel or multiple optical probes), and data quality (e.g., better signal-to-noise). Along with these advances in data acquisition, more complex applications will be attempted including implementations in awake behaving animals, disease models, and both young and old subjects. Further, the analyses of these multi-modal data will expand and progress through more wide-spread implementation, data sharing and cross-specialty collaboration. Ultimately, BOLD-fMRI and optical imaging methods have the potential to link animal and human studies and to provide unique insight into the functional organizing principles of the brain in health and disease.

Fig. 37 Concurrent optical imaging and fMRI. (a) Optical imaging implementations within the MRI scanner. Schematic of typical wide-field imaging components (i.). Excitation light is delivered (LED light source), passes through a dichroic mirror, and is focused onto the mouse cortex (1X objective). Emitted fluorescence signal is relayed to a camera and recorded. Example imaging frames from a movie recorded from a mouse expressing GCaMP in glia (Aldh1l1-Cre/Ai162) (top right). Data are collected in-scanner. Blooms of increased activity are in hot colors; epochs of decreased activity are in cool colors. Schematic of a typical fiber photometry experiment (ii.). Excitation light delivered and signal recorded through long fiber optic cables. Both (i.) and (ii.) can be performed within an MRI scanner (iii.) where simultaneous BOLD-fMRI data can be recorded. Wide-field imaging yields measures of cortical activity (2D images), while fiber photometry can target subcortical areas (1D time courses). Simultaneously recorded glia-Ca^{2+} (green) and BOLD (orange) spontaneous activity from a cortical roi are plotted (middle). In this example, these signals are moderately correlated (Pearson's correlation R^2 = 0.52, P < 0.05). (b) In-scanner wide-field imaging. Components and light path are indicated (image reproduced from Ref. 630). For wide-field imaging, optical access to the cortex is gained by resecting the scalp and covering the skull in dental cement, glue, and glass (right). The wide-field imaging data can be registered to the MRI data using the middle cerebral arteries as anatomical landmarks and an MR angiogram. Example multi-modal measurements of spontaneous Ca^{2+} fluorescence and BOLD activity.

Fig. 37 (*Continued*) (c) With multi-modal data registered to a common space (i.), ROIs can be imposed (e.g., Allen Atlas regions) and a connectome computed. Multi-modal spontaneous activity can be used to compute a between contrast transfer function (ii.). Here, gamma-variant fitting[629] was applied to compute a transfer function using simultaneously recorded spontaneous BOLD activity and excitatory neuronal Ca^{2+} activity (Slc17a7/Cam/TeTG6f, N = 6, plotted in blue) or glia Ca^{2+} activity (Aldh1l1-Cre/Ai162, N = 5, plotted in purple). Abbreviations: functional magnetic resonance imaging (fMRI, MRI, MR), light emitting diode (LED), anterior (A), posterior (P), right (R), left (L), dorsal (D), ventral (V), Pearson's correlation (R^2), region(s) of interest (roi, rois), signal intensity (SI), arbitrary units (au), blood-oxygen-level-dependent (BOLD), seconds (secs), echo planar imaging (EPI), repetition time (TR), field of view (FOV), radio frequency (RF).

9 Computational Imaging

Computational microscopy is a class of methods that synergistically combines optical hardware and computational algorithms for enabling novel capabilities that the optics alone do not support (Fig. 38). The motivation is to overcome the many challenges in neuronal imaging. These methods have been broadly applied to 1P or multiphoton imaging of functional indicators (e.g., Ca^{2+} imaging and voltage imaging), OCT, and PA imaging.

The first type of challenges stem from the physical tradeoffs between several desirable imaging parameters, including SNR, imaging speed, spatial resolution, FOV, depth of field (DOF), and the size and weight of the optical device. To overcome this, new types of computational microscopes have been developed to enable high-speed volumetric imaging, enhanced resolution, and extended DOF. For example, Light field microscopy enabled single-shot *in-vivo* 3D recording of neuronal activity[442,682–687] [Fig. 39(a)]. Similar concepts have enabled miniaturized microscopes, such as MiniLFM,[688] Miniscope3D,[690] CM2,[419] and FlatScope,[691] for 3D recording of neuronal activity in freely moving animals [Fig. 39(b)]. Structured illumination microscopy enabled super-resolution reconstruction and background suppression for *in vivo* brain imaging[689,692,693] [Fig. 39(c)].

The second type of challenges stem from the complexity of the large-scale multi-dimensional neuronal imaging data. To overcome this, many advanced computational algorithms have been developed to perform various signal extraction tasks, such as segmentation, enhancement of SNR, image deconvolution, and spike estimation. In the past few years, parametric and model-based techniques, such as principal component analysis (PCA), non-negative matrix factorization (NMF), and sparse deconvolution, have shown tremendous success. In recent years, data-driven machine/deep learning-based techniques have become popular and achieved the state-of-the-art performance in various tasks, such as vessel segmentation in deep brain[694,695] [Fig. 40(a)], neuron segmentation[696,698] [Fig. 40(b)], functional signal denoising[697] [Fig. 40(c)], Ca^{2+} signal extraction,[699,700] 3D deconvolution,[701,702] and super-resolution reconstruction.[703]

In the future, we can expect that computational microscopy will continue to broadly impact both the system design and signal analysis in neuronal imaging. One promising area is to jointly
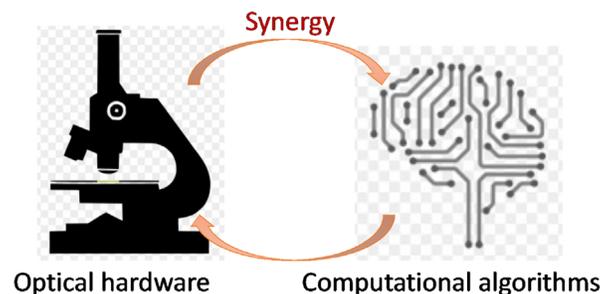
Fig. 38 Computational microscopy synergistically combines optical hardware and computational algorithms.
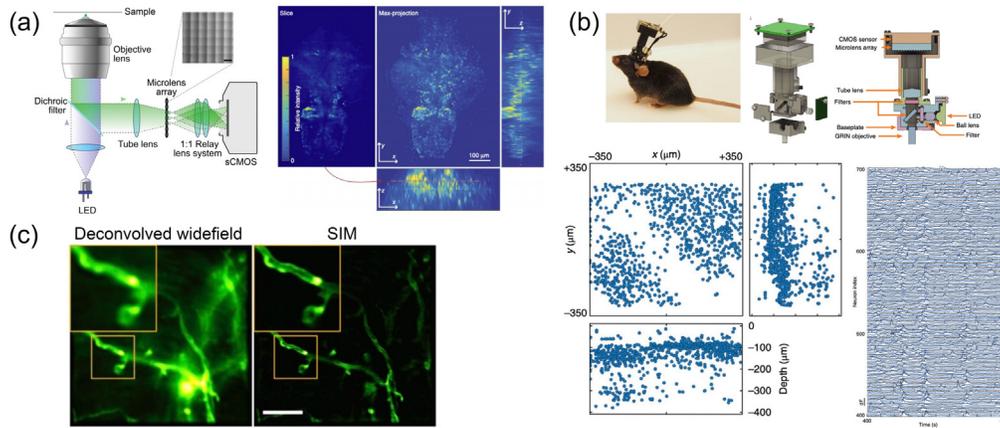
Fig. 39 Computational microscopy enables novel imaging capabilities. (a) Light field microscopy enables single-shot high-speed volumetric neuronal imaging.[442,683] (b) Miniaturized light field microscope allows volumetric neuronal recording in freely moving mice.[688] (c) Structured illumination microscopy achieves super-resolution reconstruction of dendrites expressing ChR2-GFP on the mouse brain *in vivo*.[689]
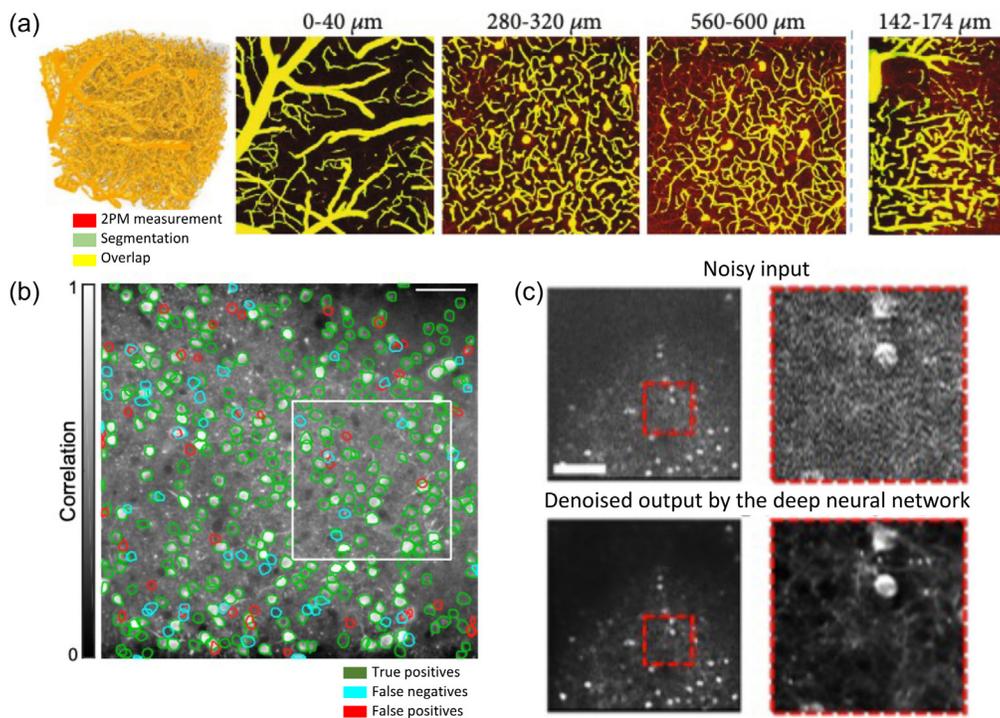
Fig. 40 Deep learning enables state-of-the-art neuronal signal extraction. (a) Vascular segmentation from 2P imaging data.[694] (b) Active neuron segmentation in 2P Ca^{2+} imaging.[696] (c) Denoising 2P Ca^{2+} imaging data.[697]

optimize the optics, acquisition strategy, and computational algorithm in a holistic framework to further push the imaging performance limits. We also anticipate that more advanced deep learning methods beyond the widely used supervised learning methods will be developed, which will incorporate unsupervised learning, semi-supervised learning, physical model-based priors for more data efficient and reliable signal extraction.

10 Conclusions

In this Status Report, we provided a 30,000-foot view of a suite of neurophotonic methods—ranging from molecular sensors to imaging technologies that allow high-speed imaging with large fields of view—that have emerged from the BRAIN Initiative and related large-scale neuroscience efforts. For each domain, we outlined the current state-of-the-art of the respective technologies, identified the areas where innovation is needed, and provided an outlook for future directions. Our goal was not to offer a comprehensive list of all recently developed neurophotonic tools. Further, our choice was often biased toward technologies developed in our own laboratories. We hope, nevertheless, that the overall scope does justice to the breadth of the modern neurophotonics arena spanning across the spatiotemporal scales:[704] from the nanometer scale of molecular sensors to the mesoscale of cortical columns and entire brain areas (hundreds of microns); from the nanosecond scale of fluorescent lifetime to slow changes in mood, executive function, and arousal unfolding over minutes and hours.

Most often, the invasive nature of the methods described in this report limits their direct translation to humans. Exceptions exist, including intraoperative brain imaging[705–707] and/or other situations where the benefit overweighs the probability of the risk. For example, optogenetic methods are being tested in clinical trials aimed at (partial) restoration of vision.[708] Maybe some of the methods presented here will evolve or inspire noninvasive techniques that can be employed in humans one day. But even in cases where the direct translation is prohibited, microscopic imaging in animals has led to better interpretation of noninvasive optical signals achievable in humans. In particular, physiological underpinning of fNIRS (as well as fMRI) signals requires an understanding of the relationship between neuronal network activity, blood flow, and O_2 consumption.[566,709,710] Neurophotonic methods designed to noninvasively probe deep tissue and apply to humans will be the focus of our companion report.

Each of the technologies highlighted in this report has been conceived by a small group of experts, but not without input from the bigger neurophotonics community. In every case, a dialog with the community and parallel efforts elsewhere have been instrumental in driving innovation, providing a testbed for early developments, and fine-tuning the new technology to serve specific applications. Among the most significant measures of the success for these efforts are ever-expanding collaborative ties between the technology and biology experts and growing global science network across countries and continents.[3,711]

As impressive and significant as the recent progress has been, we are just getting started. Our next challenge as a community is to sustain the momentum beyond the lifetime of any individual program or initiative. Needless to say, this entails, among others, retaining and nurturing the best of our students. So, if you are a student reading these lines, we would like to conclude by speaking directly to you:

> *Dear Student, thank you for making it to the end of this report. We appreciate your curiosity and persistence. At the risk of sounding self-congratulatory, we would like to tell you that each of the tools featured here is a story of ingenuity, perseverance, and tireless work. Each one is a personal story of trial and error, triumph and failure, a bold vision baked into a dry and meticulous scientific approach. These are technologies made by people. We are using light to illuminate the future, and it's never been so bright! Come and join us in this endeavor!*

Disclosures

M.D.V., B.L.S., Fe.P. are founders and hold private equity in Optogenix, a company that develops, produces, and sells technologies to deliver light into the brain. L.V.W. has a financial interest in Microphotoacoustics, Inc., CalPACT, LLC, and Union Photoacoustic Technologies, Ltd., which, however, did not support this work. T.C. is the mentor of a start-up endeavor DeepEn, which develops commercial holographic endoscopes. N.J. and Howard Hughes Medical Institute have filed patent applications that relate to adaptive optics. T.F.A. and K.M.N.S.N. have a financial interest in Agile Diffraction Ltd., which aims to commercialize the Acousto-Optic Lens (AOL) technology. D.S.P and Columbia University have patents related to multiphoton photostimulation. E.M.C.H. and Columbia University hold intellectual property rights on SCAPE, some of which are licensed to Leica Microsystems.

Acknowledgments

References

1. T. R. Insel, S. C. Landis, and F. S. Collins, "Research priorities. The NIH BRAIN initiative," *Science* **340**(6133), 687–688 (2013).

2. A. Devor et al., "The challenge of connecting the dots in the B.R.A.I.N," *Neuron* **80**(2), 270–274 (2013).

3. S. Grillner et al., "Worldwide initiatives to advance brain research," *Nat. Neurosci.* **19**(9), 1118–1122 (2016).

4. E. A. Rodriguez et al., "The growing and glowing toolbox of fluorescent and photoactive proteins," *Trends Biochem. Sci.* **42**(2), 111–129 (2017).

5. K. Chung et al., "Structural and molecular interrogation of intact biological systems," *Nature* **497**(7449), 332–337 (2013).

6. B. C. Chen et al., "Lattice light-sheet microscopy: imaging molecules to embryos at high spatiotemporal resolution," *Science* **346**(6208), 1257998 (2014).

7. E. M. C. Hillman et al., "Light-sheet microscopy in neuroscience," *Annu. Rev. Neurosci.* **42**, 295–313 (2019).

8. S. W. Hell, "Microscopy and its focal switch," *Nat. Methods* **6**(1), 24–32 (2009).

9. B. Huang, M. Bates, and X. W. Zhuang, "Super-resolution fluorescence microscopy," *Annu. Rev. Biochem.* **78**, 993–1016 (2009).

10. P. W. Tillberg et al., "Protein-retention expansion microscopy of cells and tissues labeled using standard fluorescent proteins and antibodies," *Nat. Biotechnol.* **34**(9), 987–992 (2016).

11. I. Costantini et al., "Autofluorescence enhancement for label-free imaging of myelinated fibers in mammalian brains," *Sci. Rep.* **11**, 8038 (2021).

12. A. L. A. Mascaro et al., "Label-free near-infrared reflectance microscopy as a complimentary tool for two-photon fluorescence brain imaging," *Biomed. Opt. Express* **6**(11), 4483–4492 (2015).

13. E. Min et al., "Serial optical coherence microscopy for label-free volumetric histopathology," *Sci. Rep.* **10**, 6711 (2020).

14. A. J. Schain, R. A. Hill, and J. Grutzendler, "Label-free in vivo imaging of myelinated axons in health and disease with spectral confocal reflectance microscopy," *Nat. Med.* **20**(4), 443–449 (2014).

15. H. Wang, J. F. Zhu, and T. Akkin, "Serial optical coherence scanner for large-scale brain imaging at microscopic resolution," *Neuroimage* **84**, 1007–1017 (2014).

16. C. Leahy, H. Radhakrishnan, and V. J. Srinivasan, "Volumetric imaging and quantification of cytoarchitecture and myeloarchitecture with intrinsic scattering contrast," *Biomed. Opt. Express* **4**(10), 1978–1990 (2013).

17. R. Y. Tsien, "The green fluorescent protein," *Annu. Rev. Biochem.* **67**, 509–544 (1998).

18. G. G. Lambert et al., "Aequorea's secrets revealed: new fluorescent proteins with unique properties for bioimaging and biosensing," *PLoS Biol.* **18**(11), e3000936 (2020).

19. N. C. Shaner et al., "Improved monomeric red, orange and yellow fluorescent proteins derived from Discosoma sp. red fluorescent protein," *Nat. Biotechnol.* **22**(12), 1567–1572 (2004).

20. H. Hoi et al., "An engineered monomeric Zoanthus sp yellow fluorescent protein," *Chem. Biol.* **20**(10), 1296–1304 (2013).

21. Y. Shen, T. Lai, and R. E. Campbell, "Red fluorescent proteins (RFPs) and RFP-based biosensors for neuronal imaging applications," *Neurophotonics* **2**(3), 031203 (2015).

22. D. M. Shcherbakova et al., "Near-infrared fluorescent proteins: multiplexing and optogenetics across scales," *Trends Biotechnol.* **36**(12), 1230–1243 (2018).

23. D. S. Bindels et al., "mScarlet: a bright monomeric red fluorescent protein for cellular imaging," *Nat. Methods* **14**(1), 53–56 (2017).

24. M. G. Eason, A. M. Damry, and R. A. Chica, "Structure-guided rational design of red fluorescent proteins: towards designer genetically-encoded fluorophores," *Curr. Opin. Struct. Biol.* **45**, 91–99 (2017).

25. J. B. Grimm et al., "A general method to improve fluorophores for live-cell and single-molecule microscopy," *Nat. Methods* **12**(3), 244–250 (2015).

26. J. Dou et al., "De novo design of a fluorescence-activating beta-barrel," *Nature* **561**(7724), 485–491 (2018).

27. H. W. Yeh et al., "Red-shifted luciferase-luciferin pairs for enhanced bioluminescence imaging," *Nat. Methods* **14**(10), 971–974 (2017).

28. S. Iwano et al., "Single-cell bioluminescence imaging of deep tissue in freely moving animals," *Science* **359**(6378), 935–939 (2018).
29. M. Helmstaedter et al., "Reconstruction of an average cortical column in silico," *Brain Res. Rev.* **55**(2), 193–203 (2007).
30. A. Erturk et al., "Three-dimensional imaging of solvent-cleared organs using 3DISCO," *Nat. Protoc.* **7**(11), 1983–1995 (2012).
31. I. Costantini et al., "In-vivo and ex-vivo optical clearing methods for biological tissues: review," *Biomed. Opt. Express* **10**(10), 5251–5267 (2019).
32. T. Ku et al., "Multiplexed and scalable super-resolution imaging of three-dimensional protein localization in size-adjustable tissues," *Nat. Biotechnol.* **34**(9), 973–981 (2016).
33. Y. G. Park et al., "Protection of tissue physicochemical properties using polyfunctional crosslinkers," *Nat. Biotechnol.* **37**(1), 73–83 (2019).
34. E. Murray et al., "Simple, scalable proteomic imaging for high-dimensional profiling of intact systems," *Cell* **163**(6), 1500–1514 (2015).
35. D. Choquet, M. Sainlos, and J. B. Sibarita, "Advanced imaging and labelling methods to decipher brain cell organization and function," *Nat. Rev. Neurosci.* **22**(4), 237–255 (2021).
36. T. Pfeiffer et al., "Chronic 2P-STED imaging reveals high turnover of dendritic spines in the hippocampus in vivo," *Elife* **7**, e34700 (2018).
37. V. Inavalli et al., "A super-resolution platform for correlative live single-molecule imaging and STED microscopy," *Nat. Methods* **16**(12), 1263–1268 (2019).
38. J. Tonnesen, V. Inavalli, and U. V. Nagerl, "Super-resolution imaging of the extracellular space in living brain tissue," *Cell* **172**(5), 1108–1121.e15 (2018).
39. S. W. Hell, "Far-field optical nanoscopy," *Science* **316**(5828), 1153–1158 (2007).
40. A. Furstenberg and M. Heilemann, "Single-molecule localization microscopy-near-molecular spatial resolution in light microscopy with photoswitchable fluorophores," *Phys. Chem. Chem. Phys.* **15**(36), 14919–14930 (2013).
41. K. Xu, G. Zhong, and X. Zhuang, "Actin, spectrin, and associated proteins form a periodic cytoskeletal structure in axons," *Science* **339**(6118), 452–456 (2013).
42. A. H. Tang et al., "A trans-synaptic nanocolumn aligns neurotransmitter release to receptors," *Nature* **536**(7615), 210–214 (2016).
43. S. Hrabetova et al., "Unveiling the extracellular space of the brain: from super-resolved microstructure to in vivo function," *J. Neurosci.* **38**(44), 9355–9363 (2018).
44. F. Chen, P. W. Tillberg, and E. S. Boyden, "Expansion microscopy," *Science* **347**(6221), 543–548 (2015).
45. A. Klimas and Y. Zhao, "Expansion microscopy: toward nanoscale imaging of a diverse range of biomolecules," *ACS Nano* **14**(7), 7689–7695 (2020).
46. A. T. Wassie, Y. Zhao, and E. S. Boyden, "Expansion microscopy: principles and uses in biological research," *Nat. Methods* **16**(1), 33–41 (2019).
47. B. R. Gallagher and Y. Zhao, "Expansion microscopy: a powerful nanoscale imaging tool for neuroscientists," *Neurobiol. Dis.* **154**, 105362 (2021).
48. Y. X. Zhao et al., "Nanoscale imaging of clinical specimens using pathology-optimized expansion microscopy," *Nat. Biotechnol.* **35**(8), 757–764 (2017).
49. O. Bucur et al., "Nanoscale imaging of clinical specimens using conventional and rapid-expansion pathology," *Nat. Protoc.* **15**(5), 1649–1672 (2020).
50. F. Chen et al., "Nanoscale imaging of RNA with expansion microscopy," *Nat. Methods* **13**(8), 679–684 (2016).
51. T. J. Chozinski et al., "Expansion microscopy with conventional antibodies and fluorescent proteins," *Nat. Methods* **13**(6), 485–488 (2016).
52. S. Truckenbrodt et al., "X10 expansion microscopy enables 25-nm resolution on conventional microscopes," *Embo Rep.* **19**(9), e45836 (2018).
53. J. B. Chang et al., "Iterative expansion microscopy," *Nat. Methods* **14**(6), 593–599 (2017).
54. N. Jiang et al., "Superresolution imaging of Drosophila tissues using expansion microscopy," *Mol. Biol. Cell* **29**(12), 1413–1421 (2018).
55. T. J. Mosca et al., "Presynaptic LRP4 promotes synapse number and function of excitatory CNS neurons," *Elife* **6**, e27347 (2017).

56. C. C. Yu et al., "Expansion microscopy of C. elegans," *Elife* **9**, e46249 (2020).
57. I. E. Wang et al., "Hedgehog signaling regulates gene expression in planarian glia," *Elife* **5**, e16996 (2016).
58. L. Freifeld et al., "Expansion microscopy of zebrafish for neuroscience and developmental biology studies," *Proc. Natl. Acad. Sci. U. S. A.* **114**(50), E10799–E10808 (2017).
59. R. X. Gao et al., "Cortical column and whole-brain imaging with molecular contrast and nanoscale resolution," *Science* **363**(6424), 245 (2019).
60. J. R. Crittenden and A. M. Graybiel, "Disease-associated changes in the striosome and matrix compartments of the dorsal striatum," *HBK Behav. Neurosci.* **24**, 783–802 (2016).
61. A. L. Corner et al., "Increased expression of schizophrenia-associated gene C4 leads to hypoconnectivity of prefrontal cortex and reduced social interaction," *PLoS Biol.* **18**(1), e3000604 (2020).
62. J. A. Ortega et al., "Nucleocytoplasmic proteomic analysis uncovers eRF1 and nonsense-mediated decay as modifiers of ALS/FTD C9orf72 toxicity," *Neuron* **106**(1), 90–107.e13 (2020).
63. J. R. Crittenden et al., "Striosome-dendron bouquets highlight a unique striatonigral circuit targeting dopamine-containing neurons," *Proc. Natl. Acad. Sci. U. S. A.* **113**(40), 11318–11323 (2016).
64. L. Pesce et al., "Exploring the human cerebral cortex using confocal microscopy," *Prog. Biophys. Mol. Biol.* **168**, 3–9 (2022).
65. M. Marchetti et al., "Custom multiphoton/raman microscopy setup for imaging and characterization of biological samples," *Methods Protoc.* **2**(2), 51 (2019).
66. R. Cicchi et al., "From molecular structure to tissue architecture: collagen organization probed by SHG microscopy," *J. Biophotonics* **6**(2), 129–142 (2013).
67. G. Cox, "Biological applications of second harmonic imaging," *Biophys. Rev.* **3**(3), 131–141 (2011).
68. B. Weigelin, G. J. Bakker, and P. Friedl, "Third harmonic generation microscopy of cells and tissue organization," *J.Cell Sci.* **129**(2), 245–255 (2016).
69. M. Axer et al., "High-resolution fiber tract reconstruction in the human brain by means of three-dimensional polarized light imaging," *Front. Neuroinf.* **5**, 34 (2011).
70. M. Stacho et al., "A cortex-like canonical circuit in the avian forebrain," *Science* **369**(6511), eabc5534 (2020).
71. T. A.-O. Shaik et al., "Monitoring changes in biochemical and biomechanical properties of collagenous tissues using label-free and nondestructive optical imaging techniques," *Anal. Chem.* **93**(8), 3813–3821 (2021).
72. M. Wei et al., "Volumetric chemical imaging by clearing-enhanced stimulated Raman scattering microscopy," *Proc. Natl. Acad. Sci. U. S. A.* **116**(14), 6608 (2019).
73. L. Silvestri et al., "Universal autofocus for quantitative volumetric microscopy of whole mouse brains," *Nat. Methods* **18**(8), 953–958 (2021).
74. I. Costantini et al., "Large-scale, cell-resolution volumetric mapping allows layer-specific investigation of human brain cytoarchitecture," *Biomed. Opt. Express* **12**(6), 3684–3699 (2021).
75. D. Huang et al., "Optical coherence tomography," *Science* **254**(5035), 1178–1181 (1991).
76. C. Kut et al., "Detection of human brain cancer infiltration ex vivo and in vivo using quantitative optical coherence tomography," *Sci. Transl. Med.* **7**(292), 292ra100 (2015).
77. V. J. Srinivasan et al., "Optical coherence microscopy for deep tissue imaging of the cerebral cortex with intrinsic contrast," *Opt. Express* **20**(3), 2220–2239 (2012).
78. J. Ben Arous et al., "Single myelin fiber imaging in living rodents without labeling by deep optical coherence microscopy," *J. Biomed. Opt.* **16**(11), 116012 (2011).
79. P. J. Marchand et al., "Visible spectrum extended-focus optical coherence microscopy for label-free sub-cellular tomography," *Biomed. Opt. Express* **8**(7), 3343–3359 (2017).
80. V. J. Srinivasan et al., "Multiparametric, longitudinal optical coherence tomography imaging reveals acute injury and chronic recovery in experimental ischemic stroke," *PLOS ONE* **8**(8), e71478 (2013).

81. F. Li et al., "Nondestructive evaluation of progressive neuronal changes in organotypic rat hippocampal slice cultures using ultrahigh-resolution optical coherence microscopy," *Neurophotonics* **1**(2), 025002 (2014).

82. T. Bolmont et al., "Label-free imaging of cerebral β-amyloidosis with extended-focus optical coherence microscopy," *J. Neurosci.* **32**(42), 14548–14556 (2012).

83. J. Zhu et al., "1700 nm optical coherence microscopy enables minimally invasive, label-free, in vivo optical biopsy deep in the mouse brain," *Light Sci. Appl.* **10**(1), 145 (2021).

84. O. Assayag et al., "Imaging of non-tumorous and tumorous human brain tissues with full-field optical coherence tomography," *NeuroImage: Clin.* **2**, 549–557 (2013).

85. K. Bizheva et al., "Imaging ex vivo healthy and pathological human brain tissue with ultra-high-resolution optical coherence tomography," *J. Biomed. Opt.* **10**(1), 011006 (2007).

86. C. Magnain et al., "Blockface histology with optical coherence tomography: a comparison with Nissl staining," *Neuroimage* **84**, 524–533 (2014).

87. H. Wang et al., "Reconstructing micrometer-scale fiber pathways in the brain: multi-contrast optical coherence tomography based tractography," *Neuroimage* **58**(4), 984–992 (2011).

88. H. Wang et al., "Cross-validation of serial optical coherence scanning and diffusion tensor imaging: a study on neural fiber maps in human medulla oblongata," *Neuroimage* **100**, 395–404 (2014).

89. J. Lefebvre et al., "Whole mouse brain imaging using optical coherence tomography: reconstruction, normalization, segmentation, and comparison with diffusion MRI," *Neurophotonics* **4**(4), 041501 (2017).

90. A. Castonguay et al., "Comparing three-dimensional serial optical coherence tomography histology to MRI imaging in the entire mouse brain," *J. Biomed. Opt.* **23**(1), 016008 (2018).

91. C. J. Liu et al., "Visualizing and mapping the cerebellum with serial optical coherence scanner," *Neurophotonics* **4**(1), 011006 (2017).

92. T. Q. Li, C. J. Liu, and T. Akkin, "Contrast-enhanced serial optical coherence scanner with deep learning network reveals vasculature and white matter organization of mouse brain," *Neurophotonics* **6**(3), 035004 (2019).

93. C. J. Liu et al., "Polarization-sensitive optical coherence tomography reveals gray matter and white matter atrophy in SCA1 mouse models," *Neurobiol. Dis.* **116**, 69–77 (2018).

94. M. Inoue, "Genetically encoded calcium indicators to probe complex brain circuit dynamics in vivo," *Neurosci. Res.* **169**, 2–8 (2021).

95. D. Barson et al., "Simultaneous mesoscopic and two-photon imaging of neuronal activity in cortical circuits," *Nat. Methods* **17**(1), 107–113 (2020).

96. C. Lohr et al., "Using genetically encoded calcium indicators to study astrocyte physiology: a field guide," *Front. Cell Neurosci.* **15**, 690147 (2021).

97. L. B. Cohen, B. M. Salzberg, and A. Grinvald, "Optical methods for monitoring neuron activity," *Annu. Rev. Neurosci.* **1**, 171–182 (1978).

98. A. S. Abdelfattah et al., "Bright and photostable chemigenetic indicators for extended in vivo voltage imaging," *Science* **365**(6454), 699–704 (2019).

99. K. D. Piatkevich et al., "Population imaging of neural activity in awake behaving mice," *Nature* **574**(7778), 413–417 (2019).

100. V. Villette et al., "Ultrafast two-photon imaging of a high-gain voltage indicator in awake behaving mice," *Cell* **179**(7), 1590–1608.e23 (2019).

101. M. Kannan et al., "Fast, in vivo voltage imaging using a red fluorescent indicator," *Nat. Methods* **15**(12), 1108–1116 (2018).

102. R. U. Kulkarni et al., "In vivo two-photon voltage imaging with sulfonated rhodamine dyes," *ACS Cent. Sci.* **4**(10), 1371–1378 (2018).

103. A. Pal and L. Tian, "Imaging voltage and brain chemistry with genetically encoded sensors and modulators," *Curr. Opin. Chem. Biol.* **57**, 166–176 (2020).

104. R. U. Kulkarni and E. W. Miller, "Voltage imaging: pitfalls and potential," *Biochemistry* **56**(39), 5171–5177 (2017).

105. A. Andreoni, C. M. O. Davis, and L. Tian, "Measuring brain chemistry using genetically encoded fluorescent sensors," *Curr. Opin. Biomed. Eng.* **12**, 59–67 (2019).

106. S. J. Lee et al., "Cell-type-specific asynchronous modulation of PKA by dopamine in learning," *Nature* **590**(7846), 451–456 (2021).

107. Y. Oe et al., "Distinct temporal integration of noradrenaline signaling by astrocytic second messengers during vigilance," *Nat. Commun.* **11**, 471 (2020).

108. V. Augustine et al., "Temporally and spatially distinct thirst satiation signals," *Neuron* **103**(2), 242–249.e4 (2019).

109. A. Mohebi et al., "Dissociable dopamine dynamics for learning and motivation," *Nature* **570**(7759), 65–70 (2019).

110. J. W. de Jong et al., "A neural circuit mechanism for encoding aversive stimuli in the mesolimbic dopamine system," *Neuron* **101**(1), 133–151.e7 (2019).

111. J. E. Robinson et al., "Optical dopamine monitoring with dLight1 reveals mesolimbic phenotypes in a mouse model of neurofibromatosis type 1," *Elife* **8**, e48983 (2019).

112. H. Dong et al., "Dorsal striatum dopamine levels fluctuate across the sleep-wake cycle and respond to salient stimuli in mice," *Front. Neurosci.* **13**, 242 (2019).

113. B. Dai et al., "Dopamine release in nucleus accumbens core during social behaviors in mice," https://doi.org/10.1101/2021.06.22.449478 (2021).

114. E. F. Gallo et al., "Dopamine D2 receptors modulate the cholinergic pause and inhibitory learning," *Mol. Physchiatry* (2021).

115. C. Kjaerby et al., "Dynamic fluctuations of the locus coeruleus-norepinephrine system underlie sleep state transitions," https://doi.org/10.1101/2020.09.01.274977 (2020).

116. J. Sturgill et al., "Basal forebrain-derived acetylcholine encodes valence-free reinforcement prediction error," https://doi.org/10.1101/2020.02.17.953141 (2020).

117. S. Lohani et al., "Dual color mesoscopic imaging reveals spatiotemporally heterogeneous coordination of cholinergic and neocortical activity," https://doi.org/10.1101/2020.12.09.418632 (2020).

118. C. Iadecola, "The neurovascular unit coming of age: a journey through neurovascular coupling in health and disease," *Neuron* **96**(1), 17–42 (2017).

119. C. Eroglu and B. A. Barres, "Regulation of synaptic connectivity by glia," *Nature* **468**(7321), 223–231 (2010).

120. D. Koveal, C. M. Diaz-Garcia, and G. Yellen, "Fluorescent biosensors for neuronal metabolism and the challenges of quantitation," *Curr. Opin. Neurobiol.* **63**, 111–121 (2020).

121. L. F. Barros et al., "Current technical approaches to brain energy metabolism," *Glia* **66**(6), 1138–1159 (2018).

122. X. Yu, J. Nagai, and B. S. Khakh, "Improved tools to study astrocytes," *Nat. Rev. Neurosci.* **21**(3), 121–138 (2020).

123. D. F. Wilson et al., "Measuring oxygen in living tissue: intravascular, interstitial, and "tissue" oxygen measurements," *Adv. Exp. Med. Biol.* **701**, 53–59 (2011).

124. O. S. Finikova et al., "Oxygen microscopy by two-photon-excited phosphorescence," *Chemphyschem* **9**(12), 1673–1679 (2008).

125. T. V. Esipova et al., "Oxyphor 2P: a high-performance probe for deep-tissue longitudinal oxygen imaging," *Cell Metab.* **29**(3), 736–744.e7 (2019).

126. J. K. Tung et al., "Bioluminescence imaging in live cells and animals," *Neurophotonics* **3**(2), 025001 (2016).

127. S. Y. Park et al., "Novel luciferase-opsin combinations for improved luminopsins," *J. Neurosci. Res.* **98**(3), 410–421 (2020).

128. E. L. Crespo et al., "Bioluminescent optogenetics 2.0: harnessing bioluminescence to activate photosensory proteins in vitro and in vivo," *J. Vis. Exp.* **174**, e62850 (2021).

129. W. E. Medendorp et al., "Selective postnatal excitation of neocortical pyramidal neurons results in distinctive behavioral and circuit deficits in adulthood," *Iscience* **24**(3), 102157 (2021).

130. K. Deisseroth, "Optogenetics: 10 years of microbial opsins in neuroscience," *Nat. Neurosci.* **18**(9), 1213–1225 (2015).

131. E. S. Boyden et al., "Millisecond-timescale, genetically targeted optical control of neural activity," *Nat. Neurosci.* **8**(9), 1263–1268 (2005).

132. M. J. Berridge, M. D. Bootman, and H. L. Roderick, "Calcium signalling: dynamics, homeostasis and remodelling," *Nat. Rev. Mol. Cell. Biol.* **4**(7), 517–529 (2003).

133. M. E. Larkum et al., "Synaptically activated Ca2+ waves in layer 2/3 and layer 5 rat neo-cortical pyramidal neurons," *J. Physiol.* **549**(2), 471–488 (2003).

134. W. N. Ross et al., "Synaptically activated ca2+ release from internal stores in CNS neurons," *Cell Mol. Neurobiol.* **25**(2), 283–295 (2005).

135. R. J. Miller, "Multiple calcium channels and neuronal function," *Science* **235**(4784), 46–52 (1987).

136. F. Bezanilla, "Voltage-gated ion channels," *IEEE Trans. Nanobiosci.* **4**(1), 34–48 (2005).

137. R. Felix, "Molecular regulation of voltage-gated Ca2+ channels," *J. Recept. Signal Transduct. Res.* **25**(2), 57–71 (2005).

138. G. Grynkiewicz, M. Poenie, and R. Y. Tsien, "A new generation of Ca-2+ indicators with greatly improved fluorescence properties," *J. Biol. Chem.* **260**(6), 3440–3450 (1985).

139. R. Y. Tsien, "A non-disruptive technique for loading calcium buffers and indicators into cells," *Nature* **290**(5806), 527–528 (1981).

140. V. Levram and A. Grinvald, "Activity-dependent calcium transients in central-nervous-system myelinated axons revealed by the calcium indicator fura-2," *Biophys. J.* **52**(4), 571–576 (1987).

141. R. Yuste and L. C. Katz, "Control of postsynaptic Ca2+ influx in developing neocortex by excitatory and inhibitory neurotransmitters," *Neuron* **6**(3), 333–344 (1991).

142. O. Garaschuk, R. I. Milos, and A. Konnerth, "Targeted bulk-loading of fluorescent indicators for two-photon brain imaging in vivo," *Nat. Protoc.* **1**(1), 380–386 (2006).

143. O. Garaschuk et al., "Optical monitoring of brain function in vivo: from neurons to networks," *Pflugers Arch.* **453**(3), 385–396 (2006).

144. J. N. Kerr et al., "Spatial organization of neuronal population responses in layer 2/3 of rat barrel cortex," *J. Neurosci.* **27**(48), 13316–13328 (2007).

145. J. N. Kerr, D. Greenberg, and F. Helmchen, "Imaging input and output of neocortical networks in vivo," *Proc. Natl. Acad. Sci. U. S. A.* **102**(39), 14063–14068 (2005).

146. K. Ohki et al., "Functional imaging with cellular resolution reveals precise micro-architecture in visual cortex," *Nature* **433**(7026), 597–603 (2005).

147. T. R. Sato et al., "The functional microarchitecture of the mouse barrel cortex," *PLoS Biol.* **5**(7), e189 (2007).

148. M. R. Sullivan et al., "In vivo calcium imaging of circuit activity in cerebellar cortex," *J. Neurophysiol.* **94**(2), 1636–1644 (2005).

149. J. M. Wilson et al., "Two-photon calcium imaging of network activity in XFP-expressing neurons in the mouse," *J. Neurophysiol.* **97**(4), 3118–3125 (2007).

150. E. Chaigneau et al., "Two-photon imaging of capillary blood flow in olfactory bulb glomeruli," *Proc. Natl. Acad. Sci. U. S. A.* **100**(22), 13081–13086 (2003).

151. E. Chaigneau et al., "The relationship between blood flow and neuronal activity in the rodent olfactory bulb," *J. Neurosci.* **27**(24), 6452–6460 (2007).

152. A. Nimmerjahn et al., "Sulforhodamine 101 as a specific marker of astroglia in the neocortex in vivo," *Nat. Methods* **1**(1), 31–37 (2004).

153. X. Wang et al., "Astrocytic Ca(2+) signaling evoked by sensory stimulation in vivo," *Nat. Neurosci.* **9**(6), 816–823 (2006).

154. H. Hirase, "A multi-photon window onto neuronal-glial-vascular communication," *Trends Neurosci.* **28**(5), 217–219 (2005).

155. T. Takano et al., "Two-photon imaging of astrocytic Ca2+ signaling and the microvasculature in experimental mice models of Alzheimer's disease," *Ann. N. Y. Acad. Sci.* **1097**, 40–50 (2007).

156. G. F. Tian et al., "An astrocytic basis of epilepsy," *Nat. Med.* **11**(9), 973–981 (2005).

157. A. Miyawaki et al., "Fluorescent indicators for Ca2+ based on green fluorescent proteins and calmodulin," *Nature* **388**(6645), 882–887 (1997).

158. G. S. Baird, D. A. Zacharias, and R. Y. Tsien, "Circular permutation and receptor insertion within green fluorescent proteins," *Proc. Natl. Acad. Sci. U. S. A.* **96**(20), 11241–11246 (1999).

159. T. Nagai et al., "Circularly permuted green fluorescent proteins engineered to sense Ca2+," *Proc. Natl. Acad. Sci. U. S. A.* **98**(6), 3197–3202 (2001).

160. J. Nakai, M. Ohkura, and K. Imoto, "A high signal-to-noise Ca2+ probe composed of a single green fluorescent protein," *Nat. Biotechnol.* **19**(2), 137–141 (2001).
161. Y. Nasu et al., "Structure- and mechanism-guided design of single fluorescent protein-based biosensors," *Nat. Chem. Biol.* **17**(5), 509–518 (2021).
162. L. Tian et al., "Imaging neural activity in worms, flies and mice with improved GCaMP calcium indicators," *Nat. Methods* **6**(12), 875–881 (2009).
163. H. Dana et al., "High-performance calcium sensors for imaging activity in neuronal populations and microcompartments," *Nat. Methods* **16**(7), 649–657 (2019).
164. M. Inoue et al., "Rational engineering of XCaMPs, a multicolor GECI suite for in vivo imaging of complex brain circuit dynamics," *Cell* **177**(5), 1346–1360.e24 (2019).
165. L. Zarowny et al., "Bright and high-performance genetically encoded Ca2+ indicator based on mneongreen fluorescent protein," *ACS Sens.* **5**(7), 1959–1968 (2020).
166. O. M. Subach et al., "Novel genetically encoded bright positive calcium indicator NCaMP7 based on the mNeonGreen fluorescent protein," *Int. J. Mol. Sci.* **21**(5), 1644 (2020).
167. Y. X. Zhao et al., "An expanded palette of genetically encoded Ca2+ indicators," *Science* **333**(6051), 1888–1891 (2011).
168. H. Dana et al., "Sensitive red protein calcium indicators for imaging neural activity," *Elife* **5**, e12727 (2016).
169. Y. Shen et al., "A genetically encoded Ca2+ indicator based on circularly permutated sea anemone red fluorescent protein eqFP578," *BMC Biol.* **16**(1), 9 (2018).
170. Y. Qian et al., "Improved genetically encoded near-infrared fluorescent calcium ion indicators for in vivo imaging," *PLoS Biol.* **18**(11), e3000965 (2020).
171. Y. Qian et al., "A genetically encoded near-infrared fluorescent calcium ion indicator," *Nat. Methods* **16**(2), 171–174 (2019).
172. H. V. Davila et al., "A large change in axon fluorescence that provides a promising method for measuring membrane potential," *Nat. New Biol.* **241**(109), 159–160 (1973).
173. D. S. Peterka, H. Takahashi, and R. Yuste, "Imaging voltage in neurons," *Neuron* **69**(1), 9–21 (2011).
174. A. Grinvald and R. Hildesheim, "VSDI: a new era in functional imaging of cortical dynamics," *Nat. Rev. Neurosci.* **5**(11), 874–885 (2004).
175. A. P. de Silva et al., "New fluorescent model compounds for the study of photoinduced electron transfer: the influence of a molecular electric field in the excited state," *Angew. Chem. Int. Ed. Engl.* **34**(16), 1728–1731 (1995).
176. L.-S. Li, "Fluorescence probes for membrane potentials based on mesoscopic electron transfer," *Nano Lett.* **7**(10), 2981–2986 (2007).
177. E. W. Miller et al., "Optically monitoring voltage in neurons by photo-induced electron transfer through molecular wires," *Proc. Natl. Acad. Sci. U. S. A.* **109**(6), 2114–2119 (2012).
178. A. S. Walker et al., "Optical spike detection and connectivity analysis with a far-red voltage-sensitive fluorophore reveals changes to network connectivity in development and disease," *Front. Neurosci.* **15**, 643859 (2021).
179. P. Liu and E. W. Miller, "Electrophysiology, unplugged: imaging membrane potential with fluorescent indicators," *Acc. Chem. Res.* **53**(1), 11–19 (2020).
180. M. M. Milosevic et al., "In vitro testing of voltage indicators: Archon1, ArcLightD, ASAP1, ASAP2s, ASAP3b, Bongwoori-Pos6, BeRST1, FlicR1, and Chi-VSFP-butterfly," *eNeuro* **7**(5), ENEURO.0060-20.2020 (2020).
181. R. U. Kulkarni et al., "Voltage-sensitive rhodol with enhanced two-photon brightness," *Proc. Natl. Acad. Sci. U. S. A.* **114**(11), 2813–2818 (2017).
182. A. Kazemipour et al., "Kilohertz frame-rate two-photon tomography," *Nat. Methods* **16**(8), 778–786 (2019).
183. T. Fiala et al., "Chemical targeting of voltage sensitive dyes to specific cells and molecules in the brain," *J. Am. Chem. Soc.* **142**(20), 9285–9301 (2020).
184. S. Wakayama et al., "Chemical labelling for visualizing native AMPA receptors in live neurons," *Nat. Commun.* **8**, 14850 (2017).
185. E. D. Cosco et al., "Bright chromenylium polymethine dyes enable fast, four-color in vivo imaging with shortwave infrared detection," *J. Am. Chem. Soc.* **143**(18), 6836–6846 (2021).

186. S. S. Matikonda et al., "Core remodeling leads to long wavelength fluoro-coumarins," *Chem. Sci.* **11**(28), 7302–7307 (2020).
187. M. J. Hinner, G. Hübener, and P. Fromherz, "Genetic targeting of individual cells with a voltage-sensitive dye through enzymatic activation of membrane binding," *Chembiochem* **7**(3), 495–505 (2006).
188. D. N. Ng and P. Fromherz, "Genetic targeting of a voltage-sensitive dye by enzymatic activation of phosphonooxymethyl-ammonium derivative," *ACS Chem. Biol.* **6**(5), 444–451 (2011).
189. P. Liu et al., "Fluorogenic targeting of voltage-sensitive dyes to neurons," *J. Am. Chem. Soc.* **139**(48), 17334–17340 (2017).
190. G. Ortiz et al., "Synthesis of sulfonated carbofluoresceins for voltage imaging," *J. Am. Chem. Soc.* **141**(16), 6631–6638 (2019).
191. V. Grenier et al., "Spying on neuronal membrane potential with genetically targetable voltage indicators," *J. Am. Chem. Soc.* **141**(3), 1349–1358 (2019).
192. M. Sundukova et al., "A chemogenetic approach for the optical monitoring of voltage in neurons," *Angew. Chem. Int. Ed.* **58**(8), 2341–2344 (2019).
193. P. E. Deal et al., "Covalently tethered rhodamine voltage reporters for high speed functional imaging in brain tissue," *J. Am. Chem. Soc.* **142**(1), 614–622 (2020).
194. A. S. Abdelfattah et al., "A general approach to engineer positive-going eFRET voltage indicators," *Nat. Commun.* **11**(1), 3444 (2020).
195. C. Deo et al., "The HaloTag as a general scaffold for far-red tunable chemigenetic indicators," *Nat. Chem. Biol.* **17**(6), 718–723 (2021).
196. G. V. Los et al., "HaloTag: a novel protein labeling technology for cell imaging and protein analysis," *ACS Chem. Biol.* **3**(6), 373–382 (2008).
197. L. P. Encell et al., "Development of a dehalogenase-based protein fusion tag capable of rapid, selective and covalent attachment to customizable ligands," *Curr. Chem. Genom.* **6**, 55–71 (2012).
198. J. B. Grimm et al., "A general method to fine-tune fluorophores for live-cell and in vivo imaging," *Nat. Methods* **14**(10), 987–994 (2017).
199. Y. Gong et al., "High-speed recording of neural spikes in awake mice and flies with a fluorescent voltage sensor," *Science* **350**(6266), 1361–1366 (2015).
200. Y. Adam et al., "Voltage imaging and optogenetics reveal behaviour-dependent changes in hippocampal dynamics," *Nature* **569**(7756), 413–417 (2019).
201. L. Z. Fan et al., "All-optical electrophysiology reveals the role of lateral inhibition in sensory processing in cortical layer 1," *Cell* **180**(3), 521–535.e18 (2020).
202. M. Z. Lin and M. J. Schnitzer, "Genetically encoded indicators of neuronal activity," *Nat. Neurosci.* **19**(9), 1142–1153 (2016).
203. Y. Bando et al., "Genetic voltage indicators," *BMC Biol.* **17**(1), 71 (2019).
204. Y. Xu, P. Zou, and A. E. Cohen, "Voltage imaging with genetically encoded indicators," *Curr. Opin. Chem. Biol.* **39**, 1–10 (2017).
205. M. Kannan, G. Vasan, and V. A. Pieribone, "Optimizing strategies for developing genetically encoded voltage indicators," *Front. Cell Neurosci.* **13**, 53 (2019).
206. C. Beck, D. Zhang, and Y. Gong, "Enhanced genetically encoded voltage indicators advance their applications in neuroscience," *Curr. Opin. Biomed. Eng.* **12**, 111–117 (2019).
207. T. Knopfel and C. Song, "Optical voltage imaging in neurons: moving from technology development to practical tool," *Nat. Rev. Neurosci.* **20**(12), 719–727 (2019).
208. L. X. Peng, Y. X. Xu, and P. Zou, "Genetically-encoded voltage indicators," *Chin. Chem. Lett.* **28**(10), 1925–1928 (2017).
209. Y. Ma, P. O. Bayguinov, and M. B. Jackson, "Optical studies of action potential dynamics with hVOS probes," *Curr. Opin. Biomed. Eng.* **12**, 51–58 (2019).
210. T. Patriarchi et al., "Ultrafast neuronal imaging of dopamine dynamics with designed genetically encoded sensors," *Science* **360**(6396), eaat4422 (2018).
211. P. M. Borden et al., "A fast genetically encoded fluorescent sensor for faithful *in vivo* acetylcholine detection in mice, fish, worms and flies," https://doi.org/10.1101/2020.02.07.939504 (2020).

212. M. A. Lobas et al., "A genetically encoded single-wavelength sensor for imaging cytosolic and cell surface ATP," *Nat. Commun.* **10**, 711 (2019).
213. J. S. Marvin et al., "A genetically encoded fluorescent sensor for in vivo imaging of GABA," *Nat. Methods* **16**(8), 763–770 (2019).
214. A. V. Shivange et al., "Determining the pharmacokinetics of nicotinic drugs in the endoplasmic reticulum using biosensors," *J. Gen. Physiol.* **151**(6), 738–757 (2019).
215. E. K. Unger et al., "Directed evolution of a selective and sensitive serotonin sensor via machine learning," *Cell* **183**(7), 1986–2002.e26 (2020).
216. C. Hoffmann et al., "A FlAsH-based FRET approach to determine G protein-coupled receptor activation in living cells," *Nat. Methods* **2**(3), 171–176 (2005).
217. J. B. Jensen et al., "Fluorescence changes reveal kinetic steps of muscarinic receptor-mediated modulation of phosphoinositides and Kv7.2/7.3 K+ channels," *J. Gen. Physiol.* **133**(4), 347–359 (2009).
218. M. Maier-Peuschel et al., "A FRET-based M2 muscarinic receptor sensor to study the mechanisms of allosteric modulation," *N-S Arch. Pharmacol.* **377**, 15 (2008).
219. J. P. Vilardaga et al., "Measurement of the millisecond activation switch of G protein-coupled receptors in living cells," *Nat. Biotechnol.* **21**(7), 807–812 (2003).
220. N. R. Latorraca, A. J. Venkatakrishnan, and R. O. Dror, "GPCR dynamics: structures in motion," *Chem. Rev.* **117**(1), 139–155 (2017).
221. A. Dong et al., "A fluorescent sensor for spatiotemporally resolved endocannabinoid dynamics *in vitro* and *in vivo*," *Nat. Biotechnol.* (2021).
222. F. Sun et al., "A genetically encoded fluorescent sensor enables rapid and specific detection of dopamine in flies, fish, and mice," *Cell* **174**(2), 481–496.e19 (2018).
223. F. M. Sun et al., "Next-generation GRAB sensors for monitoring dopaminergic activity in vivo," *Nat. Methods* **17**(11), 1156–1166 (2020).
224. J. Feng et al., "A genetically encoded fluorescent sensor for rapid and specific in vivo detection of norepinephrine," *Neuron* **102**(4), 745–761.e8 (2019).
225. J. X. Wan et al., "A genetically encoded sensor for measuring serotonin dynamics," *Nat. Neurosci.* **24**(5), 746–752 (2021).
226. Z. Wu et al., "A GRAB sensor reveals activity-dependent non-vesicular somatodendritic adenosine release," https://doi.org/10.1101/2020.05.04.075564 (2020).
227. K. Deuschle et al., "Construction and optimization of a family of genetically encoded metabolite sensors by semirational protein engineering," *Protein Sci.* **14**(9), 2304–2314 (2005).
228. H. Takanaga, B. Chaudhuri, and W. B. Frommer, "GLUT1 and GLUT9 as major contributors to glucose influx in HepG2 cells identified by a high sensitivity intramolecular FRET glucose sensor," *BBA-Biomembr.* **1778**(4), 1091–1099 (2008).
229. C. M. Diaz-Garcia et al., "Quantitative in vivo imaging of neuronal glucose concentrations with a genetically encoded fluorescence lifetime sensor," *J. Neurosci. Res.* **97**(8), 946–960 (2019).
230. J. P. Keller et al., "In vivo glucose imaging in multiple model organisms with an engineered single-wavelength sensor," *Cell Rep.* **35**(12), 109284 (2021).
231. J. Berg, Y. P. Hung, and G. Yellen, "A genetically encoded fluorescent reporter of ATP:ADP ratio," *Nat. Methods* **6**(2), 161–166 (2009).
232. H. Imamura et al., "Visualization of ATP levels inside single living cells with fluorescence resonance energy transfer-based genetically encoded indicators," *Proc. Natl. Acad. Sci. U. S. A.* **106**(37), 15651–15656 (2009).
233. M. Tantama et al., "Imaging energy status in live cells with a fluorescent biosensor of the intracellular ATP-to-ADP ratio," *Nat. Commun.* **4**, 2550 (2013).
234. Y. P. Hung et al., "Imaging cytosolic NADH-NAD(+) redox state with a genetically encoded fluorescent biosensor," *Cell Metab.* **14**(4), 545–554 (2011).
235. Y. Zhao et al., "SoNar, a highly responsive NAD+/NADH sensor, allows high-throughput metabolic screening of anti-tumor agents," *Cell Metab.* **21**(5), 777–789 (2015).
236. R. Tao et al., "Genetically encoded fluorescent sensors reveal dynamic regulation of NADPH metabolism," *Nat. Methods* **14**(7), 720–728 (2017).

237. O. Sallin et al., "Semisynthetic biosensors for mapping cellular concentrations of nicotin-amide adenine dinucleotides," *Elife* **7**, e32638 (2018).

238. A. San Martin et al., "Imaging mitochondrial flux in single cells with a FRET sensor for pyruvate," *PLOS ONE* **9**(1), e85780 (2014).

239. A. San Martin et al., "A genetically encoded FRET lactate sensor and its use to detect the warburg effect in single cancer cells," *PLOS ONE* **8**(2), e57712 (2013).

240. P. Mächler et al., "*In vivo* evidence for a lactate gradient from astrocytes to neurons," *Cell Metab.* **23**(1), 94–102 (2016).

241. C. M. Diaz-Garcia et al., "Neuronal stimulation triggers neuronal glycolysis and not lactate uptake," *Cell Metab.* **26**(2), 361–374 (2017).

242. G. Yellen and R. Mongeon, "Quantitative two-photon imaging of fluorescent biosensors," *Curr. Opin. Chem. Biol.* **27**, 24–30 (2015).

243. N. J. Allen and D. A. Lyons, "Glia as architects of central nervous system formation and function," *Science* **362**(6411), 181–185 (2018).

244. W. S. Chung, N. J. Allen, and C. Eroglu, "Astrocytes control synapse formation, function, and elimination," *Cold Spring Harb. Perspect. Biol.* **7**(9), a020370 (2015).

245. D. Ziemens et al., "Heterogeneity of activity-induced sodium transients between astrocytes of the mouse hippocampus and neocortex: mechanisms and consequences," *J. Neurosci.* **39**(14), 2620–2634 (2019).

246. Y. Shen et al., "Genetically encoded fluorescent indicators for imaging intracellular potassium ion concentration," *Commun. Biol.* **2**, 18 (2019).

247. J. C. Octeau et al., "An optical neuron-astrocyte proximity assay at synaptic distance scales," *Neuron* **98**(1), 49–66.e9 (2018).

248. Y. Bernardinelli et al., "Activity-dependent structural plasticity of perisynaptic astro-cytic domains promotes excitatory synapse stability," *Curr. Biol.* **24**(15), 1679–1688 (2014).

249. C. Murphy-Royal et al., "Surface diffusion of astrocytic glutamate transporters shapes syn-aptic transmission," *Nat. Neurosci.* **18**(2), 219–226 (2015).

250. A. Araque et al., "Gliotransmitters travel in time and space," *Neuron* **81**(4), 728–739 (2014).

251. J. Nagai et al., "Specific and behaviorally consequential astrocyte Gq GPCR signaling attenuation *in vivo* with ibetaARK," *Neuron* **109**(14), 2256–2274.e9 (2021).

252. F. Pestana et al., "No longer underappreciated: the emerging concept of astrocyte hetero-geneity in neuroscience," *Brain Sci* **10**(3), 168 (2020).

253. L. Ben Haim and D. H. Rowitch, "Functional diversity of astrocytes in neural circuit regu-lation," *Nat. Rev. Neurosci.* **18**(1), 31–41 (2017).

254. M. Y. Batiuk et al., "Identification of region-specific astrocyte subtypes at single cell resolution," *Nat. Commun.* **11**, 1220 (2020).

255. L. Luo, E. M. Callaway, and K. Svoboda, "Genetic dissection of neural circuits: a decade of progress," *Neuron* **98**(2), 256–281 (2018).

256. X. Yu et al., "Reducing astrocyte calcium signaling *in vivo* alters striatal microcircuits and causes repetitive behavior," *Neuron* **99**(6), 1170–1187.e9 (2018).

257. S. Mederos et al., "Melanopsin for precise optogenetic activation of astrocyte-neuron networks," *Glia* **67**(5), 915–934 (2019).

258. J. C. Octeau et al., "Transient, consequential increases in extracellular potassium ions accompany Channelrhodopsin2 excitation," *Cell Rep.* **27**(8), 2249–2261.e7 (2019).

259. M. R. Depaoli et al., "Live cell imaging of signaling and metabolic activities," *Pharmacol. Ther.* **202**, 98–119 (2019).

260. X. Bi, C. Beck, and Y. Gong, "Genetically encoded fluorescent indicators for imaging brain chemistry," *Biosensors (Basel)* **11**(4), 116 (2021).

261. M. Slezak et al., "Distinct mechanisms for visual and motor-related astrocyte responses in mouse visual cortex," *Curr. Biol.* **29**(18), 3120–3127.e5 (2019).

262. N. A. Steinmetz et al., "Neuropixels 2.0: a miniaturized high-density probe for stable, long-term brain recordings," *Science* **372**(6539), eabf4588 (2021).

263. J. M. Vanderkooi et al., "An optical method for measurement of dioxygen concentration based on quenching of phosphorescence," *J. Biol. Chem.* **262**, 5476–5482 (1987).

264. W. L. Rumsey, J. M. Vanderkooi, and D. F. Wilson, "Imaging of phosphorescence: a novel method for measuring the distribution of oxygen in perfused tissue," *Science* **241**, 1649–1651 (1988).

265. S. A. Vinogradov and D. F. Wilson, "Porphyrin-dendrimers as biological oxygen sensors," in *Designing Dendrimers*, S. Capagna and P. Ceroni, Eds., Wiley, New York (2012).

266. A. Y. Lebedev et al., "Dendritic phosphorescent probes for oxygen imaging in biological systems," *ACS Appl. Mater. Interfaces* **1**(6), 1292–1304 (2009).

267. T. V. Esipova et al., "Two new "protected" oxyphors for biological oximetry: properties and application in tumor imaging," *Anal. Chem.* **83**(22), 8756–8765 (2011).

268. S. Sakadzic et al., "Two-photon high-resolution measurement of partial pressure of oxygen in cerebral vasculature and tissue," *Nat. Methods* **7**(9), 755–759 (2010).

269. J. Lecoq et al., "Simultaneous two-photon imaging of oxygen and blood flow in deep cerebral vessels," *Nat. Med.* **17**(7), 893–898 (2011).

270. A. Devor et al., ""Overshoot" of O(2) is required to maintain baseline tissue oxygenation at locations distal to blood vessels," *J. Neurosci.* **31**(38), 13676–13681 (2011).

271. S. M. S. Kazmi et al., "Three-dimensional mapping of oxygen tension in cortical arterioles before and after occlusion," *Biomed. Opt. Express* **4**(7), 1061–1073 (2013).

272. S. Sakadzic et al., "Large arteriolar component of oxygen delivery implies a safe margin of oxygen supply to cerebral tissue," *Nat. Commun.* **5**, 5734 (2014).

273. A. Parpaleix, Y. Goulam Houssen, and S. Charpak, "Imaging local neuronal activity by monitoring PO(2) transients in capillaries," *Nat. Med.* **19**(2), 241–246 (2013).

274. D. G. Lyons et al., "Mapping oxygen concentration in the awake mouse brain," *Elife* **5**, e12024 (2016).

275. R. P. Brinas et al., "Phosphorescent oxygen sensor with dendritic protection and two-photon absorbing antenna," *J. Am. Chem. Soc.* **127**(33), 11851–11862 (2005).

276. E. Roussakis et al., "Two-photon antenna-core oxygen probe with enhanced performance," *Anal. Chem.* **86**, 5937−5945 (2014).

277. T. V. Esipova et al., "Two-photon absorbing phosphorescent metalloporphyrins: effects of π-extension and peripheral substitution," *J. Am. Chem. Soc.* **138**(48), 15648–15662 (2016).

278. T. V. Esipova et al., "Stabilizing g-states in centrosymmetric tetrapyrroles: two-photon-absorbing porphyrins with bright phosphorescence," *J. Phys. Chem. A* **121**(33), 6243–6255 (2017).

279. X. Cao et al., "Quantification of oxygen depletion during FLASH irradiation in vitro and in vivo," *Int. J. Radiat. Oncol. Biol. Phys. (RED J.)* **111**(1), 240–248 (2021).

280. K. Berglund et al., "Light-emitting channelrhodopsins for combined optogenetic and chemical-genetic control of neurons," *PLOS ONE* **8**(3), e59759 (2013).

281. K. Berglund et al., "Luminopsins integrate opto- and chemogenetics by using physical and biological light sources for opsin activation," *Proc. Natl. Acad. Sci. U. S. A.* **113**(3), E358–E367 (2016).

282. N. Naim et al., "Luminescence-activated nucleotide cyclase regulates spatial and temporal cAMP synthesis," *J. Biol. Chem.* **294**(4), 1095–1103 (2019).

283. T. Li et al., "A synthetic BRET-based optogenetic device for pulsatile transgene expression enabling glucose homeostasis in mice," *Nat. Commun.* **12**, 615 (2021).

284. J. R. Zenchak et al., "Bioluminescence-driven optogenetic activation of transplanted neural precursor cells improves motor deficits in a Parkinson's disease mouse model," *J. Neurosci. Res.* **98**(3), 458–468 (2020).

285. J. K. Tung et al., "Chemically activated luminopsins allow optogenetic inhibition of distributed nodes in an epileptic network for non-invasive and multi-site suppression of seizure activity," *Neurobiol. Dis.* **109**, 1–10 (2018).

286. S. P. Yu et al., "Optochemogenetic stimulation of transplanted iPS-NPCs enhances neuronal repair and functional recovery after ischemic stroke," *J. Neurosci.* **39**(33), 6571–6594 (2019).

287. D. Song et al., "Manipulation of hippocampal CA3 firing via luminopsins modulates spatial and episodic short-term memory, especially working memory, but not long-term memory," *Neurobiol. Learn. Mem.* **155**, 435–445 (2018).

288. P. B. Jaiswal et al., "Motoneuron activity is required for enhancements in functional recovery after peripheral nerve injury in exercised female mice," *J. Neurosci. Res.* **98**(3), 448–457 (2020).

289. A. C. Love and J. A. Prescher, "Seeing (and using) the light: recent developments in bioluminescence technology," *Cell Chem. Biol.* **27**(8), 904–920 (2020).

290. D. Celinskis et al., "Miniaturized devices for bioluminescence imaging in freely behaving animals," *IEEE Eng. Med. Biol. Soc.* **2020**, 4385–4389 (2020).

291. G. Nagel et al., "Channelrhodopsin-1: a light-gated proton channel in green algae," *Science* **296**(5577), 2395–2398 (2002).

292. G. Nagel et al., "Channelrhodopsin-2, a directly light-gated cation-selective membrane channel," *Proc. Natl. Acad. Sci. U. S. A.* **100**(24), 13940–13945 (2003).

293. X. Li et al., "Fast noninvasive activation and inhibition of neural and network activity by vertebrate rhodopin and green algae channelrhodopsin," *Proc. Natl. Acad. Sci. U. S. A.* **102**(49), 17816–17821 (2005).

294. A. D. Bi et al., "Ectopic expression of a microbial-type rhodopsin restores visual responses in mice with photoreceptor degeneration," *Neuron* **50**(1), 23–33 (2006).

295. O. Yizhar et al., "Optogenetics in neural systems," *Neuron* **71**(1), 9–34 (2011).

296. K. Deisseroth and P. Hegemann, "The form and function of channelrhodopsin," *Science* **357**(6356), eaan5544 (2017).

297. J. Levitz et al., "Dual optical control and mechanistic insights into photoswitchable group II and III metabotropic glutamate receptors," *Proc. Natl. Acad. Sci. U. S. A.* **114**(17), E3546–E3554 (2017).

298. J. Levitz et al., "Optical control of metabotropic glutamate receptors," *Nat. Neurosci.* **16**(4), 507–516 (2013).

299. R. H. Kramer, A. Mourot, and H. Adesnik, "Optogenetic pharmacology for control of native neuronal signaling proteins," *Nat. Neurosci.* **16**(7), 816–823 (2013).

300. J. Y. Lin et al., "Optogenetic inhibition of synaptic release with chromophore-assisted light inactivation (CALI)," *Neuron* **79**(2), 241–253 (2013).

301. B. R. Rost et al., "Optogenetic tools for subcellular applications in neuroscience," *Neuron* **96**(3), 572–603 (2017).

302. L. Petreanu et al., "Channelrhodopsin-2-assisted circuit mapping of long-range callosal projections," *Nat. Neurosci.* **10**(5), 663–668 (2007).

303. D. Lin et al., "Functional identification of an aggression locus in the mouse hypothalamus," *Nature* **470**(7333), 221–226 (2011).

304. J. T. Paz et al., "Closed-loop optogenetic control of thalamus as a tool for interrupting seizures after cortical injury," *Nat. Neurosci.* **16**(1), 64–70 (2013).

305. J. A. Sahel et al., "Partial recovery of visual function in a blind patient after optogenetic therapy," *Nat. Med.* **27**(7), 1223–1229 (2021).

306. A. R. Adamantidis et al., "Neural substrates of awakening probed with optogenetic control of hypocretin neurons," *Nature* **450**(7168), 420–424 (2007).

307. M. Jazayeri and A. Afraz, "Navigating the neural space in search of the neural code," *Neuron* **93**(5), 1003–1014 (2017).

308. J. P. Rickgauer and D. W. Tank, "Two-photon excitation of channelrhodopsin-2 at saturation," *Proc. Natl. Acad. Sci. U. S. Am* **106**(35), 15025–15030 (2009).

309. R. Prakash et al., "Two-photon optogenetic toolbox for fast inhibition, excitation and bistable modulation," *Nat. Methods* **9**(12), 1171–1179 (2012).

310. A. M. Packer et al., "Two-photon optogenetics of dendritic spines and neural circuits," *Nat. Methods* **9**(12), 1202–1205 (2012).

311. E. Papagiakoumou, E. Ronzitti, and V. Emiliani, "Scanless two-photon excitation with temporal focusing," *Nat. Methods* **17**(6), 571–581 (2020).

312. W. J. Yang et al., "Simultaneous two-photon imaging and two-photon optogenetics of cortical circuits in three dimensions," *Elife* **7**, e32671 (2018).

313. N. T. M. Robinson et al., "Targeted activation of hippocampal place cells drives memory-guided spatial behavior," *Cell* **183**(6), 1586–1599.e10 (2020).

314. J. H. Marshel et al., "Cortical layer-specific critical dynamics triggering perception," *Science* **365**(6453), eaaw5202 (2019).

315. L. Carrillo-Reid et al., "Controlling visually guided behavior by holographic recalling of cortical ensembles," *Cell* **178**(2), 447–457.e5 (2019).
316. S. N. Chettih and C. D. Harvey, "Single-neuron perturbations reveal feature-specific competition in V1," *Nature* **567**(7748), 334–340 (2019).
317. O. P. Ernst et al., "Microbial and animal rhodopsins: structures, functions, and molecular mechanisms," *Chem. Rev.* **114**(1), 126–163 (2014).
318. N. Yutin and E. V. Koonin, "Proteorhodopsin genes in giant viruses," *Biol. Direct.* **7**, 34 (2012).
319. A. Rozenberg et al., "Microbial rhodopsins: the last two decades," *Annu. Rev. Microbiol.* **75**, 427–447 (2021).
320. G. Nagel et al., "Light activation of channelrhodopsin-2 in excitable cells of Caenorhabditis elegans triggers rapid Behavioral responses," *Curr. Biol.* **15**(24), 2279–2284 (2005).
321. J. Vierock et al., "Molecular determinants of proton selectivity and gating in the red-light activated channelrhodopsin Chrimson," *Sci. Rep.* **7**, 9928 (2017).
322. E. G. Govorunova et al., "Natural light-gated anion channels: a family of microbial rhodopsins for advanced optogenetics," *Science* **349**(6248), 647–650 (2015).
323. E. G. Govorunova et al., "The expanding family of natural anion channelrhodopsins reveals large variations in kinetics, conductance, and spectral sensitivity," *Sci. Rep.* **7**, 43358 (2017).
324. M. Mahn et al., "High-efficiency optogenetic silencing with soma-targeted anion-conducting channelrhodopsins," *Nat. Commun.* **9**, 4125 (2018).
325. J. E. Messier et al., "Targeting light-gated chloride channels to neuronal somatodendritic domain reduces their excitatory effect in the axon," *Elife* **7**, e38506 (2018).
326. R. A. Kopton et al., "Cardiac electrophysiological effects of light-activated chloride channels," *Front. Physiol.* **9**, 1806 (2018).
327. V. Shevchenko et al., "Inward H+ pump xenorhodopsin: mechanism and alternative optogenetic approach," *Sci. Adv.* **3**(9), e1603187 (2017).
328. J. Mattis et al., "Principles for applying optogenetic tools derived from direct comparative analysis of microbial opsins," *Nat. Methods* **9**(2), 159–172 (2012).
329. V. Gradinaru, K. R. Thompson, and K. Deisseroth, "eNpHR: a Natronomonas halorhodopsin enhanced for optogenetic applications," *Brain Cell Biol.* **36**(1–4), 129–139 (2008).
330. C. Grimm et al., "Electrical properties, substrate specificity and optogenetic potential of the engineered light-driven sodium pump eKR2," *Sci. Rep.* **8**, 9316 (2018).
331. V. Gradinaru et al., "Molecular and cellular approaches for diversifying and extending optogenetics," *Cell* **141**(1), 154–165 (2010).
332. J. A. Cardin et al., "Targeted optogenetic stimulation and recording of neurons in vivo using cell-type-specific expression of Channelrhodopsin-2," *Nat. Protoc.* **5**(2), 247–254 (2010).
333. E. G. Govorunova et al., "Cation and anion channelrhodopsins: sequence motifs and taxonomic distribution," *mBio* **12**(4), e0165621 (2021).
334. J. Wietek et al., "Conversion of channelrhodopsin into a light-gated chloride channel," *Science* **344**(6182), 409–412 (2014).
335. J. Y. Lin et al., "ReaChR: a red-shifted variant of channelrhodopsin enables deep transcranial optogenetic excitation," *Nat. Neurosci.* **16**(10), 1499–1508 (2013).
336. J. Wietek et al., "Anion-conducting channelrhodopsins with tuned spectra and modified kinetics engineered for optogenetic manipulation of behavior," *Sci. Rep.* **7**, 14957 (2017).
337. N. C. Klapoetke et al., "Independent optical excitation of distinct neural populations," *Nat. Methods* **11**(3), 338–346 (2014).
338. T. Mager et al., "High frequency neural spiking and auditory signaling by ultrafast red-shifted optogenetics," *Nat. Commun.* **9**, 1750 (2018).
339. K. Spoida et al., "Melanopsin variants as intrinsic optogenetic on and off switches for transient versus sustained activation of G protein pathways," *Curr. Biol.* **26**(9), 1206–1212 (2016).
340. D. Eickelbeck et al., "Lamprey parapinopsin ("UVLamP"): a bistable UV-sensitive optogenetic switch for ultrafast control of GPCR pathways," *Chembiochem* **21**(5), 612–617 (2020).

341. M. Mahn et al., "Efficient optogenetic silencing of neurotransmitter release with a mosquito rhodopsin," *Neuron* **109**(10), 1621–1635.e8 (2021).

342. B. A. Copits et al., "A photoswitchable GPCR-based opsin for presynaptic inhibition," *Neuron* **109**(11), 1791–1809.e11 (2021).

343. R. Karapinar et al., "Reverse optogenetics of G protein signaling by zebrafish non-visual opsin Opn7b for synchronization of neuronal networks," *Nat. Commun.* **12**, 4488 (2021).

344. S. P. Tsunoda, M. Sugiura, and H. Kandori, "Molecular properties and optogenetic applications of enzymerhodopsins," in *Optogenetics: Light-Sensing Proteins and Their Applications in Neuroscience and Beyond*, H. Yawo et al., Eds., Springer Nature, Singapore (2021).

345. M. Luck et al., "A photochromic Histidine Kinase Rhodopsin (HKR1) that is bimodally switched by ultraviolet and blue light," *J. Biol. Chem.* **287**(47), 40083–40090 (2012).

346. G. M. Avelar et al., "A rhodopsin-guanylyl cyclase gene fusion functions in visual perception in a fungus," *Curr. Biol.* **24**(11), 1234–1240 (2014).

347. K. Yoshida et al., "A unique choanoflagellate enzyme rhodopsin exhibits light-dependent cyclic nucleotide phosphodiesterase activity," *J. Biol. Chem.* **292**(18), 7531–7541 (2017).

348. Y. A. B. Sierra et al., "Potassium channel-based optogenetic silencing," *Nat. Commun.* **9**, 4611(2018).

349. S. X. Zhang et al., "Hypothalamic dopamine neurons motivate mating through persistent cAMP signalling," *Nature* **597**(7875), 245–249 (2021).

350. K. K. Ghosh et al., "Miniaturized integration of a fluorescence microscope," *Nat. Methods* **8**(10), 871–878 (2011).

351. D. Aharoni et al., "All the light that we can see: a new era in miniaturized microscopy," *Nat. Methods* **16**(1), 11–13 (2019).

352. D. Aharoni and T. M. Hoogland, "Circuit investigations with open-source miniaturized microscopes: past, present and future," *Front. Cell Neurosci.* **13**, 141 (2019).

353. N. Vladimirov et al., "Light-sheet functional imaging in fictively behaving zebrafish," *Nat. Methods* **11**(9), 883–884 (2014).

354. M. B. Bouchard et al., "Swept confocally-aligned planar excitation (SCAPE) microscopy for high-speed volumetric imaging of behaving organisms," *Nat. Photonics* **9**, 113–119 (2015).

355. V. Voleti et al., "Real-time volumetric microscopy of in vivo dynamics and large-scale samples with SCAPE 2.0," *Nat. Methods* **16**(10), 1054–1062 (2019).

356. L. N. Perkins et al., "Extracting individual neural activity recorded through splayed optical microfibers," *Neurophotonics* **5**(4), 045009 (2018).

357. F. Helmchen, A. Gilad, and J. L. Chen, "Neocortical dynamics during whisker-based sensory discrimination in head-restrained mice," *Neuroscience* **368**, 57–69 (2018).

358. A. Gilad and F. Helmchen, "Spatiotemporal refinement of signal flow through association cortex during learning," *Nat. Commun.* **11**, 1744 (2020).

359. A. Gilad et al., "Behavioral strategy determines frontal or posterior location of short-term memory in neocortex," *Neuron* **99**(4), 814–828.e7 (2018).

360. Y. Gallero-Salas et al., "Sensory and behavioral components of neocortical signal flow in discrimination tasks with short-term memory," *Neuron* **109**(1), 135–148.e6 (2021).

361. L. Pinto et al., "Task-dependent changes in the large-scale dynamics and necessity of cortical regions," *Neuron* **104**(4), 810–824.e9 (2019).

362. V. Esmaeili et al., "Rapid suppression and sustained activation of distinct cortical regions for a delayed sensory-triggered motor response," *Neuron* **109**(13), 2183–2201.e9 (2021).

363. Y. Ma et al., "Resting-state hemodynamics are spatiotemporally coupled to synchronized and symmetric neural activity in excitatory neurons," *Proc. Natl. Acad. Sci. U. S. A.* **113**(52), E8463–E8471 (2016).

364. A. Mitra et al., "Spontaneous infra-slow brain activity has unique spatiotemporal dynamics and laminar structure," *Neuron* **98**(2), 297–305.e6 (2018).

365. M. C. Murphy et al., "Macroscale variation in resting-state neuronal activity and connectivity assessed by simultaneous calcium imaging, hemodynamic imaging and electrophysiology," *Neuroimage* **169**, 352–362 (2018).

366. L. M. Brier et al., "Separability of calcium slow waves and functional connectivity during wake, sleep, and anesthesia," *Neurophotonics* **6**(3), 035002 (2019).

367. M. P. Vanni et al., "Mesoscale mapping of mouse cortex reveals frequency-dependent cycling between distinct macroscale functional modules," *J. Neurosci.* **37**(31), 7513–7533 (2017).

368. E. H. Ratzlaff and A. Grinvald, "A tandem-lens epifluorescence macroscope – hundred-fold brightness advantage for wide-field imaging," *J. Neurosci. Methods* **36**(2-3), 127–137 (1991).

369. J. Couto et al., "Chronic, cortex-wide imaging of specific cell populations during behavior," *Nat. Protoc.* **16**(7), 3241–3263 (2021).

370. M. P. Vanni and T. H. Murphy, "Mesoscale transcranial spontaneous activity mapping in GCaMP3 transgenic mice reveals extensive reciprocal connections between areas of somatomotor cortex," *J. Neurosci.* **34**(48), 15931–15946 (2014).

371. W. E. Allen et al., "Global representations of goal-directed behavior in distinct cell types of mouse neocortex," *Neuron* **94**(4), 891–907.e6 (2017).

372. N. A. Nelson et al., "Imaging spinal cord activity in behaving animals," *Exp. Neurol.* **320**, 112974 (2019).

373. S. Chen et al., "Miniature fluorescence microscopy for imaging brain activity in freely-behaving animals," *Neurosci. Bull.* **36**(10), 1182–1190 (2020).

374. T. Shuman et al., "Breakdown of spatial coding and interneuron synchronization in epileptic mice," *Nat. Neurosci.* **23**(2), 229–238 (2020).

375. B. B. Scott et al., "Imaging cortical dynamics in GCaMP transgenic rats with a head-mounted widefield macroscope," *Neuron* **100**(5), 1045–1058.e5 (2018).

376. M. L. Rynes et al., "Miniaturized head-mounted microscope for whole-cortex mesoscale imaging in freely behaving mice," *Nat. Methods* **18**, 417–425 (2021).

377. K. J. Sekiguchi et al., "Imaging large-scale cellular activity in spinal cord of freely behaving mice," *Nat. Commun.* **7**, 11450 (2016).

378. P. Shekhtmeyster et al., "Trans-segmental imaging in the spinal cord of behaving mice," bioRxiv, 2021.12.23.474042 (2021).

379. P. Shekhtmeyster et al., "Multiplex, translaminar imaging in the spinal cord of behaving mice," https://doi.org/10.1101/2021.12.23.474039 (2021).

380. C. Guo et al., "Miniscope-LFOV: a large field of view, single cell resolution, miniature microscope for wired and wire-free imaging of neural dynamics in freely behaving animals," https://doi.org/10.1101/2021.11.21.469394 (2021).

381. E. M. Hillman et al., "High-speed 3D imaging of cellular activity in the brain using axially-extended beams and light sheets," *Curr. Opin. Neurobiol.* **50**, 190–200 (2018).

382. K. H. Kim et al., "Multifocal multiphoton microscopy based on multianode photomultiplier tubes," *Opt. Express* **15**(18), 11658–11678 (2007).

383. Y. Xue et al., "Scanless volumetric imaging by selective access multifocal multiphoton microscopy," *Optica* **6**(1), 76–83 (2019).

384. R. Lu et al., "Video-rate volumetric functional imaging of the brain at synaptic resolution," *Nat. Neurosci.* **20**(4), 620–628 (2017).

385. P. Dufour et al., "Two-photon excitation fluorescence microscopy with a high depth of field using an axicon," *Appl. Opt.* **45**(36), 9246–9252 (2006).

386. A. Song et al., "Volumetric two-photon imaging of neurons using stereoscopy (vTwINS)," *Nat. Methods* **14**(4), 420–426 (2017).

387. F. F. Voigt et al., "The mesoSPIM initiative: open-source light-sheet microscopes for imaging cleared tissue," *Nat. Methods* **16**(11), 1105–1108 (2019).

388. H.-U. Dodt et al., "Ultramicroscopy: three-dimensional visualization of neuronal networks in the whole mouse brain," *Nat. Methods* **4**(4), 331–336 (2007).

389. J. Huisken et al., "Optical sectioning deep inside live embryos by selective plane illumination microscopy," *Science* **305**(5686), 1007–1009 (2004).

390. R. Tomer et al., "Quantitative high-speed imaging of entire developing embryos with simultaneous multiview light-sheet microscopy," *Nat. Methods* **9**(7), 755–763 (2012).

391. R. D. Vaadia et al., "Characterization of proprioceptive system dynamics in behaving drosophila larvae using high-speed volumetric microscopy," *Curr. Biol.* **29**(6), 935–944.e4 (2019).

392. E. S. Schaffer et al., "Flygenvectors: the spatial and temporal structure of neural activity across the fly brain," https://doi.org/10.1101/2021.09.25.461804 (2021).

393. C. Wen et al., "3DeeCellTracker, a deep learning-based pipeline for segmenting and tracking cells in 3D time lapse images," *Elife* **10**, e59187 (2021).

394. S. E. Benezra et al., "Learning enhances behaviorally relevant representations in apical dendrites," https://doi.org/10.1101/2021.11.10.468144 (2021).

395. L. Xu et al., "Widespread receptor-driven modulation in peripheral olfactory coding," *Science* **368**(6487), eaaz5390 (2020).

396. R. P. J. Barretto, B. Messerschmidt, and M. J. Schnitzer, "In vivo fluorescence imaging with high-resolution microlenses," *Nat. Methods* **6**(7), 511–512 (2009).

397. M. J. Levene et al., "In vivo multiphoton microscopy of deep brain tissue," *J. Neurophysiol.* **91**(4), 1908–1912 (2004).

398. M. L. Andermann et al., "Chronic cellular imaging of entire cortical columns in awake mice using microprisms," *Neuron* **80**(4), 900–913 (2013).

399. A. Antonini et al., "Extended field-of-view ultrathin microendoscopes for high-resolution two-photon imaging with minimal invasiveness," *Elife* **9**, e58882 (2020).

400. A. Attardo, J. E. Fitzgerald, and M. J. Schnitzer, "Impermanence of dendritic spines in live adult CA1 hippocampus," *Nature* **523**(7562), 592–596 (2015).

401. R. J. Low, Y. Gu, and D. W. Tank, "Cellular resolution optical access to brain regions in fissures: imaging medial prefrontal cortex and grid cells in entorhinal cortex," *Proc. Natl. Acad. Sci. U. S. A.* **111**(52), 18739–18744 (2014).

402. S. M. Popoff et al., "Measuring the transmission matrix in optics: an approach to the study and control of light propagation in disordered media," *Phys. Rev. Lett.* **104**(10), 100601 (2010).

403. S. Turtaev et al., "High-fidelity multimode fibre-based endoscopy for deep brain in vivo imaging," *Light-Sci. Appl.* **7**, 92 (2018).

404. S. A. Vasquez-Lopez et al., "Subcellular spatial resolution achieved for deep-brain imaging in vivo using a minimally invasive multimode fiber," *Light: Sci. Appl.* **7**(1), 110 (2018).

405. S. Ohayon et al., "Minimally invasive multimode optical fiber microendoscope for deep brain fluorescence imaging," *Biomed. Opt. Express* **9**(4), 1492–1509 (2018).

406. R. Turcotte et al., "Focusing light in biological tissue through a multimode optical fiber: refractive index matching," *Opt. Lett.* **44**(10), 2386–2389 (2019).

407. D. Kleinfeld et al., "Fluctuations and stimulus-induced changes in blood flow observed in individual capillaries in layers 2 through 4 of rat neocortex," *Proc. Natl. Acad. Sci. U. S. A.* **95**(26), 15741–15746 (1998).

408. N. J. Sofroniew et al., "A large field of view two-photon mesoscope with subcellular resolution for in vivo imaging," *Elife* **5**, e14472 (2016).

409. O. I. Rumyantsev et al., "Fundamental bounds on the fidelity of sensory cortical coding," *Nature* **580**(7801), 100–105 (2020).

410. C. H. Yu et al., "Diesel2p mesoscope with dual independent scan engines for flexible capture of dynamics in distributed neural circuitry," *Nat. Commun.* **12**, 6639 (2021).

411. M. K. Yang et al., "MATRIEX imaging: multiarea two-photon real-time in vivo explorer," *Light-Sci. Appl.* **8**, 109 (2019).

412. J. Lecoq et al., "Visualizing mammalian brain area interactions by dual-axis two-photon calcium imaging," *Nat. Neurosci.* **17**(12), 1825–1829 (2014).

413. M. J. Wagner et al., "Shared cortex-cerebellum dynamics in the execution and learning of a motor task," *Cell* **177**(3), 669–682.e24 (2019).

414. K. M. Nadella et al., "Random-access scanning microscopy for 3D imaging in awake behaving animals," *Nat. Methods* **13**(12), 1001–1004 (2016).

415. J. Demas et al., "High-speed, cortex-wide volumetric recording of neuroactivity at cellular resolution using light beads microscopy," *Nat. Methods* **18**(9), 1103–1111 (2021).

416. D. G. Ouzounov et al., "In vivo three-photon imaging of activity of GCaMP6-labeled neurons deep in intact mouse brain," *Nat. Methods* **14**(4), 388–390 (2017).

417. A. Klioutchnikov et al., "Three-photon head-mounted microscope for imaging deep cortical layers in freely moving rats," *Nat. Methods* **17**(5), 509–513 (2020).

418. W. Zong et al., "Miniature two-photon microscopy for enlarged field-of-view, multi-plane and long-term brain imaging," *Nat. Methods* **18**(1), 46–49 (2021).

419. Y. J. Xue et al., "Single-shot 3D wide-field fluorescence imaging with a computational miniature mesoscope," *Sci. Adv.* **6**(43), eabb7508 (2020).

420. F. Tian, J. J. Hu, and W. J. Yang, "GEOMScope: large field-of-view 3d lensless microscopy with low computational complexity," *Laser Photonics Rev.* **15**(8), 2100072 (2021).

421. P. F. Qiao, W. J. Yang, and C. J. Chang-Hasnain, "Recent advances in high-contrast meta-structures, metasurfaces, and photonic crystals," *Adv. Opt. Photonics* **10**(1), 180–245 (2018).

422. J. N. Stirman et al., "Wide field-of-view, multi-region, two-photon imaging of neuronal activity in the mammalian brain," *Nat. Biotechnol.* **34**(8), 857–862 (2016).

423. K. Ota et al., "Fast, cell-resolution, contiguous-wide two-photon imaging to reveal functional network architectures across multi-modal cortical areas," *Neuron* **109**(11), 1810–1824.e9 (2021).

424. A. Cheng et al., "Simultaneous two-photon calcium imaging at different depths with spatiotemporal multiplexing," *Nat. Methods* **8**(2), 139–142 (2011).

425. S. Weisenburger et al., "Volumetric Ca2+ imaging in the mouse brain using hybrid multiplexed sculpted light microscopy," *Cell* **177**(4), 1050–1066.e14 (2019).

426. R. W. Lu et al., "Rapid mesoscale volumetric imaging of neural activity with synaptic resolution," *Nat. Methods* **17**(3), 291–294 (2020).

427. M. Clough et al., "Flexible simultaneous mesoscale two-photon imaging of neural activity at high speeds," *Nat. Commun.* **12**, 6638 (2021).

428. W. Denk, J. H. Strickler, and W. W. Webb, "Two-photon laser scanning fluorescence microscopy," *Science* **248**(4951), 73–76 (1990).

429. T. V. Truong et al., "Deep and fast live imaging with two-photon scanned light-sheet microscopy," *Nat. Methods* **8**(9), 757–760 (2011).

430. R. W. Lu et al., "Video-rate volumetric functional imaging of the brain at synaptic resolution," *Nat. Neurosci.* **20**(4), 620–628 (2017).

431. R. Prevedel et al., "Fast volumetric calcium imaging across multiple cortical layers using sculpted light," *Nat. Methods* **13**(12), 1021–1028 (2016).

432. W. J. Yang et al., "Simultaneous multi-plane imaging of neural circuits," *Neuron* **89**(2), 269–284 (2016).

433. T. Zhang et al., "Kilohertz two-photon brain imaging in awake mice," *Nat. Methods* **16**(11), 1119–1122 (2019).

434. D. R. Beaulieu et al., "Simultaneous multiplane imaging with reverberation two-photon microscopy," *Nat. Methods* **17**(3), 283 (2020).

435. J. L. Wu et al., "Kilohertz two-photon fluorescence microscopy imaging of neural activity in vivo," *Nat. Methods* **17**(3), 287–290 (2020).

436. G. D. Reddy et al., "Three-dimensional random access multiphoton microscopy for functional imaging of neuronal activity," *Nat. Neuroscie.* **11**(6), 713–720 (2008).

437. M. Ducros et al., "Encoded multisite two-photon microscopy," *Proc. Natl. Acad. Sci. U. S. A.* **110**(32), 13138–13143 (2013).

438. D. Oron, E. Tal, and Y. Silberberg, "Scanningless depth-resolved microscopy," *Opt. Express* **13**(5), 1468–1476 (2005).

439. G. H. Zhu et al., "Simultaneous spatial and temporal focusing of femtosecond pulses," *Opt. Express* **13**(6), 2153–2159 (2005).

440. M. Kumar et al., "Integrated one- and two-photon scanned oblique plane illumination (SOPi) microscopy for rapid volumetric imaging," *Opt. Express* **26**(10), 13027–13041 (2018).

441. S. Quirin et al., "Simultaneous imaging of neural activity in three dimensions," *Front. Neural Circuit* **8**, 29 (2014).

442. R. Prevedel et al., "Simultaneous whole-animal 3D imaging of neuronal activity using light-field microscopy," *Nat. Methods* **11**(7), 727–730 (2014).

443. M. Broxton et al., "Wave optics theory and 3-D deconvolution for the light field microscope," *Opt. Express* **21**(21), 25418–25439 (2013).

444. G. Y. Fan et al., "Video-rate scanning two-photon excitation fluorescence microscopy and ratio imaging with cameleons," *Biophys. J.* **76**(5), 2412–2420 (1999).

445. R. Salome et al., "Ultrafast random-access scanning in two-photon microscopy using acousto-optic deflectors," *J. Neurosci. Methods* **154**(1–2), 161–174 (2006).

446. G. D. Reddy and P. Saggau, "Fast three-dimensional laser scanning scheme using acousto-optic deflectors," *J. Biomed. Opt.* **10**(6), 064038 (2005).

447. W. J. Shain et al., "Extended depth-of-field microscopy with a high-speed deformable mirror," *Opt. Lett.* **42**(5), 995–998 (2017).

448. M. Dal Maschio et al., "Three-dimensional in vivo scanning microscopy with inertia-free focus control," *Opt. Lett.* **36**(17), 3503–3505 (2011).

449. V. Nikolenko et al., "SLM microscopy: scanless two-photon imaging and photostimulation with spatial light modulators," *Front. Neural Circuit* **2**, 5 (2008).

450. W. Gobel, B. M. Kampa, and F. Helmchen, "Imaging cellular network dynamics in three dimensions using fast 3D laser scanning," *Nat. Methods* **4**(1), 73–79 (2007).

451. B. F. Grewe et al., "Fast two-layer two-photon imaging of neuronal cell populations using an electrically tunable lens," *Biomed. Opt. Express* **2**(7), 2035–2046 (2011).

452. L. J. Kong et al., "Continuous volumetric imaging via an optical phase-locked ultrasound lens," *Nat. Methods* **12**(8), 759–762 (2015).

453. T. Chakraborty et al., "Converting lateral scanning into axial focusing to speed up 3D microscopy," *Light Sci. Appl.* **9**, 165 (2020).

454. M. Bawart et al., "Modified Alvarez lens for high-speed focusing," *Opt. Express* **25**(24), 29847–29855 (2017).

455. P. A. Kirkby, K. M. Srinivas Nadella, and R. A. Silver, "A compact acousto-optic lens for 2D and 3D femtosecond based 2-photon microscopy," *Opt. Express* **18**(13), 13720–13745 (2010).

456. R. W. Lu et al., "50 Hz volumetric functional imaging with continuously adjustable depth of focus," *Biomed. Opt. Express* **9**(4), 1964–1976 (2018).

457. G. H. Meng et al., "High-throughput synapse-resolving two-photon fluorescence micro-endoscopy for deep-brain volumetric imaging in vivo," *Elife* **8**, e40805 (2019).

458. S. Bovetti et al., "Simultaneous high-speed imaging and optogenetic inhibition in the intact mouse brain," *Sci. Rep.* **7**, 40041 (2017).

459. F. Anselmi et al., "Three-dimensional imaging and photostimulation by remote-focusing and holographic light patterning," *Proc. Natl. Acad. Sci. U. S. A.* **108**(49), 19504–19509 (2011).

460. C. Moretti et al., "Scanless functional imaging of hippocampal networks using patterned two-photon illumination through GRIN lenses," *Biomed. Opt. Express* **7**(10), 3958–3967 (2016).

461. M. Duocastella et al., "Acousto-optic systems for advanced microscopy," *J. Phys.: Photonics* **3**, 012004 (2021).

462. V. A. Griffiths et al., "Real-time 3D movement correction for two-photon imaging in behaving animals," *Nat. Methods* **17**(7), 741–748 (2020).

463. T. Fernandez-Alfonso et al., "Monitoring synaptic and neuronal activity in 3D with synthetic and genetic indicators using a compact acousto-optic lens two-photon microscope," *J. Neurosci. Methods* **222**, 69–81 (2014).

464. A. Kaplan, N. Friedman, and N. Davidson, "Acousto-optic lens with very fast focus scanning," *Opt. Lett.* **26**(14), 1078–1080 (2001).

465. H. Gurnani and R. A. Silver, "Multidimensional population activity in an electrically coupled inhibitory circuit in the cerebellar cortex," *Neuron* **109**(10), 1739–1753.e8 (2021).

466. G. Szalay et al., "Fast 3D imaging of spine, dendritic, and neuronal assemblies in behaving animals," *Neuron* **92**(4), 723–738 (2016).

467. G. Konstantinou et al., "Dynamic wavefront shaping with an acousto-optic lens for laser scanning microscopy," *Opt. Express* **24**(6), 6283–6299 (2016).

468. E. Froudarakis et al., "Population code in mouse V1 facilitates readout of natural scenes through increased sparseness," *Nat. Neurosci.* **17**(6), 851–857 (2014).

469. G. Katona et al., "Fast two-photon in vivo imaging with three-dimensional random-access scanning in large tissue volumes," *Nat. Methods* **9**(2), 201–208 (2012).

470. T. Geiller et al., "Large-scale 3D two-photon imaging of molecularly identified CA1 inter-neuron dynamics in behaving mice," *Neuron* **108**(5), 968–983.e9 (2020).

471. F. Lanore et al., "Cerebellar granule cell axons support high dimensional representations," *Nat. Neurosci.* **24**(8), 1142–1150 (2021).

472. W. Akemann et al., "Fast spatial beam shaping by acousto-optic diffraction for 3D non-linear microscopy," *Opt. Express* **23**(22), 28191–205 (2015).

473. P. Mahou et al., "Multicolor two-photon tissue imaging by wavelength mixing," *Nat. Methods* **9**(8), 815–818 (2012).

474. J. R. Lakowicz et al., "Two-color two-photon excitation of fluorescence," *Photochem. Photobiol.* **64**(4), 632–635 (1996).

475. M. W. Dowley, K. B. Eisenthal, and W. L. Peticolas, "Two-photon laser excitation of poly-cyclic aromatic molecules," *J. Chem. Phys.* **47**(5), 1609–1619 (1967).

476. P. R. Monson and W. M. Mcclain, "Polarization dependence of the two-photon absorption of tumbling molecules with application to liquid 1-chloronaphthalene and benzene," *J. Chem. Phys.* **53**(1), 29–37 (1970).

477. D. Frohlich and H. Mahr, "Two-photon spectroscopy in anthracene," *Phys. Rev. Lett.* **16**(20), 895–897 (1966).

478. S. Sadegh et al., "Overcoming the fundamental limit of two-photon microscopywith non-degenerate excitation," in *Biophotonics Congr.: Biomed. Opt. 2020 (Transl., Microsc., OCT, OTS, BRAIN), OSA Tech. Digest*, Optica Publishing Group, p. BTu1C.4 (2020).

479. S. Sadegh et al., "Measurement of the relative non-degenerate two-photon absorption cross-section for fluorescence microscopy," *Opt. Express* **27**(6), 8335–8347 (2019).

480. S. Sadegh et al., "Efficient non-degenerate two-photon excitation for fluorescence micros-copy," *Opt. Express* **27**(20), 28022–28035 (2019).

481. M. H. Yang et al., "Non-degenerate 2-photon excitation in scattering medium for fluores-cence microscopy," *Opt. Express* **24**(26), 30173–30187 (2016).

482. J. M. Hales et al., "Resonant enhancement of two-photon absorption in substituted fluorene molecules," *J. Chem. Phys.* **121**(7), 3152–3160 (2004).

483. S. Quentmeier, S. Denicke, and K. H. Gericke, "Two-color two-photon fluorescence laser scanning microscopy," *J. Fluoresc.* **19**(6), 1037–1043 (2009).

484. E. P. Perillo et al., "Two-color multiphoton in vivo imaging with a femtosecond diamond Raman laser," *Light-Sci. Appl.* **6**, e17095 (2017).

485. S. Lindek and E. H. Stelzer, "Resolution improvement by nonconfocal theta microscopy," *Opt. Lett.* **24**(21), 1505–1507 (1999).

486. C. Ibanez-Lopez et al., "Optical-sectioning improvement in two-color excitation scanning microscopy," *Microsc. Res. Tech.* **64**(2), 96–102 (2004).

487. D. R. Miller et al., "Deep tissue imaging with multiphoton fluorescence microscopy," *Curr. Opin. Biomed. Eng.* **4**, 32–39 (2017).

488. C. Wang et al., "Reduced deep-tissue image degradation in three-dimensional multiphoton microscopy with concentric two-color two-photon fluorescence excitation," *J. Opt. Soc. Am. B* **25**(6), 976–982 (2008).

489. M. O. Cambaliza and C. Saloma, "Advantages of two-color excitation fluorescence microscopy with two confocal excitation beams," *Opt. Commun.* **184**(1-4), 25–35 (2000).

490. C. M. Blanca and C. Saloma, "Two-color excitation fluorescence microscopy through highly scattering media," *Appl. Opt.* **40**(16), 2722–2729 (2001).

491. D. Kobat, G. Zhu, and C. Xu, "Background reduction with two-color two-beam multipho-ton excitation," in *Biomed. Opt., OSA Tech. Digest (CD)*, Optica Publishing Group, p. BMF6 (2008).

492. X. Cheng et al., "Comparing the fundamental imaging depth limit of two-photon, three-photon, and non-degenerate two-photon microscopy," *Opt. Lett.* **45**(10), 2934–2937 (2020).

493. T.-W. Chen et al., "Ultrasensitive fluorescent proteins for imaging neuronal activity," *Nature* **499**(7458), 295–300 (2013).

494. P. Theer and W. Denk, "On the fundamental imaging-depth limit in two-photon micros-copy," *J. Opt. Soc. Am. A Opt. Image Sci. Vision* **23**(12), 3139–3149 (2006).

495. T. Wang et al., "Three-photon imaging of mouse brain structure and function through the intact skull," *Nat. Methods* **15**(10), 789–792 (2018).

496. H. Liu et al., "In vivo deep-brain structural and hemodynamic multiphoton microscopy enabled by quantum dots," *Nano Lett.* **19**(8), 5260–5265 (2019).

497. N. G. Horton et al., "In vivo three-photon microscopy of subcortical structures within an intact mouse brain," *Nat. Photonics* **7**, 205–209 (2013).

498. D. Kobat et al., "Deep tissue multiphoton microscopy using longer wavelength excitation," *Opt. Express* **17**(16), 13354–13364 (2009).

499. M. Wang et al., "Comparing the effective attenuation lengths for long wavelength in vivo imaging of the mouse brain," *Biomed. Opt. Express* **9**(8), 3534–3543 (2018).

500. K. Takasaki, R. Abbasi-asl, and J. Waters, "Superficial bound of the depth limit of two-photon imaging in mouse brain," *eNeuro* **7**(1), ENEURO.0255-19.2019 (2020).

501. T. Wang et al., "Quantitative analysis of 1300-nm three-photon calcium imaging in the mouse brain," *eLife* **9**, e53205 (2020).

502. D. M. Chow et al., "Deep three-photon imaging of the brain in intact adult zebrafish," *Nat. Methods* **17**, 605–608 (2020).

503. Y. Hontani, F. Xia, and C. Xu, "Multicolor three-photon fluorescence imaging with single-wavelength excitation deep in mouse brain," *Sci. Adv.* **7**, eabf3531 (2021).

504. C. Xu et al., "Multiphoton fluorescence excitation: new spectral windows for biological nonlinear microscopy," *Proc. Natl. Acad. Sci. U. S. A.* **93**(20), 10763–10768 (1996).

505. C. Xu and W. W. Webb, "Multiphoton excitation of molecular fluorophores and nonlinear laser microscopy," *Top. Fluoresc. Spectrosc.* **5**, 471–540 (1997).

506. N. Akbari et al., "Imaging deeper than the transport mean free path with multiphoton microscopy," *Biomed. Opt. Express* **13**(1), 452–463 (2022).

507. L. Streich et al., "High-resolution structural and functional deep brain imaging using adaptive optics three-photon microscopy," *Nat. Methods* **18**(10), 1253–1258 (2021).

508. C. Rodríguez et al., "An adaptive optics module for deep tissue multiphoton imaging in vivo," *Nat. Methods* **18**(10), 1259–1264 (2021).

509. B. Li et al., "An adaptive excitation source for high-speed multiphoton microscopy," *Nat. Methods* **17**, 163–166 (2020).

510. M. Wang et al., "Impact of the emission wavelengths on in vivo multiphoton imaging of mouse brains," *Biomed. Opt. Express* **10**(4), 1905–1918 (2019).

511. H. W. Babcock, "The Possibility of compensating astronomical seeing," *Publ. Astron. Soc. Pac.* **65**, 229 (1953).

512. R. K. Tyson, *Principles of Adaptive Optics*, CRC Press (2015).

513. J. Z. Liang, D. R. Williams, and D. T. Miller, "Supernormal vision and high-resolution retinal imaging through adaptive optics," *J. Opt. Soc. Am. A* **14**(11), 2884–2892 (1997).

514. J. Porter et al., *Adaptive Optics for Vision Science: Principles, Practices, Design and Applications*, Wiley (2006).

515. C. Rodriguez and N. Ji, "Adaptive optical microscopy for neurobiology," *Curr. Opin. Neurobiol.* **50**, 83–91 (2018).

516. R. Aviles-Espinosa et al., "Measurement and correction of in vivo sample aberrations employing a nonlinear guide-star in two-photon excited fluorescence microscopy," *Biomed. Opt. Express* **2**(11), 3135–3149 (2011).

517. K. Wang et al., "Rapid adaptive optical recovery of optimal resolution over large volumes," *Nat. Methods* **11**(6), 625–628 (2014).

518. D. Debarre et al., "Image-based adaptive optics for two-photon microscopy," *Opt. Lett.* **34**(16), 2495–2497 (2009).

519. N. Ji, D. E. Milkie, and E. Betzig, "Adaptive optics via pupil segmentation for high-resolution imaging in biological tissues," *Nat. Methods* **7**(2), 141–147 (2010).

520. C. Wang et al., "Multiplexed aberration measurement for deep tissue imaging in vivo," *Nat. Methods* **11**(10), 1037–1040 (2014).

521. I. N. Papadopoulos et al., "Scattering compensation by focus scanning holographic aberration probing (F-SHARP)," *Nat. Photonics* **11**(2), 116–123 (2017).

522. K. Wang et al., "Direct wavefront sensing for high-resolution in vivo imaging in scattering tissue," *Nat. Commun.* **6**, 7276 (2015).

523. R. Liu et al., "Direct wavefront sensing enables functional imaging of infragranular axons and spines," *Nat. Methods* **16**, 615–618 (2019).

524. N. Jia, T. R. Sato, and E. Betzig, "Characterization and adaptive optical correction of aberrations during in vivo imaging in the mouse cortex," *Proc. Natl. Acad. Sci. U. S. A.* **109**(1), 22–27 (2012).

525. X. D. Tao et al., "Transcutical imaging with cellular and subcellular resolution," *Biomed. Opt. Express* **8**(3), 1277–1289 (2017).
526. J. H. Park et al., "Large-field-of-view imaging by multi-pupil adaptive optics," *Nat. Methods* **14**(6), 581–583 (2017).
527. I. N. Papadopoulos et al., "Dynamic conjugate F-SHARP microscopy," *Light-Sci. Appl.* **9**, 110 (2020).
528. W. Z. Sun et al., "Thalamus provides layer 4 of primary visual cortex with orientation- and direction-tuned inputs," *Nat. Neurosci.* **19**(2), 308–315 (2016).
529. I. W. Chen, E. Papagiakoumou, and V. Emiliani, "Towards circuit optogenetics," *Curr. Opin. Neurobiol.* **50**, 179–189 (2018).
530. V. Emiliani et al., "All-Optical interrogation of neural circuits," *J. Neurosci.* **35**(41), 13917–13926 (2015).
531. H. Adesnik and L. Abdeladim, "Probing neural codes with two-photon holographic opto-genetics," *Nat. Neurosci.* **24**(10), 1356–1366 (2021).
532. A. M. Packer et al., "Simultaneous all-optical manipulation and recording of neural circuit activity with cellular resolution in vivo," *Nat. Methods* **12**(2), 140–146 (2015).
533. O. A. Shemesh et al., "Temporally precise single-cell-resolution optogenetics," *Nat. Neurosci.* **20**(12), 1796–1806 (2017).
534. A. Forli et al., "Two-photon bidirectional control and imaging of neuronal excitability with high spatial resolution in vivo," *Cell Rep.* **22**(11), 3087–3098 (2018).
535. A. R. Mardinly et al., "Precise multimodal optical control of neural ensemble activity," *Nat. Neurosci.* **21**(6), 881–893 (2018).
536. W. Yang et al., "Simultaneous two-photon imaging and two-photon optogenetics of cortical circuits in three dimensions," *Elife* **7**, e32671 (2018).
537. M. Dal Maschio et al., "Linking neurons to network function and behavior by two-photon holographic optogenetics and volumetric imaging," *Neuron* **94**(4), 774–789.e5 (2017).
538. J. V. Gill et al., "Precise holographic manipulation of olfactory circuits reveals coding features determining perceptual detection," *Neuron* **108**(2), 382–393.e5 (2020).
539. J. P. Rickgauer, K. Deisseroth, and D. W. Tank, "Simultaneous cellular-resolution optical perturbation and imaging of place cell firing fields," *Nat. Neurosci.* **17**(12), 1816–1824 (2014).
540. E. Papagiakoumou et al., "Patterned two-photon illumination by spatiotemporal shaping of ultrashort pulses," *Opt. Express* **16**(26), 22039–22047 (2008).
541. L. Golan et al., "Design and characteristics of holographic neural photo-stimulation systems," *J. Neural Eng.* **6**(6), 066004 (2009).
542. N. C. Pégard et al., "Three-dimensional scanless holographic optogenetics with temporal focusing (3D-SHOT)," *Nat. Commun.* **8**, 1228 (2017).
543. N. Accanto et al., "Multiplexed temporally focused light shaping through a gradient index lens for precise in-depth optogenetic photostimulation," *Sci. Rep.* **9**, 7603 (2019).
544. E. Papagiakoumou et al., "Scanless two-photon excitation of channelrhodopsin-2," *Nat. Methods* **7**(10), 848–854 (2010).
545. S. Paluch-Siegler et al., "All-optical bidirectional neural interfacing using hybrid multi-photon holographic optogenetic stimulation," *Neurophotonics* **2**(3), 031208 (2015).
546. I. W. Chen et al., "In vivo submillisecond two-photon optogenetics with temporally focused patterned light," *J. Neurosci.* **39**(18), 3484–3497 (2019).
547. T. Aharoni and S. Shoham, "Phase-controlled, speckle-free holographic projection with applications in precision optogenetics," *Neurophotonics* **5**(2), 025004 (2018).
548. G. M. Lerman et al., "Real-time in situ holographic optogenetics confocally unraveled sculpting microscopy," *Laser Photonics Rev.* **13**(9), 1900144 (2019).
549. E. Chaigneau et al., "Two-photon holographic stimulation of ReaChR," *Front. Cell Neurosci.* **10**, 234 (2016).
550. C. A. Baker et al., "Cellular resolution circuit mapping with temporal-focused excitation of soma-targeted channelrhodopsin," *Elife* **5**, e14193 (2016).
551. A. Forli et al., "Optogenetic strategies for high-efficiency all-optical interrogation using blue-light-sensitive opsins," *Elife* **10**, e63359 (2021).

552. H. A. Bounds et al., "Multifunctional Cre-dependent transgenic mice for high-precision all-optical interrogation of neural circuits," https://doi.org/10.1101/2021.10.05.463223 (2021).

553. S. Sun et al., "Large-scale femtosecond holography for near simultaneous optogenetic neural modulation," *Opt. Express* **27**(22), 32228–32234 (2019).

554. G. Faini et al., "Ultrafast light targeting for high-throughput precise control of neuronal networks," https://doi.org/10.1101/2021.06.14.448315 (2021).

555. E. Frumker and Y. Silberberg, "Femtosecond pulse shaping using a two-dimensional liquid-crystal spatial light modulator," *Opti. Lett.* **32**(11), 1384–1386 (2007).

556. T. Mayblum et al., "New insights and system designs for temporally focused multiphoton optogenetics," *Proc SPIE* **9329**, 932928 (2015).

557. O. Hernandez et al., "Three-dimensional spatiotemporal focusing of holographic patterns," *Nat. Commun.* **7**, 11928 (2016).

558. B. Sun et al., "Four-dimensional light shaping: manipulating ultrafast spatiotemporal foci in space and time," *Light: Sci. Appl.* **7**(1), 17117 (2018).

559. G. M. Lerman et al., "Precise optical probing of perceptual detection," bioRxiv, 10.1101/456764 (2018).

560. E. Chong et al., "Manipulating synthetic optogenetic odors reveals the coding logic of olfactory perception," *Science* **368**(6497), eaba2357 (2020).

561. H. W. Dalgleish et al., "How many neurons are sufficient for perception of cortical activity?" *Elife* **9**, e58889 (2020).

562. W. T. Newsome, K. H. Britten, and J. A. Movshon, "Neuronal correlates of a perceptual decision," *Nature* **341**(6237), 52–54 (1989).

563. P. Blinder et al., "The cortical angiome: an interconnected vascular network with non-columnar patterns of blood flow," *Nat. Neurosci.* **16**(7), 889–897 (2013).

564. B. Cauli and E. Hamel, "Revisiting the role of neurons in neurovascular coupling," *Front. Neuroenerg.* **2**, 9 (2010).

565. H. Uhlirova et al., "Cell type specificity of neurovascular coupling in cerebral cortex," *Elife* **5**, e14315 (2016).

566. H. Uhlirova et al., "The roadmap for estimation of cell-type-specific neuronal activity from non-invasive measurements," *Philos. Trans. R. Soc. Lond. B Biol. Sci.* **371**(1705), 20150356 (2016).

567. D. A. Boas and A. K. Dunn, "Laser speckle contrast imaging in biomedical optics," *J. Biomed. Opt.* **15**(1), 011109 (2010).

568. A. K. Dunn et al., "Dynamic imaging of cerebral blood flow using laser speckle," *J. Cereb. Blood Flow Metab.* **21**(3), 195–201 (2001).

569. A. K. Dunn et al., "Simultaneous imaging of total cerebral hemoglobin concentration, oxygenation, and blood flow during functional activation," *Opt. Lett.* **28**(1), 28–30 (2003).

570. J. D. Briers, "Laser Doppler, speckle and related techniques for blood perfusion mapping and imaging," *Physiol. Meas.* **22**(4), R35–R66 (2001).

571. A. Devor et al., "Two-photon laser scanning microscopy as a tool to study cortical vaso-dynamics under normal and ischemic conditions," in *Imaging the Brain with Optical Methods*, A. W. Roe, Ed., pp. 245–261, Springer (2009).

572. A. Devor et al., "Frontiers in optical imaging of cerebral blood flow and metabolism," *J. Cereb. Blood Flow Metab.* **32**(7), 1259–1276 (2012).

573. A. Devor et al., "Functional imaging of cerebral oxygenation with intrinsic optical contrast and phosphorescent probes," in *Optical Imaging of Cortical Circuit Dynamics*, B. Weber and F. Helmchen, Eds., Springer, New York (2013).

574. S. Sakadžić et al., "Two-photon microscopy measurement of cerebral metabolic rate of oxygen using periarteriolar oxygen concentration gradients," *Neurophotonics* **3**(4), 045005 (2016).

575. P. Mächler et al., "Microscopic quantification of oxygen consumption across cortical layers," https://doi.org/10.1101/2021.10.13.464176 (2021).

576. J. Mayhew et al., "Spectroscopic analysis of changes in remitted illumination: the response to increased neural activity in brain," *Neuroimage* **10**(3), 304–326 (1999).

577. D. A. Boas et al., "Twenty years of functional near-infrared spectroscopy: introduction for the special issue," *Neuroimage* **85**(Pt 1), 1–5 (2014).
578. A. Grinvald et al., "Imaging the neocortex functional architecture using multiple intrinsic signals: implications for hemodynamic-based functional imaging," *Cold Spring Harb. Protoc.* **2016**(3), pdb top089375 (2016).
579. L. V. Wang and J. Yao, "A practical guide to photoacoustic tomography in the life sciences," *Nat. Methods* **13**(8), 627–638 (2016).
580. J. J. Yao and L. H. V. Wang, "Photoacoustic brain imaging: from microscopic to macroscopic scales," *Neurophotonics* **1**(1), 011003 (2014).
581. R. K. Wang and L. An, "Doppler optical micro-angiography for volumetric imaging of vascular perfusion in vivo," *Opt. Express* **17**(11), 8926–8940 (2009).
582. U. Baran and R. K. Wang, "Review of optical coherence tomography based angiography in neuroscience," *Neurophotonics* **3**(1), 010902 (2016).
583. V. J. Srinivasan et al., "OCT methods for capillary velocimetry," *Biomed. Opt. Express* **3**(3), 612–29 (2012).
584. H. Ren, C. Du, and Y. Pan, "Cerebral blood flow imaged with ultrahigh-resolution optical coherence angiography and Doppler tomography," *Opt. Lett.* **37**(8), 1388–1390 (2012).
585. A. Rakymzhan et al., "Optical microangiography reveals temporal and depth-resolved hemodynamic change in mouse barrel cortex during whisker stimulation," *J. Biomed. Opt.* **25**(9), 096005 (2020).
586. C. W. Merkle and V. J. Srinivasan, "Laminar microvascular transit time distribution in the mouse somatosensory cortex revealed by dynamic contrast optical coherence tomography," *Neuroimage* **125**, 350–362 (2016).
587. V. J. Srinivasan and H. Radhakrishnan, "Optical coherence tomography angiography reveals laminar microvascular hemodynamics in the rat somatosensory cortex during activation," *Neuroimage* **102**(Pt 2), 393–406 (2014).
588. Y. Li, W. Wei, and R. K. Wang, "Capillary flow homogenization during functional activation revealed by optical coherence tomography angiography based capillary velocimetry," *Sci. Rep.* **8**, 4107 (2018).
589. S. E. Erdener et al., "Spatio-temporal dynamics of cerebral capillary segments with stalling red blood cells," *J. Cereb. Blood Flow Metab.* **39**(5), 886–900 (2019).
590. P. Shin et al., "High-speed optical coherence tomography angiography for the measurement of stimulus-induced retrograde vasodilation of cerebral pial arteries in awake mice," *Neurophotonics* **7**(3), 030502 (2020).
591. S. Chen et al., "Imaging hemodynamic response after ischemic stroke in mouse cortex using visible-light optical coherence tomography," *Biomed. Opt. Express* **7**(9), 3377–3389 (2016).
592. S. P. Chong et al., "Cerebral metabolic rate of oxygen (CMRO2) assessed by combined Doppler and spectroscopic OCT," *Biomed. Opt. Express* **6**(10), 3941–3951 (2015).
593. P. Tang et al., "Measurement and visualization of stimulus-evoked tissue dynamics in mouse barrel cortex using phase-sensitive optical coherence tomography," *Biomed. Opt. Express* **11**(2), 699–710 (2020).
594. J. Tang et al., "Imaging localized fast optical signals of neural activation with optical coherence tomography in awake mice," *Opt. Lett.* **46**(7), 1744–1747 (2021).
595. P. J. Marchand et al., "Validation of red blood cell flux and velocity estimations based on optical coherence tomography intensity fluctuations," *Sci. Rep.* **10**, 19584 (2020).
596. H. M. Swartz, "Measuring real levels of oxygen in vivo: opportunities and challenges," *Biochem. Soc. Trans.* **30**, 248–252 (2002).
597. J. M. Arbeit et al., "Hypoxia: importance in tumor biology, noninvasive measurement by imaging, and value of its measurement in the management of cancer therapy," *Int. J. Radiat. Biol.* **82**(10), 699–757 (2006).
598. D. S. Vikram, J. L. Zweier, and P. Kuppusamy, "Methods for noninvasive imaging of tissue hypoxia," *Antioxid. Redox Signaling* **9**(10), 1745–1756 (2007).
599. K. A. Krohn, J. M. Link, and R. P. Mason, "Molecular imaging of hypoxia," *J. Nucl. Med.* **49**, 129S–148S (2008).

600. O. S. Finikova et al., "Energy and electron transfer in enhanced two-photon-absorbing systems with triplet cores," *J. Phys. Chem. A* **111**(30), 6977–6990 (2007).

601. O. S. Finikova et al., "Dynamic quenching of porphyrin triplet states by two-photon absorbing dyes: Towards two-photon-enhanced oxygen nanosensors," *J. Photochem. Photobiol., A: Chem.* **198**(1), 75–84 (2008).

602. A. Y. Lebedev, T. Troxler, and S. A. Vinogradov, "Design of metalloporphyrin-based dendritic nanoprobes for two-photon microscopy of oxygen," *J. Porphyrins. Phthalocyanines* **12**(12), 1261–1269 (2008).

603. L. E. Sinks et al., "Two-photon microscopy of oxygen: polymersomes as probe carrier vehicles," *J. Phys. Chem. B* **114**(45), 14373–14382 (2010).

604. B. Li et al., "More homogeneous capillary flow and oxygenation in deeper cortical layers correlate with increased oxygen extraction," *Elife* **8**, e42299 (2019).

605. R. B. Buxton, "Interpreting oxygenation-based neuroimaging signals: the importance and the challenge of understanding brain oxygen metabolism," *Front. Neuroenerg.* **2**, 8 (2010).

606. K. A. Kasischke et al., "Two-photon NADH imaging exposes boundaries of oxygen diffusion in cortical vascular supply regions," *J. Cereb. Blood Flow Metab.* **31**(1), 68–81 (2011).

607. A. Krogh, "The number and distribution of capillaries in muscles with calculations of the oxygen pressure head necessary for supplying the tissue," *J. Physiol.* **52**(6), 409–415 (1919).

608. L. H. V. Wang and S. Hu, "Photoacoustic tomography: in vivo imaging from organelles to organs," *Science* **335**(6075), 1458–1462 (2012).

609. L. Li et al., "Snapshot photoacoustic topography through an ergodic relay of optical absorption in vivo," *Nat. Protoc.* **16**(5), 2381–2394 (2021).

610. L. Li et al., "Single-impulse panoramic photoacoustic computed tomography of small-animal whole-body dynamics at high spatiotemporal resolution," *Nat. Biomed. Eng.* **1**(5), 1–11 (2017).

611. P. Zhang et al., "High-resolution deep functional imaging of the whole mouse brain by photoacoustic computed tomography in vivo," *J. Biophotonics* **11**(1), e201700024 (2018).

612. P. Zhang et al., "In vivo superresolution photoacoustic computed tomography by localization of single dyed droplets," *Light: Sci. Appl.* **8**(1), 36 (2019).

613. J. Yao et al., "High-speed label-free functional photoacoustic microscopy of mouse brain in action," *Nat. Methods* **12**(5), 407 (2015).

614. L. Li et al., "Label-free photoacoustic tomography of whole mouse brain structures ex vivo," *Neurophotonics* **3**(3), 035001 (2016).

615. S. Na et al., "Massively parallel functional photoacoustic computed tomography of the human brain," *Nat. Biomed. Eng.* (2021).

616. S. Gottschalk et al., "Rapid volumetric optoacoustic imaging of neural dynamics across the mouse brain," *Nat. Biomed. Eng.* **3**(5), 392–401 (2019).

617. B. Rao et al., "Photoacoustic imaging of voltage responses beyond the optical diffusion limit," *Sci. Rep.* **7**, 2560 (2017).

618. M. Chamanzar et al., "Ultrasonic sculpting of virtual optical waveguides in tissue," *Nat. Commun.* **10**, 92 (2019).

619. H. W. Ruan et al., "Fluorescence imaging through dynamic scattering media with speckle-encoded ultrasound-modulated light correlation," *Nat. Photonics* **14**(8), 511–516 (2020).

620. X. A. Xu, H. L. Liu, and L. V. Wang, "Time-reversed ultrasonically encoded optical focusing into scattering media," *Nat. Photonics* **5**(3), 154–157 (2011).

621. Y. M. Wang et al., "Deep-tissue focal fluorescence imaging with digitally time-reversed ultrasound-encoded light," *Nat. Commun.* **3**, 928 (2012).

622. K. Si, R. Fiolka, and M. Cui, "Fluorescence imaging beyond the ballistic regime by ultrasound-pulse-guided digital phase conjugation," *Nat. Photonics* **6**(10), 657–661 (2012).

623. Y. Jiang et al., "Optoacoustic brain stimulation at submillimeter spatial precision," *Nat. Commun.* **11**, 881 (2020).

624. Y. Zhang et al., "Battery-free, lightweight, injectable microsystem for in vivo wireless pharmacology and optogenetics," *Proc. Natl. Acad. Sci. U. S. A.* **116**(43), 21427–21437 (2019).

625. G. Hong and C. M. Lieber, "Novel electrode technologies for neural recordings," *Nat. Rev. Neurosci.* **20**(6), 330–345 (2019).

626. L. C. Moreaux et al., "Integrated neurophotonics: toward dense volumetric interrogation of brain circuit activity-at depth and in real time," *Neuron* **108**(1), 66–92 (2020).

627. D. Kuzum et al., "Transparent and flexible low noise graphene electrodes for simultaneous electrophysiology and neuroimaging," *Nat. Commun.* **5**, 5259 (2014).

628. M. J. Donahue et al., "Multimodal characterization of neural networks using highly transparent electrode arrays," *Eneuro* **5**(6), ENEURO.0187-18.2018 (2018).

629. Y. Qiang et al., "Transparent arrays of bilayer-nanomesh microelectrodes for simultaneous electrophysiology and two-photon imaging in the brain," *Sci. Adv.* **4**(9), eaat0626 (2018).

630. E. M. R. Lake et al., "Simultaneous cortex-wide fluorescence Ca(2+) imaging and whole-brain fMRI," *Nat. Methods*, **17**(12), 1262–1271 (2020).

631. K. Schulz et al., "Simultaneous BOLD fMRI and fiber-optic calcium recording in rat neocortex," *Nat. Methods* **9**(6), 597–602 (2012).

632. M. Wang et al., "Brain-state dependent astrocytic Ca(2+) signals are coupled to both positive and negative BOLD-fMRI signals," *Proc. Natl. Acad. Sci. U. S. A.* **115**(7), E1647–E1656 (2018).

633. J. H. Lee et al., "Global and local fMRI signals driven by neurons defined optogenetically by type and wiring," *Nature* **465**(7299), 788–792 (2010).

634. A. J. Kennerley et al., "Concurrent fMRI and optical measures for the investigation of the hemodynamic response function," *Magn. Reson. Med.* **54**(2), 354–365 (2005).

635. J. Brake, M. Jang, and C. H. Yang, "Analyzing the relationship between decorrelation time and tissue thickness in acute rat brain slices using multispeckle diffusing wave spectroscopy," *J. Opt. Soc. Am. A* **33**(2), 270–275 (2016).

636. Z. Yaqoob et al., "Optical phase conjugation for turbidity suppression in biological samples," *Nat. Photonics* **2**(2), 110–115 (2008).

637. Y. Liu et al., "Optical focusing deep inside dynamic scattering media with near-infrared time-reversed ultrasonically encoded (TRUE) light," *Nat. Commun.* **6**, 5904 (2015).

638. I. M. Vellekoop and A. P. Mosk, "Focusing coherent light through opaque strongly scattering media," *Opt. Lett.* **32**(16), 2309–2311 (2007).

639. C. Ma et al., "Time-reversed adapted-perturbation (TRAP) optical focusing onto dynamic objects inside scattering media," *Nat. Photonics* **8**(12), 931–936 (2014).

640. E. H. Zhou et al., "Focusing on moving targets through scattering samples," *Optica* **1**(4), 227–232 (2014).

641. H. W. Ruan et al., "Focusing light inside scattering media with magnetic-particle-guided wavefront shaping," *Optica* **4**(11), 1337–1343 (2017).

642. P. X. Lai et al., "Photoacoustically guided wavefront shaping for enhanced optical focusing in scattering media," *Nat. Photonics* **9**(2), 126–132 (2015).

643. Y. C. Shen et al., "Focusing light through biological tissue and tissue-mimicking phantoms up to 9.6 cm in thickness with digital optical phase conjugation," *J. Biomed. Opt.* **21**(8), 085001 (2016).

644. M. M. Qureshi et al., "In vivo study of optical speckle decorrelation time across depths in the mouse brain," *Biomed. Opt. Express* **8**(11), 4855–4864 (2017).

645. D. F. Wang et al., "Focusing through dynamic tissue with millisecond digital optical phase conjugation," *Optica* **2**(8), 728–735 (2015).

646. D. Feldkhun et al., "Focusing and scanning through scattering media in microseconds," *Optica* **6**(1), 72–75 (2019).

647. O. Tzang et al., "Wavefront shaping in complex media with a 350 kHz modulator via a 1D-to-2D transform," *Nat. Photonics* **13**(11), 788–793 (2019).

648. T. Laforest et al., "Co-integration of a smart CMOS image sensor and a spatial light modulator for real-time optical phase modulation," *Proc SPIE* **9022**, 90220N (2014).

649. F. Pisanello et al., "Multipoint-emitting optical fibers for spatially addressable in vivo optogenetics," *Neuron* **82**(6), 1245–1254 (2014).

650. F. Pisanello et al., "Dynamic illumination of spatially restricted or large brain volumes via a single tapered optical fiber," *Nat. Neurosci.* **20**(8), 1180–1188 (2017).

651. F. Pisano et al., "Depth-resolved fiber photometry with a single tapered optical fiber implant," *Nat. Methods* **16**(11), 1185–1192 (2019).
652. A. Balena et al., "Two-photon fluorescence-assisted laser ablation of non-planar metal surfaces: fabrication of optical apertures on tapered fibers for optical neural interfaces," *Opt. Express* **28**(15), 21368–21381 (2020).
653. E. Maglie et al., "Ray tracing models for estimating light collection properties of micro-structured tapered optical fibers for optical neural interfaces," *Opt. Lett.* **45**(14), 3856–3859 (2020).
654. F. Pisano et al., "Focused ion beam nanomachining of tapered optical fibers for patterned light delivery," *Microelectron. Eng.* **195**, 41–49 (2018).
655. J. Lee, W. G. Wang, and B. L. Sabatini, "Anatomically segregated basal ganglia pathways allow parallel behavioral modulation," *Nat. Neurosci.* **23**(11), 1388–1398 (2020).
656. S. J. Lee et al., "Monitoring behaviorally induced biochemical changes using fluorescence lifetime photometry," *Front. Neurosci.* **13**, 766 (2019).
657. M. Bianco et al., "Comparative study of autofluorescence in flat and tapered optical fibers towards application in depth-resolved fluorescence lifetime photometry in brain tissue," *Biomed. Opt. Express* **12**(2), 993–1009 (2021).
658. B. Spagnolo et al., "Integrated tapered fibertrode for simultaneous control and readout of neural activity over small brain volumes with reduced light-induced artefacts," https://doi.org/10.1101/2020.07.31.226795 (2021).
659. F. Pisano et al., "Plasmonics on a neural implant: engineering light-matter interactions on the nonplanar surface of tapered optical fibers," *Adv. Opt. Mater.* **10**(2), 2101649 (2022).
660. F. Pisano et al., "Single-cell micro- and nano-photonic technologies," *J. Neurosci. Methods* **325**, 108355 (2019).
661. D. W. Park et al., "Graphene-based carbon-layered electrode array technology for neural imaging and optogenetic applications," *Nat. Commun.* **5**, 5258 (2014).
662. M. Thunemann et al., "Deep 2-photon imaging and artifact-free optogenetics through transparent graphene microelectrode arrays," *Nat. Commun.* **9**, 2035 (2018).
663. N. Driscoll et al., "Multimodal in vivo recording using transparent graphene microelectrodes illuminates spatiotemporal seizure dynamics at the microscale," *Commun. Biol.* **4**(1), 136 (2021).
664. D.-W. Park et al., "Electrical neural stimulation and simultaneous in vivo monitoring with transparent graphene electrode arrays implanted in GCaMP6f mice," *ACS Nano* **12**(1), 148–157 (2018).
665. X. Liu et al., "A compact closed-loop optogenetics system based on artifact-free transparent graphene electrodes," *Front. Neurosci.* **12**, 132 (2018).
666. K. J. Seo et al., "Transparent, flexible, penetrating microelectrode arrays with capabilities of single-unit electrophysiology," *Adv. Biosyst.* **3**(3), 1800276 (2019).
667. A. K. Geim, "Graphene: status and prospects," *Science* **324**(5934), 1530–1534 (2009).
668. K. Kostarelos et al., "Graphene in the design and engineering of next-generation neural interfaces," *Adv. Mater.* **29**(42), 1700909 (2017).
669. S. K. Rastogi et al., "Effect of graphene on nonneuronal and neuronal cell viability and stress," *Nano Lett.* **17**(5), 3297–3301 (2017).
670. J. Zhang et al., "Stretchable transparent electrode array for simultaneous electrical and optical interrogation of neural circuits in vivo," *Nano Lett.* **18**(5), 2903–2911 (2018).
671. Y. C. Lu et al., "Ultralow Impedance graphene microelectrodes with high optical transparency for simultaneous deep two-photon imaging in transgenic mice," *Adv. Funct. Mater.* **28**(31), 1800002 (2018).
672. F. Barkhof, S. Haller, and S. A. R. B. Rombouts, "Resting-state functional MR imaging: a new window to the brain," *Radiology* **272**(1), 29–49 (2014).
673. B. J. He, "Spontaneous and task-evoked brain activity negatively interact," *J. Neurosci.* **33**(11), 4672–4682 (2013).
674. T. Ito et al., "Task-evoked activity quenches neural correlations and variability across cortical areas," *PLoS Comput. Biol.* **16**(8), e1007983 (2020).

675. F. Albers et al., "Multimodal functional neuroimaging by simultaneous BOLD fMRI and fiber-optic calcium recordings and optogenetic control," *Mol. Imaging Biol.* **20**(2), 171–182 (2018).

676. X. M. Chen et al., "Mapping optogenetically-driven single-vessel fMRI with concurrent neuronal calcium recordings in the rat hippocampus," *Nat. Commun.* **10**, 5239 (2019).

677. J. H. Lee, "Informing brain connectivity with optogenetic functional magnetic resonance imaging," *Neuroimage* **62**(4), 2244–2249 (2012).

678. D. Miyamoto and M. Murayama, "The fiber-optic imaging and manipulation of neural activity during animal behavior," *Neurosci. Res.* **103**, 1–9 (2016).

679. H. S. Palmer, "Optogenetic fMRI sheds light on the neural basis of the BOLD signal," *J. Neurophysiol.* **104**(4), 1838–1840 (2010).

680. F. Schlegel et al., "Fiber-optic implant for simultaneous fluorescence-based calcium recordings and BOLD fMRI in mice," *Nat. Protoc.* **13**(5), 840–855 (2018).

681. M. Schwalm et al., "Cortex-wide BOLD fMRI activity reflects locally-recorded slow oscillation-associated calcium waves," *Elife* **6**, e27602 (2017).

682. N. C. Pegard et al., "Compressive light-field microscopy for 3D neural activity recording," *Optica* **3**(5), 517–524 (2016).

683. T. Nobauer et al., "Video rate volumetric Ca2+ imaging across cortex using seeded iterative demixing (SID) microscopy," *Nat. Methods* **14**(8), 811–818 (2017).

684. T. V. Truong et al., "High-contrast, synchronous volumetric imaging with selective volume illumination microscopy," *Commun. Biol.* **3**, 74 (2020).

685. Z. K. Zhang et al., "Imaging volumetric dynamics at high speed in mouse and zebrafish brain with confocal light field microscopy," *Nat. Biotechnol.* **39**(1), 74–83 (2021).

686. P. Quicke et al., "Subcellular resolution three-dimensional light-field imaging with genetically encoded voltage indicators," *Neurophotonics* **7**(3), 035006 (2020).

687. L. Cong et al., "Rapid whole brain imaging of neural activity in freely behaving larval zebrafish (Danio rerio)," *Elife* **6**, e28158 (2017).

688. O. Skocek et al., "High-speed volumetric imaging of neuronal activity in freely moving rodents," *Nat. Methods* **15**(6), 429–432 (2018).

689. R. Turcottea et al., "Dynamic super-resolution structured illumination imaging in the living brain," *Proc. Natl. Acad. Sci. U. S. A.* **116**(19), 9586–9591 (2019).

690. K. Yanny et al., "Miniscope3D: optimized single-shot miniature 3D fluorescence microscopy," *Light-Sci. Appl.* **9**(1), 171 (2020).

691. J. K. Adams et al., "Single-frame 3D fluorescence microscopy with ultraminiature lensless FlatScope," *Sci. Adv.* **3**(12), e1701548 (2017).

692. S. Hong et al., "Structured illumination microscopy for the investigation of synaptic structure and function," *Synapse Dev.* **1538**, 155–167 (2017).

693. P. W. Winter et al., "Two-photon instant structured illumination microscopy improves the depth penetration of super-resolution imaging in thick scattering samples," *Optica* **1**(3), 181–191 (2014).

694. W. Tahir et al., "Anatomical modeling of brain vasculature in two-photon microscopy by generalizable deep learning," *BME Front.* **2021**, 1 (2021).

695. S. Stefan and J. Lee, "Deep learning toolbox for automated enhancement, segmentation, and graphing of cortical optical coherence tomography microangiograms," *Biomed. Opt. Express* **11**(12), 7325–7342 (2020).

696. S. Soltanian-Zadeh et al., "Fast and robust active neuron segmentation in two-photon calcium imaging using spatiotemporal deep learning," *Proc. Natl. Acad. Sci. U. S. A.* **116**(17), 8554–8563 (2019).

697. J. Lecoq et al., "Removing independent noise in systems neuroscience data using DeepInterpolation," *Nat. Methods* **18**(11), 1401–1408 (2021).

698. Y. J. Bao et al., "Segmentation of neurons from fluorescence calcium recordings beyond real time," *Nat. Mach. Intell.* **3**(7), 590–600 (2021).

699. P. Rupprecht et al., "A database and deep learning toolbox for noise-optimized, generalized spike inference from calcium imaging," *Nat. Neurosci.* **24**(9), 1324–1337 (2021).

700. A. Giovannucci et al., "CaImAn an open source tool for scalable calcium imaging data analysis," *Elife* **8**, e38173 (2019).

701. Z. Q. Wang et al., "Real-time volumetric reconstruction of biological dynamics with light-field microscopy and deep learning," *Nat. Methods* **18**(5), 551 (2021).

702. N. Wagner et al., "Deep learning-enhanced light-field imaging with continuous validation," *Nat. Methods* **18**(5), 557–563 (2021).

703. L. H. Jin et al., "Deep learning enables structured illumination microscopy with low light levels and enhanced speed," *Nat. Commun.* **11**, 1934 (2020).

704. F. S. Pavone and S. Shoham, *Handbook of Neurophotonics*, CRC Press, Boca Raton (2020).

705. L. M. Richards et al., "Intraoperative laser speckle contrast imaging with retrospective motion correction for quantitative assessment of cerebral blood flow," *Neurophotonics* **1**(1), 015006 (2014).

706. K. Sato et al., "Intraoperative intrinsic optical imaging of human somatosensory cortex during neurosurgical operations," *Neurophotonics* **4**(3), 031205 (2017).

707. A. Rayshubskiy et al., "Direct, intraoperative observation of similar to 0.1 Hz hemo-dynamic oscillations in awake human cortex: Implications for fMRI," *Neuroimage* **87**, 323–331 (2014).

708. S. Kleinlogel et al., "Emerging approaches for restoration of hearing and vision," *Physiol. Rev.* **100**(4), 1467–1525 (2020).

709. L. Gagnon et al., "Quantifying the microvascular origin of BOLD-fMRI from first principles with two-photon microscopy and an oxygen-sensitive nanoprobe," *J. Neurosci.* **35**(8), 3663–3675 (2015).

710. M. G. Kozberg et al., "Resolving the transition from negative to positive blood oxygen level-dependent responses in the developing brain," *Proc. Natl. Acad. Sci. U. S. A.* **110**(11), 4380–4385 (2013).

711. A. Adams et al., "International brain initiative: an innovative framework for coordinated global brain research efforts," *Neuron* **105**(2), 212–216 (2020).

Biographies of the authors are not available.